STUDY OF THE CHARGE SPIN AND HEAT IN THE METAL/MAGNETIC INSULATOR NANO-STRUCTURE

by

Danru Qu

A dissertation submitted to Johns Hopkins University in conformity with the requirements for the degree of Doctor of Philosophy

Baltimore, Maryland

August, 2016

Abstract

This dissertation focuses on spin caloritronics, which studies the interplay between heat, spin and charge currents, and classic spintronics, which studies the generation and transport of a pure spin current without the accompaniment of a net charge current.

When a temperature gradient is applied across the yttrium iron garnet (YIG), a pure spin current is generated, and this is the spin Seebeck effect. Usually, a thin layer of Pt film is attached to detect the pure spin current generated in YIG. In the study of the Pt/YIG structure, we have observed the magnetic proximity effect in the nonmagnetic metal Pt, which compromises the suitability of Pt as a pure spin current detector. The signature of the magnetic proximity effect is the magnetoresistance and anomalous Hall like behavior. More interestingly, the magnetoresistance in the Pt/YIG structures exhibits an unusual magnetic field angular dependence unlike any known magnetoresistance.

Because of the magnetic proximity effect in Pt/YIG, one needs to search for a better pure spin current detector for the conclusive establishment of the spin Seebeck effect. We show that Au, with negligible magnetic proximity effect when in contact with YIG, is a better, indeed the best material to date. By varying the Au thin film thicknesses on YIG, we have conclusively demonstrated the intrinsic spin Seebeck behavior of YIG without appreciable contamination of any other effect.

The observation of the intrinsic spin Seebeck effect allows us to inject a pure spin current into various materials of interest, such as the *5d* heavy metals, to study the inverse spin Hall effect, where a spin current is converted to a charge current, and obtain the two

key parameters of spin Hall angle, which is the conversion efficiency between spin current and charge current, and spin diffusion length, which quantifies the distance a spin can travel without losing its information, in pure spin current phenomena.

Prior to our work, the inverse spin Hall effect has only been observed in non-magnetic metals. We have demonstrated the inverse spin Hall effect in ferromagnetic metals such as permalloy (Py) and Co, as well as antiferromagnetic metal of Cr. To our surprise, we found that the inverse spin Hall effect is independent of the magnetic ordering. By decoupling the magnetization of Co and YIG, we show that the direction of the Co magnetization has no effect on the spin index of the spin current from YIG. We have also found that the inverse spin Hall effect in antiferromagnetic Cr is apparently independent of the antiferromagnetic ordering since the inverse spin Hall effect remains the same below and above the Cr Neel temperature. Moreover, we have determined the spin Hall angles in these magnetic materials, and found their values to be comparable to those of the *5d* metals, which exhibit some of largest values. In fact, we have found Cr, although only a *3d* metal, possesses the largest spin Hall angle of all metals.

The new physical phenomena and materials established in this dissertation, including the unique magnetoresistance, the intrinsic spin Seebeck effect, the inverse spin Hall effect in ferromagnetic and anitferromagnetic metals, the large spin Hall angle in magnetic materials, and independent of their magnetic ordering, the largest spin Hall angle in Cr, may help us build superior spintronic devices, especially pure spin current devices.

This work was performed under the guidance of Professor C. L. Chien at Johns Hopkins University.

To my parents

Acknowledgements

I would like to express my sincere gratitude to my thesis advisor, Professor C. L. Chien for his guidance, inspiration and tremendous support on both my thesis work and career choice. I have greatly benefited from his expertise in all aspects. He has set a great example as a researcher and mentor with constant enthusiasm and commitment to excellence. I am fortunate and proud to be your student!

I am indebted to the help and feedback on my thesis from Professor Oleg Tchernyshyov. I am thankful to the advice from my thesis committee members; Professor Petar Maksimovic, Professor En Ma and Professor David Gracias. I am grateful to have collaborated with Dr. Bingfeng Miao and Dr. Dai Tian on some of the projects. I would like to thank Dr. Sunxiang Huang and Dr. Yufan Li for helpful discussions. It has also been a pleasure to work with Dr. Weigang Wang, Mingen Li, Fei Chen, Dr. Qinli Ma, Dr. Weiwei Lin, Li Ma, Steven Tran, Yifan Chen, Dr. Yu Wang, Dr. Yue Zhang and Brent Page. I would also like to thank Lauren Fowler, Kelley Key, Norma Berry, Brian Schriver, Jessica Rexroad and Carm King for their warm assistance, and Lyle Schwartz and Dean Carpenter for their excellent machine shop work.

A special thanks to my boyfriend Ssu-Yen Huang. Thank you very much for your unlimited support, encouragement and company.

Last but not the least, I thank my parents for their unconditional love and blind trust, without whom I could never have started this journey.

Contents

List of Figures

List of Tables

Chapter 1

Introduction

During the past two decades, strong efforts have been focused on research of the spin degrees of freedom in solid state systems. The interest is motivated by both the quest to understand fundamental scientific questions and the potential in technological applications. This chapter reviews some key advances and recent emerging trends in spintronics.

The golden era of spintronics begins with the observation of *interlayer coupling* in magnetic multilayers in 1986. When two ferromagnetic (FM) layers are seperated by a non-FM spacer layer, there is interlayer coupling between the two FM layers through the spacer layer. It was observed that an antiferromagnetic (AFM) interaction exists between the two Fe layers in the Fe/Cr/Fe(001) trilayer [1]. This result leads to the discovery of the *giant magnetoresistance* (GMR), for which the Nobel Prize in Physics was awarded in 2007 to Albert Fert and Peter Grünberg. [2, 3]

Magnetoresistance (MR) is the property of a material to change the value of its resistance under an external magnetic field. In the Fe/Cr/Fe(001) trilayer structure, at zero magnetic field, the magnetization of the two FM layers are antiparallel with each other, with magnetoresistance of $\rho_{\uparrow\downarrow}$. When a large magnetic field (a few thousand Oe) is applied to force the two FM layers to be parallel, its magnetoresistance ($\rho_{\uparrow\uparrow}$, parallel

configuration) is smaller than that of the AFM configuration ($\rho_{\uparrow\downarrow}$). In some samples, the magnetoresistance ratio

$$\frac{\Delta R}{R} = \frac{\rho_{\uparrow\downarrow} - \rho_{\uparrow\uparrow}}{\rho_{\uparrow\uparrow}} \quad (1)$$

can reach 100% [2]. It is "giant" compared with the magnetoresistance in a single magnetic layer which is usually 1%. The large difference in the magnetoresistance ratio is because of their drastically different mechanisms. In a single magnetic layer, the magnetoresistance is a result of the *s*-*d* scattering, where *s* electron is scattered by *d* orbitals with different cross sections under different magnetic field orientations.

The mechanism of GMR is the conduction electron spin dependent scattering at the FM/NM layer interfaces. For the ferromagnetic metal, the density of states for spin majority band and spin minority band are not equal at the Fermi surface. The electrons with spin antiparallel to the spin majority band are more strongly scattered than the parallel spins. Therefore, the antiparallel configuration is expecting higher resistance than parallel configuration, as shown in Fig.1.1. Most of the early works on GMR used current flow in plane geometry, the current flow perpendicular to plane geometry was accomplished in 1991, where a larger MR ratio is obtained compared with the current perpendicular to plane geometry. [4]

In the study of GMR, an oscillating behavior of FM and AFM interaction between the two FM layers was observed as a function of the spacer thickness. [5] This effect can be explained by the Ruderman-Kittel-Kasuya-Yosida (RKKY) interaction that the coupling between the two FM layers is mediated by the conduction electrons in the

spacer layer, and the oscillating periods depends on the Fermi's surface of the spacer layer. [6]

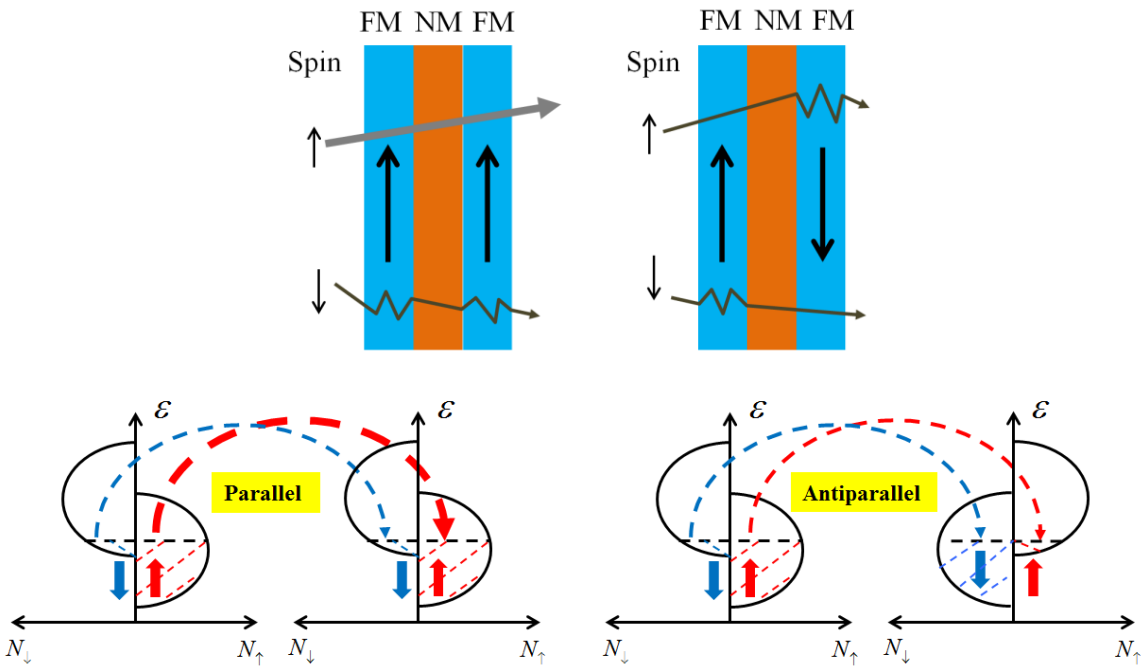

Fig.1.1 (Top panels) Schematic drawing of the spin dependent scattering in GMR structure with FM layers being parallel or antiparallel. (Bottom panels)Schematic drawing of majority and minority bands density of states at the Fermi level with parallel and antiparallel FM configurations.

The discovery of the interlayer coupling and GMR effect had strong impact on information technology, since the high GMR ratio is beneficial for both the magnetic field sensor device and magnetic data storage device. However, in order to utilize GMR in those devices, one has to control the FM layer configurations by breaking the interlayer coupling, which for the FM layers in the Fe/Cr/Fe structure requires a very high magnetic field (2000 Oe) to align the two FM layers.

This problem was solved by the *exchange bias* in the FM/AFM system, as shown in Fig. 1.2, which was discovered in 1956 by Meiklejohn and Bean [7], but the renewed

interest was triggered by its reduction of the magnetic field to observe the GMR effect [8].In the FM/NM/FM/AFM multilayer system, the FM next to the AFM is pinned as a fixed layer because of the exchange coupling to the AFM (magnetization curve of FM is shifted away from the zero field axis). The other FM is the free layer, which does not couple to any magnetic thin film, and can respond to, or be controlled by a small magnetic field (a few Oe). The reduction of the saturation field has greatly enhanced the sensitivity of magnetic field sensor devices, and made the writing of magnetic data much easier.

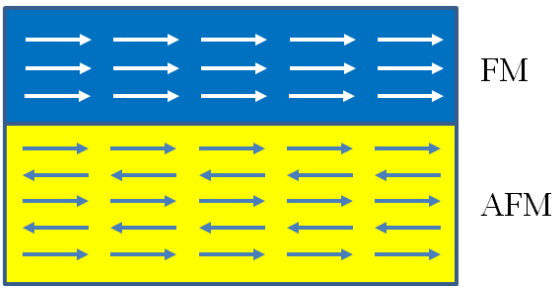

Fig.1.2 Schematic drawing of the exchange bias in the FM/AFM structure.

Similar to the GMR structure, the *magnetic tunnel junction* (MTJ) structure is based on two FM layers sandwiched by a thin *insulating* layer. the tunneling magnetoresistance (TMR), defined the same as GMR by Eq. 1, is used to describe the magnetoresistance in MTJ. The TMR effect was first measured in the Fe/Ge-O/Co multilayer structure with MR ratio of 14% at 4.2 K by Julliere in 1975 [9]. The renewed interest in TMR was triggered by the discovery of high TMR ratios in a multilayer with a thin amorphous aluminum oxide at *room temperature* by Miyazaki *et al* [10] and Moodera *et al* [11] in 1995.

The breakthrough came with the use of epitaxial MgO (001) as a tunnel barrier, where the MR ratio was predicted to be over 1000% in fully ordered (001) oriented Fe/MgO/Fe by first principle calculation [12], and experimentally was observed to be higher than 200%. [13] Since MgO barrier has a crystalline structure, we may use symmetry considerations to classify electron states. Electrons belonging to the Δ_1 irreducible representation (isotropic, usually with a large positive spin polarization at the Fermi level, atomic orbitals *s*, p_z and $d_{3z^2-r^2}$) decay slowly in space in the MgO layer, while electrons from other irreducible representations such as Δ_2 and Δ_5 (exemplified by atomic orbitals p_x and p_y) penetrate to a smaller depth into the MgO layer. Thus, when the barrier becomes thicker, Bloch states with the Δ_1 symmetry dominate the conductance. Single-crystal. MgO is therefore an effective symmetry filter. To make an MgO layer an effective spin filter, one has to find materials with Bloch state $\Delta_1$symmetry at the Fermi energy for one spin channel but not for the other. The material should be compatible with the thin MgO layer. Remarkably, Fe is such a material, where the $\Delta_1$symmetry electron exists only in the majority spin band but not in the minority spin band. Thus the majority spins have a larger probability to tunnel through the MgO barrier than the minority spin spins. In the case of antiparallel configuration, even if a majority spin tunnel through the barrier, it does not contribute to the conductance since it cannot propagate in the minority spin channel of the second FM layer. This symmetry and spin-filtering behavior is shown in Fig.1.3. It was observed that the CoFeB/MgO/CoFeB magnetic tunnel junction (MTJ) has the MR ratio up to 500% at room temperature. [14]

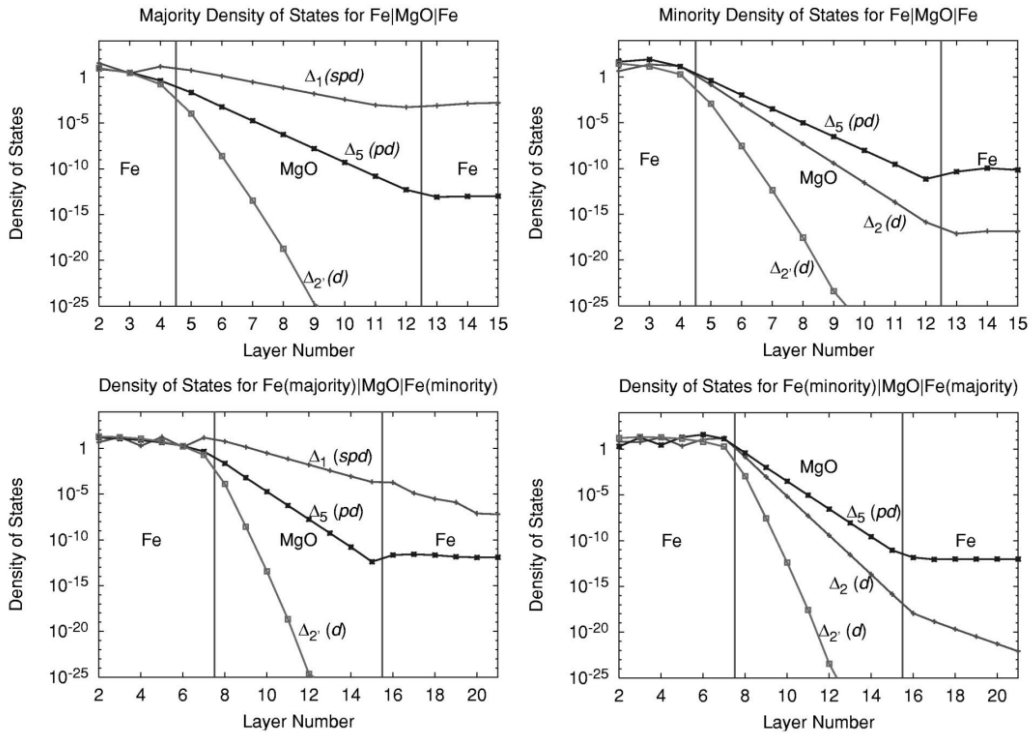

Fig.1.3 Tunneling density of states (DOS) for electrons with perpendicular to plane velocity for Fe(100)/MgO/Fe(100) structure. Upper left is the DOS for electrons from majority spin band to majority spin band, upper right is the DOS for minority to minority, lower left is majority to minority and lower right is minority to majority. [Figure is obtained from Phys. Rev. B **63** 054416 (2001)]

The giant TMR effect at room temperature is a very desirable property for spintronic devices. In *magnetic random access memory* (MRAM), the difference in resistance for parallel and antiparallel magnetizations configuration are useful properties for binary computing based on the two configurations, as shown in Fig.1.4. Since no electric current is necessary to retain the information, MRAM is non-volatile and energy efficient. The first generation of MRAM uses current-induced Oersted magnetic field to change the state of a data cell. However, a magnetic field cannot be efficiently localized and thus may accidentally switch the state of a neighboring data cell. This issue can be

solved by using a different switching method based on the application of electric current discussed next.

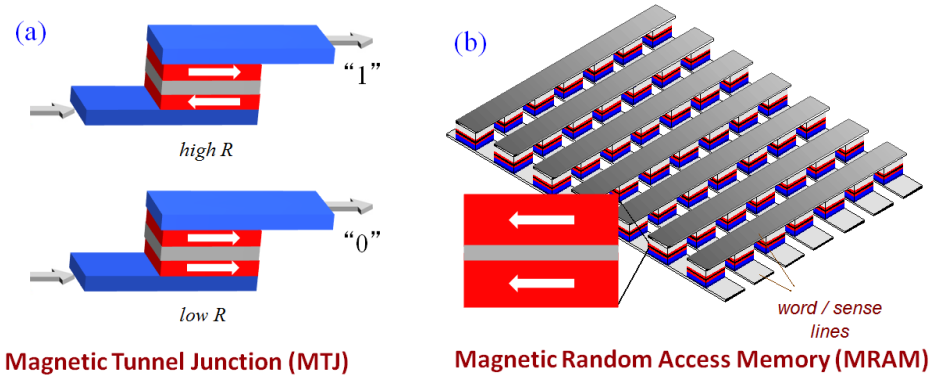

Fig. 1.4 (a) Schematic drawing of MTJ with magnetic layers sandwiched by an insulator. Electric current flows through the junction. The antiparallel and parallel configurations of the two ferromagnets represent high and low resistance states and therefore "1" and "0" states in Boolean computation. (b) Schematic drawing of MRAM where each unit bit is a MTJ.

The *spin transfer torque* (STT) effect, independently predicted by Slonczewski and Berger in 1996, is another major event in the field of spintronics. [15, 16] In STT, angular momentum can be transferred from an electric to the FM layer. As shown in Fig.1.5, when electrons flow perpendicular to the plane in a FM layer, they are partially transmitted through the FM layer with the polarization parallel to the magnetization of the ferromagnet, the others are reflected back with opposite spin polarizations, and if the electrons are initially polarized, they exert a torque to the FM layer. The torque density is $\vec{\tau}_{ST} = \frac{\hbar}{2eM_S t} J_s[(\hat{m} \times \hat{\sigma}) \times \hat{m}]$. Here, $\hat{\sigma}$ is spin index, $\hat{m}$ is magnetization direction, M_S is the saturation magnetization of the FM layer, t is the thickness of the FM layer and J_S is spin current. Slonczewski predicted that, depending on the geometry of the device, and the magnitude of charge current and external magnetic field, the STT effect could

reorient the static magnetization of the FM layer or cause a dynamical steady-state precession of the FM magnetization.

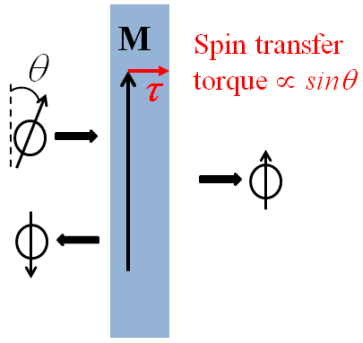

Fig. 1.5 Illustration of the spin transfer torque.

In magnetic multilayers with FM/NM/FM or FM/tunnel barrier/FM structure, where one FM is free layer (easy to switch) and the other FM is fixed layer (hard to switch). When electrons flow from the fixed layer to the free layer, Fig.1.6, the transmitted *parallel polarized* electrons exert the STT to the free layer, and results in a preferably *parallel configuration*. On the other hand, when electrons flow from the free layer to the fixed layer (Fig.), the reflected *antiparallel polarized* electrons, exert the STT to the free layer, resulting a preferably *antiparallel configuration*. Therefore, instead of the external magnetic field, the magnetization orientations of an FM layer can be controlled by the direction of *current* flowing through the junction using STT, one for parallel and the opposite for antiparallel configuration.

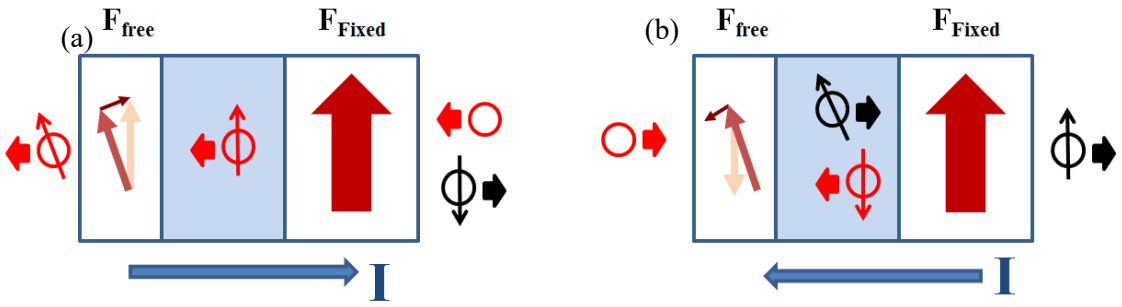

Fig. 1.6 Illustration of the spin transfer torque in magnetic multilayers. (a) Charge current flows from fixed layer to free layer favors parallel FM configuration. (b) Charge current flows from free layer to fixed layer favors antiparallel FM configuration.

The use of STT greatly has greatly increased the density of data cells in the MRAM. However, the device encounters another problem: it is susceptible to the electromigration and breakdown due to the high current density ($10^7 A/cm^2$) passing through the junction. In order to solve this problem, new materials and new physics have to come into the field of spintronics.

The field of spintronics is evolving, and many emerging spintronic subfields are attracting lots of attentions. These subfields may enable us to develop high density, low energy cost and stable spintronic devices. Among them are spintronic devices utilizing pure spin current, and spin caloritronics converting heat current to spin current, which the author studied in this dissertation.

The pure spin current without the accompanying charge current can be carried by equal amount of electrons with opposite spins moving in opposite directions, or by spin wave in a magnetic insulator. [17] Since spin current carries spin information with the least amount of charge carriers or no charge carriers at all (in magnetic insulator), it generates much less Joule heat compared with spin polarized current, and therefore it is

highly energy efficient. Another very important advantage for pure spin current is the current path. As shown in Fig. 1.7(a), the spin-polarized current passes *through* the magnetic nanostructure, threatening its integrity with high current density. In the pure spin current switching, shown in Fig 1.7(b), no net charge current flows through the nanostructures, except the pure spin current.

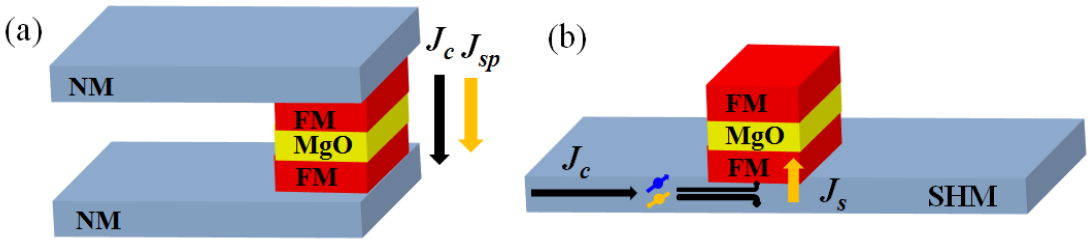

Fig.1.7 (a) Spin transfer torque switching from the spin polarized current in the FM/MgO/FM junction. Current flows through the junction. (b) Pure spin current switching in the FM/MgO/FM junction from the pure spin current in the spin Hall metal. Current flows in the bottom spin Hall metal.

Spin caloritronics studies the interplay between heat, spin and charge current. With the increasing amount of waste heat in electronic or spintronic devices, utilization of the waste heat is important for "greener" spintronic devices. In the spin Seebeck effect (SSE) [18], spin current is generated from the temperature gradient across a ferromagnet, and converted into charge current by an attached spin current detector, achieving the conversion from heat to spin and charge current. The spin caloritronics has important energy applications if highly efficient spintronic devices can be fabricated.

This dissertation focuses on the pure spin current spintronics and the spin caloritronics, more specifically, SSE in ferromagnetic insulator yttrium iron garnet (YIG), and the pure spin current/charge current conversion in various metals of interest. During the study, many intriguing physical phenomena have been observed, such as the magnetic

proximity effect in the Pt/YIG structure; the intrinsic SSE in YIG from a pure spin current detector Au; the inverse spin Hall effect in various materials including magnetic materials through the thermal spin injection from YIG; the independence of inverse spin Hall effect on the magnetic orderings.

This dissertation is arranged as follows: experimental methods such as thin film fabrication and characterizations are discussed in Chapter 2. An introduction of the pure spin current phenomena is given in Chapter 3. The spin Seebeck effect and its controversies are discussed in Chapter 4. Chapter 5 is focused on the magnetic proximity effect and its controversies. The intrinsic spin Seebeck effect is observed in Au/YIG structures and is discussed in Chapter 6. The inverse spin Hall effect in various nonmagnetic materials and a model to calculate the spin Hall angles are discussed in Chapter 7. Chapter 8 discusses the inverse spin Hall effect in magnetic materials and its independence of magnetic ordering. Chapter 9 is the conclusion.

References to Chapter 1

1. P. Grunberg, R. Schreiber, Y. Pang, M. B. Brodsky, and H. Sowers, "Layered magnetic structures: evidence for antiferromagnetic coupling of Fe layers across Cr interlayers", Phys. Rev. Lett. **57**, 2442 (1986)
2. M. N. Baibich, J. M. Broto, A. Fert, F. Nguyen Van Dau, F. Petroff, P. Etienne, G. Creuzet, A. Friederich, and J. Chazelas, "Giant magnetoresistance of (001)Fe/(001)Cr magnetic super lattices", Phys. Rev. Lett. **61** 2472 (1988)
3. G. Binasch, P. Grunberg, F. Saurenbach, and W. Zinn, "Enhanced magnetoresistance in layered magnetic structures with antiferromagnetic interlayer exchange", Phys. Rev. B **39** 4828 (1989)
4. J. Bass and W. P. Pratt Jr., "Current-perpendicular (CPP) magnetoresistance in magnetic metallic multilayers", J. Magn. Magn. Mater. **200**, 274 (1999)
5. S. S. P. Parkin, N. More, and K. P. Roche, "Oscillations in exchange coupling and magnetoresistance in metallic superlattice structures: Co/Ru, Co/Cr, and Fe/Cr", Phys. Rev. Lett. **64**, 2304 (1990)
6. D. M. Edwards, J. Mathon, R. B. Muniz, and M. S. Phan, "Oscillations of the exchange in magnetic multilayers as an analog of de Haas-van Alphen effect", Phys. Rev. Lett. **67**, 493 (1991)
7. W. H. Meiklejohn and C. P. Bean, "New magnetic anisotropy", Phys. Rev. **105**, 904 (1957)

8. B. Dieny, V. S. Speriosu, S. S. P. Parkin, B. A. Gurney, D. R. Wilhoit, and D. Mauri, "Giant magnetoresistive in soft ferromagnetic multilayers", Phys. Rev. B **43**, 1297(R) (1991)
9. M. Julliere, "Tunneling between ferromagnetic films", Phys. Lett. A, **54**, 225 (1975)
10. T. Miyazaki and N. Tezuka, "Giant magnetic tunneling effect in Fe/Al_2O_3/Fe junction", J. Magn. Magn. Mater. **139**, L231 (1995)
11. J. S. Moodera, Lisa R. Kinder, Terrilyn M. Wong, and R. Meservey, "Large magnetoresistance at room temperature in ferromagnetic thin film tunnel junctions", Phys. Rev. Lett. **74**, 3273 (1995)
12. W. H. Butler, X. -G. Zhang, T. C. Schulthess, and J. M. MacLaren, "Spin-dependent tunneling conductance of Fe/MgO/Fe sandwiches" Phys. Rev. B **63** 054416 (2001)
13. S. Yuasa, T. Nagahama, A. Fukushima, Y. Suzuki, and K. Ando, "Giant room-temperature magnetoresistance in single-crystal Fe/MgO/Fe magnetic tunnel junctions", Nat. Mater. **3** 868 (2004)
14. Y. M. Lee, J. Hayakawa, S. Ikeda, F. Matsukura and H. Ohno, "Effect of electrode composition on the tunnel magnetoresistance of pseudo-spin-valve magnetic tunnel junction with a MgO tunnel barrier", Appl. Phys. Lett. **90**, 212507 (2007)
15. J. C. Slonczewski, "Current-driven excitation of magnetic multilayers", J. Magn. Magn. Mater. **159**, L1 (1996)
16. L. Berger, "Emission of spin waves by a magnetic multilayer traversed by a current", Phys. Rev. B **54**, 9353 (1996)
17. J. E. Hirsch, "Spin Hall effect", Phys. Rev. Lett. **83**, 1834 (1999)

18. K. Uchida, S. Takahashi, K. Harii, J. Ieda, W. Koshibae, K. Ando, S. Maekawa, and E. Saitoh, “Observation of the spin Seebeck effect”, Nature, **455**, 778 (2008)

Chapter 2

Thin Film Fabrication and Characterization Technique

2.1 Introduction

Thin films are materials from one atomic layer to a few μm's in thickness. Because of the reduced dimensionality in such systems, thin films are as important as bulk materials in the discovery of novel physical behaviors and properties. Moreover, with a proper choice of the substrate and growth conditions, one can fabricate amorphous, polycrystalline or single crystalline thin film with relaxed or strained lattices; one can construct multilayers with interfaces based on known thin films but with new physical properties; one can massively produce thin films with lateral dimensions in the orders of meters and maintaining good crystalline structure; and with the development of the experimental technique, one can precisely control the thickness and shape of thin films down to the scale of single atoms.

There are many types of thin film fabrication methods including those using physical processes, such as sputtering, pulsed laser deposition, and thermal evaporation, and those using chemical reaction processes such as electrochemical deposition, atomic layer deposition and chemical vapor deposition. Comparing with other thin film fabrication methods, sputtering has the advantages of independence on the melting point of the material, the ability to sputter both insulating and metallic material and even liquid

materials such as Ga, and maintains good stoichiometry of the target material composition.

In this chapter, magnetron sputtering is described. The methods used to achieve high vacuum for thin film fabrication, the methods used to pattern the thin film (photolithography), and the methods used to characterize physical properties of the thin film such as X-ray diffraction (crystalline structure), atomic force microscope (surface morphology), vibrating sample magnetometry (magnetic properties), probe station and physical property measurement system (electrical and thermal transport properties) are also introduced and discussed.

2.2 Magnetron Sputtering

2.2.1 Sputtering Basics

The first known record of sputtering dates back to 1852, when W. R. Grove demonstrated the deposition of materials in a gaseous discharge environment.[1] The deposition process was thought to be the result of thermal evaporation for more than a century, but later people realized that atoms begin to escape as a consequence of a collision cascade from the ion bombardment of the solid target well before the target reaches its local thermal equilibrium.

To perform sputtering, one needs to put the target in a discharged gaseous environment. Most often inert Ar is selected as the sputtering gas, so that the films grown

would not be contaminated with oxygen and nitrogen if one had air as the sputtering gas. The sputtering can be administered in a wide range of pressure from sub-mtorr to torr and in all gaseous environments. Since one usually desires a film of the correct composition, of high purity, with crystal orientation, with a smooth surface, and with a well-defined thickness, one works very diligently to achieve these goals. One must use a chamber that can achieve high vacuum ($<10^{-7}$ Torr) since reactive gases in a poor vacuum would contaminate the films.

The sputtering process starts with the ionization of a sputtering gas, in the chamber at sufficiently low pressure. The ionization process follows the equation $A+e^{-}\longrightarrow A^{+}+2e^{-}$, where A is the gas molecule, most often Ar.[2] During the sputtering process, the energized particles create a glowing plasma, which is partially ionized gas, consisting of positively charged particles (Ar^{+} ions), negatively charged particles (electrons) and neutral ones. The relaxation of an electronically excited state is nearly instantaneous around (10^{-8} s), and in most cases is accompanied by the emission of UV or visible light and gives the plasma its glow. The plasma environment is sustained by a strong electric field established by a voltage (~ 300 V) between ground and the target of intended deposited materials. The target is negatively charged to attract and accelerate the positively charged Ar^{+}, which upon bombardment knock out the atoms from the target and deposit on the substrate, shown in Fig.2.1.

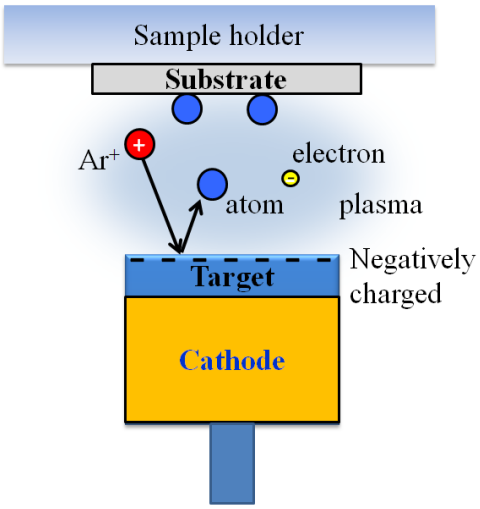

Fig. 2.1 Schematic drawing of sputtering.

When ions bombard the surface of a material, depending on their energy, the bombardment may cause several processes: ion reflection, ion absorption (sticking to the surface), sputtering, ion implantation, chemical reaction with the surface, and electron and photon emission. The sputtering process occurs in the ion beam energy range from 10 eV to 3 keV, where lower than this energy range absorption and reflection appear, and higher than this range ion implantation occurs. In the following, we describe several aspects of the sputtering.

2.2.2 Sputter Yield

The key principle of sputtering process is the energy and momentum transfer from the incident ions to the atoms to be knocked off the surface. The sputter yield (*S*) specifies the number of atoms release for incident ions at a specific energy, and can be described by

$$S = \frac{\text{Number of sputtered atoms}}{\text{Number of incident ions}}.$$

S depends on the energy of the incident ions, the relative mass of the ions (m_1) and target atoms (m_2), the binding energy of atoms in the target and the angle of incidence of ions. It is proportional to $\propto \frac{m_1 m_2}{(m_1+m_2)^2}$. Normally, the sputter yield ranges from 0.1 to 10.

2.2.3 Sputter Gas Pressure

The sputtered atoms escaping from the target diffuse on to the substrate. The deposition rate is proportional to the sputtering yield and is also affected by the sputter gas pressure. The gas pressure is inversely proportional to the mean free path of the particle. When the gas pressure is too high, thanks to inelastic collisions with the molecules, the ions are slowed down creating fewer secondary electrons from the bombardment that reduces the Ar ionization portion. The deposition rate decreases as the gas pressure increases. On the other hand, when the gas pressure is too low, the plasma may not be sustained as a result of the lack of gas molecules. The deposition rate also decreases when the gas pressure decreases because of less frequent bombardment. For magnetron sputtering, the preferred sputtering gas pressure is a few mtorr.

2.2.4 Diode Sputtering and Magnetron Sputtering

The simplest sputtering technique is diode sputtering with grounded substrate and chamber and a negatively charged sputtering gun where the target is attached. Ar^+ ions accelerate towards the negatively charged target, bombarding the target atoms and

causing the escape of atoms from the target as described earlier. However, this method has a very low deposition rate and secondary electrons from the target bombardment may damage the substrate.

Magnetron sputtering has been developed to address the shortcomings of diode sputtering. A carefully designed magnet assembly is placed just below the thin target such that an annular magnetic field protrudes above the target surface. Fig.2.2. Due to the magnetic field, moving electrons are trapped above the target surface by the magnetic flux. An increased density of electrons enhances their probability of ionizing the Ar gas atoms, thereby enhancing the deposition rate. At the same time, the confinement of electrons reduces the damage to the substrate from the secondary electrons. Magnetron sputtering makes a great improvement to the sputtering technique.

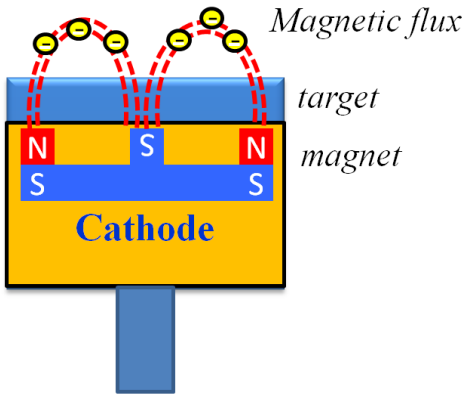

Fig. 2.2 Schematic drawing of magnetron sputtering.

2.2.5 DC and RF sputtering

For DC sputtering, a conducting target is negatively charged to attract Ar^+ ions. However, for insulating target, DC sputtering does not work because of the positive charge accumulation on the target. However, RF sputtering with alternating voltages with

frequency of 13.56 MHz works for insulating target. Thanks to the large mass differences between ions and electrons, heavy ions cannot follow the frequency of alternating voltage but light electrons still can. Therefore, electrons neutralize the positive charges on the target and allow the sputtering of the insulating target.

2.2.6 Reactive Sputtering

When fabricating oxide or nitride compounds, in addition to Ar, controlled amount of reactive gases such as O_2, N_2, and NH_3 may be added to the sputtering process to allow the sputtered particles react with these gases. In this manner, one can fabricate NbN with reactive sputtering using an Nb target and N_2 gas.

2.2.7 Wedged Layer Deposition

Wedged layer deposition is used to fabricate thin films with a gradient in thickness in one direction. A wedge sample is ideal for studying thickness-dependent properties of a film. To deposit a wedged layer, one can control the substrate and the shutter above the deposition gun, such that the thickness of the material on a large substrate can be made to vary linearly with position, as shown in Fig.2.3. One can slice a wedged sample into many smaller samples each has approximately one thickness. Wedged samples are very useful for determining the thickness dependence of a film's properties.

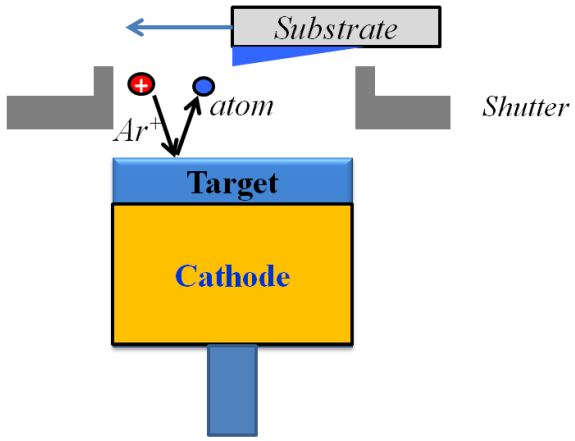

Fig. 2.3 Schematic drawing of the wedge deposition.

2.2.8 Co-sputtering

Only a few thin film deposition techniques can readily fabricate multi-element materials. Sputtering is one of them. Besides sputtering of a multi-element target, there is another variation: co-sputtering. Co-sputtering involves at least two sputtering guns with overlapping deposition. As one advances on the substrate platform and composition of the two materials are continuing varying; one material increasing while the other decreasing. With careful positioning and tilting of the sputtering guns, one can even accomplish linear variation of the composition, and even nearly constant total film thickness. Fig.2.4 shows the co-sputtering thickness profile for Au-Ta alloy thin films the author fabricated. It is worth mentioning that sputtering is a vapor quench technique, which means that it is able to fabricate alloys with metastable phases that are not in the equilibrium phase diagram.

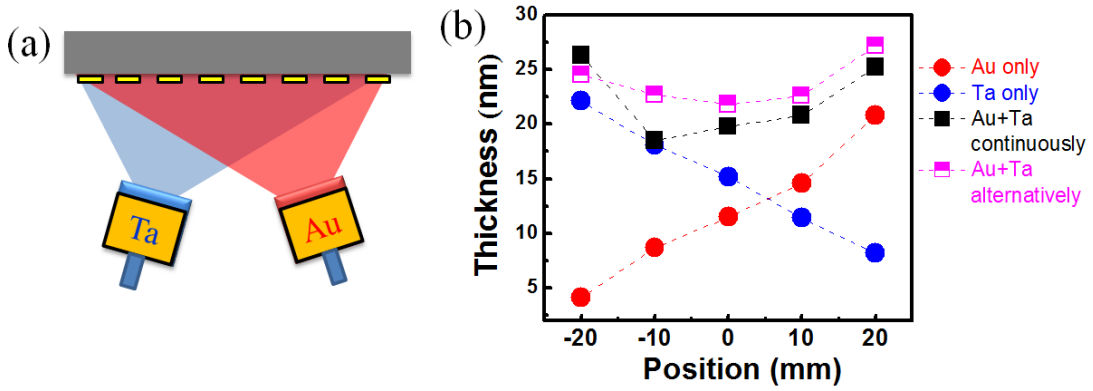

Fig. 2.4 (a) Schematic drawing of the co-sputtering. (b) Thickness profile of the Au and Ta co-sputtering film. The dots represent the following processes: Au gun only (red), Ta gun only (blue), Au and guns operating continuously (black), Au and Ta guns alternating (pink).

2.3 Vacuum Basics

Perfect vacuum has almost zero pressure. However, this is never achieved in reality. The residual gases are mostly from the outgassing of the chamber material. Any system at the 10^{-11} torr level is already in the ultra-high vacuum (UHV) range. The best vacuum ever achieved in a laboratory environment is 10^{-15} Torr.

High vacuum is important for fabrication of high-purity materials. From the kinetic theory of gases, the number of molecules striking a unit area of surface per unit time (gas impingement rate) is $\Gamma = \frac{P}{(2\pi mkT)^{1/2}}$, P is the gas pressure, m is the molecular mass of the gas, k is the Boltzmann constant, and T is the temperature. For a vacuum with base pressure as low as 10^{-10} Torr, it takes more than 8 hours for the residual gas to form a monolayer at room temperature, assuming each gas molecule sticks to the substrate. By comparison, when the vacuum base pressure is 10^{-6} Torr, the residual gas may need only 3 seconds to form a monolayer.[3] Throughout the research for this dissertation, vacuum systems with base pressures from 10^{-7} to 10^{-8} Torr have been used.

To achieve high vacuum, vacuum pumps are selected and used to pump out the

gases in the chamber. Usually a pre-vacuum pump (e.g., a rotary one) is used first to achieve a rough vacuum before using the high-vacuum pumps in order to protect those high vacuum pumps from break down under higher pressure upon seeing atmosphere. Here we describe several high vacuum pumps that the author has used in the laboratory.

Diffusion pumps were the first high vacuum pumps in operation, as shown in Fig.2.5. It is an oil-based pump, where heated oil vapor is used to knock the gas molecules with downward momentum and then remove them by a prevacuum pump. The diffusion pump has a high pumping speed at low cost, and it can last a long time with proper usage, but it may suffer from the possibility of contaminated vacuum chambers due to backstreaming oil molecules.

Turbomolecular pump resembles jet engine with a stack of multiple angled blades, as shown in Fig.2.6. Rotor blades, stack between stationary stator blades, rotate at a very high speed up to 1500 rotations per second. When a gas molecule enters the pump, it bounces downward to the exhaust because of the collision with the angled blades. Turbo-pumps are clean, fast, and efficient in maintaining high vaccum.

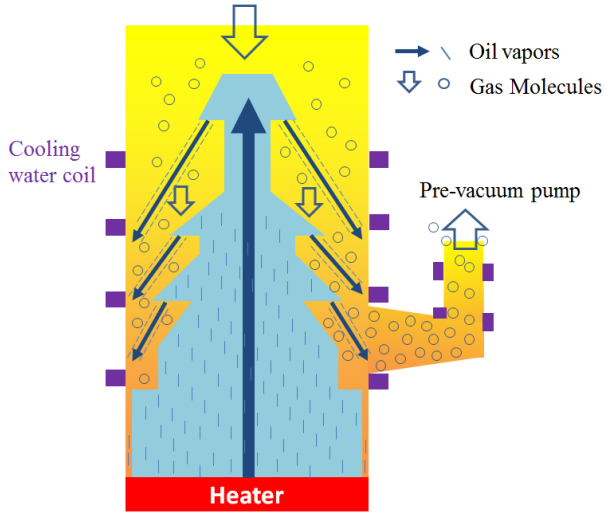

Fig. 2.5 Schematic drawing of oil pump.

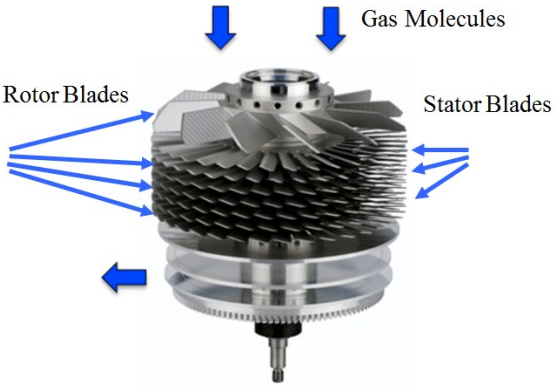

Fig. 2.6 Illustration of turbo pump. [Figure is obtained from *Edwards Vac*]

Cryogenic pump operates at low temperature, and is based on the adsorption of gas on cold surfaces. As shown in Fig.2.7, there are three stages for the cryo-pump. The first stage is an outer surface, held at about 80 K and capturing mostly water vapor. The second stage is an inverted cup shaped inner surface held at about 15 K to 20 K trapping the common gases that condense above 15 K, such as N_2 and O_2. The third stage is the underside of the cup coated with porous activated charcoal absorbing gas molecules with a low condensation temperature, such as helium and hydrogen. A cryo-pump is also clean, fast and efficient.

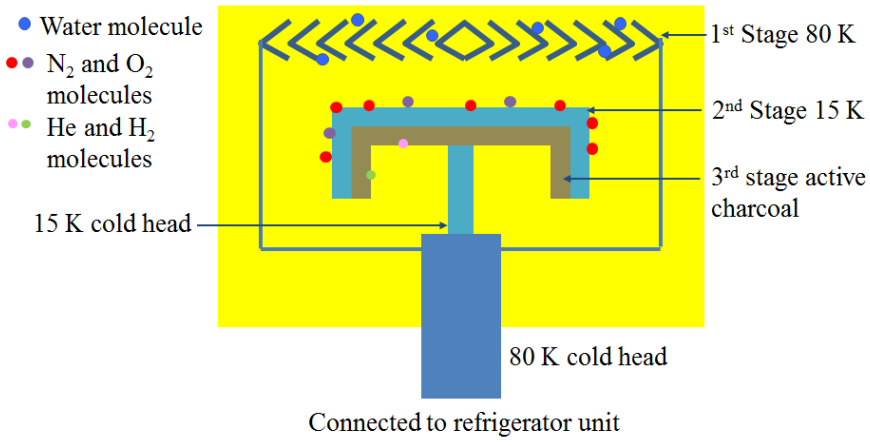

Fig. 2.7 Schematic drawing of cryo-pump.

2.4 Photolithography

Photolithography is a process that uses light to transfer patterns from a photomask to a photoresist coated on a material. It was invented in 1822 by Nicephore Niepce, who used a natural asphalt, the Bitumen of Judea (a *negative* photoresist thanks to its solubility), as the first photoresist to make a printing plate. When soluble natural asphalt is coated on a sheet of metal, glass or stone plate, the parts exposed to light become less soluble while the unexposed parts can be rinsed away. After that, the exposed parts of the plate can be chemically etched. In 1940, Oskar Suβ created a *positive* photoresist which is insoluble initially but become soluble when exposed to light, and it is used in the opposite manner to the negative photoresist.

The photolithography process involves several important steps: preparation of photo mask, coating of photoresist, sample baking, UV light exposure, post-baking, post-exposure, and development. One has to optimize these steps to successfully transfer the pattern from the mask to the photoresist. Usually, photolithography takes place in a cleanroom to avoid contaminations from suspended particles in the air.

Besides photolithography, there are also other lithography methods such as electron beam lithography, ion beam lithography, etc. E-beam lithography uses a focused beam of electrons to change the solubility of the resist and thus draw patterns with sub-10 nm resolution. Ion beam lithography uses focused beam of ions, which are much heavier particles than electrons, thus has higher energy than e-beam lithography to draw patterns on hard resist.

Compared with these methods, photolithography has the advantages of low cost and creating patterns over an entire surface efficiently. On the other hand, the resolution of photolithography is limited since a UV light has relatively long wavelength compared with that of an electron beam or ion beam. With the development of light sources and lithography processes, the resolution of optical photolithography has been shrunk to about 10 nm using an extreme ultraviolet wavelength with immersion lithography technique. The immersion lithography technique uses liquid medium that has a high refractive index instead of an air gap between the optical lens and the photoresist surface. Therefore, the wavelength of light travelling in the liquid medium can be further reduced and the resolution can be enhanced.

2.5 X-Ray Diffraction

2.5.1 Introduction

X-rays was discovered by Röntgen in 1895, who was awarded the first Nobel Prize in physics in 1901. X-rays are electromagnetic waves covering the wavelength between 10^{-12} m to 10^{-9} m. Thanks to their short wavelengths comparable with the crystal lattice constant (a few to a few tens of Angstrom), X-ray diffraction is often used to study the crystalline structure of materials. In this session, small-angle reflectivity, X-ray diffraction measurement, and pole figures are introduced.

A schematic drawing of X-ray scattering is shown in Fig.2.8. The incident x-ray beam is fixed along the x axis, the sample plane has angle ω with incident beam in the xz plane, and the diffracted beam is collected by the detector at angle 2θ with reference to the incident beam also in the xz plane. Ideally, $\omega=\theta$, experimentally there is a small

offset between the two angles. The rotation of the sample stage along the normal axis is characterized by angle ϕ. The rotation of the sample stage along the horizontal inplane axis is characterized by angle ψ. [4]

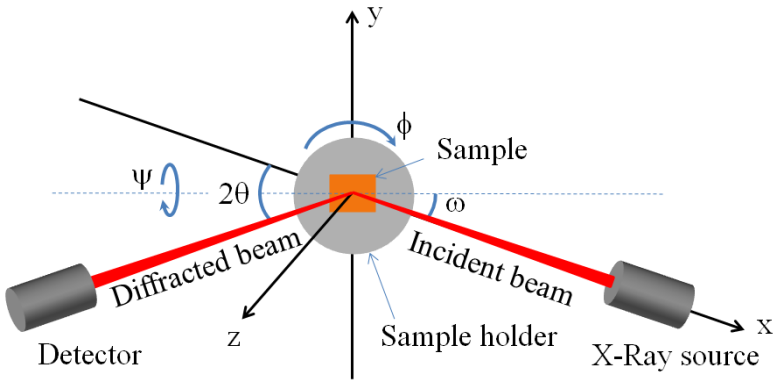

Fig. 2.8 Schematic drawing of the XRD.

The fundamental principle of X-ray diffraction is the Bragg's Law, shown in Fig.2.9, where each diffraction peak satisfies the relation

$$2dsin\theta = n\lambda.$$

Here d is the spacing between atomic planes, 2θ is the angle between the incident and diffracted x-ray beams, n is the diffraction order and λ is the wavelength of the x-ray, in the X'Pert system the author use, $\lambda = 1.5406$ Å.

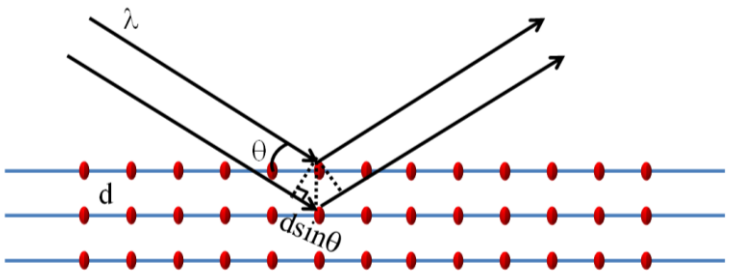

Fig.2.9 Schematic drawing of the Bragg's Law.

Two very useful basic XRD scans are the $2\theta/\omega$ scan and the *rocking curve* scan. In the $2\theta/\omega$ scan, the 2θ and ω change in a coupled manner so that the atomic planes diffracting the X-ray do not change. The $2\theta/\omega$ scan gives information on the atomic plane spacing and the film thickness. From the intensity and the width of the peak, one is able to obtain information such as grain size and film roughness. In the *rocking curve* scan, the detector is fixed at certain Bragg angle and the angle ω of the sample stage changes by a small amount. A perfect crystal should generate a sharp peak in rocking curve scan, while defects such as curvature, dislocation and mosaicity will broaden the peak.

2.5.2 X-Ray Diffraction Pattern

The $2\theta/\omega$ scan generates Bragg peaks indexed by the Miller indices. In this notation, Miller indices (*hkl*) denote a family of planes orthogonal to $h\boldsymbol{A}+k\boldsymbol{B}+l\boldsymbol{C}$, where ***A, B, C*** are the basis of the reciprocal lattice vectors and *d* is the interplane distance in Bragg's law. Depending on the crystal system

$$\text{Cubic: } \frac{1}{d^2} = \frac{h^2+k^2+l^2}{a^2}$$

$$\text{Tetragonal: } \frac{1}{d^2} = \frac{h^2+k^2}{a^2} + \frac{l^2}{c^2}$$

$$\text{Orthorhombic: } \frac{1}{d^2} = \frac{h^2}{a^2} + \frac{k^2}{b^2} + \frac{l^2}{c^2}$$

$$\text{Hexagonal: } \frac{1}{d^2} = \frac{4}{3}\left(\frac{h^2+hk+k^2}{a^2}\right) + \frac{l^2}{c^2}$$

where *a, b*, and *c* are lattice constants of the crystal; in a cubic lattice, *a=b=c,* in a tetragonal lattice, *a=b*. Thus, based on the lattice constant (*a, b* and *c*) and a set of atomic planes represented by Miller indices (*hkl*), one can predict the x-ray diffraction angle (2θ). Likewise, one can obtain the lattice constant (*a, b* and *c*) based on the x-ray crystalline angle (2θ) and Miller indices (*hkl*).

Different crystals present different Bragg peaks due to different atomic plane spacing. However, some Bragg peaks disappear in certain crystalline structures because of the x-ray interferences. This is captured by the geometrical structure factor

$$S_A = \sum_{j=1}^{n} e^{i\boldsymbol{A}\cdot\boldsymbol{d_j}}.$$

Here, $\boldsymbol{A}$ is the reciprocal lattice vector, $\boldsymbol{d}$ is the scatterer position. For example, for the body centered cubic (bcc) structure with basis ($\boldsymbol{d_0} = 0$, $\boldsymbol{d_1} = \frac{a}{2}(\hat{\boldsymbol{x}} + \hat{\boldsymbol{y}} + \hat{\boldsymbol{z}})$), and reciprocal lattice vector $\boldsymbol{A} = \frac{2\pi}{a}(h\hat{\boldsymbol{x}} + k\hat{\boldsymbol{y}} + l\hat{\boldsymbol{z}})$, the structure factor is

$$S_A = 1 + (-1)^{h+k+l}.$$

When *h+k+l*=odd, $S_A = 0$, which means the diffraction pattern disappears. Thus, bcc structure only show *h+k+l*=even peaks. For the face centered cubic (fcc) structure with basis ($\boldsymbol{d_0} = 0$, $\boldsymbol{d_1} = \frac{a}{2}(\hat{\boldsymbol{x}} + \hat{\boldsymbol{y}})$, $\boldsymbol{d_2} = \frac{a}{2}(\hat{\boldsymbol{y}} + \hat{\boldsymbol{z}})$, $\boldsymbol{d_3} = \frac{a}{2}(\hat{\boldsymbol{x}} + \hat{\boldsymbol{z}})$), the structure factor $S_A = 1 + (-1)^{h+k} + (-1)^{h+l} + (-1)^{k+l}$. When *h, k, l* are combinations of odd and even numbers, $S_K = 0$, the diffraction pattern disappears, and only when *h, k, l* are all odd or even numbers, there is a diffraction peak.

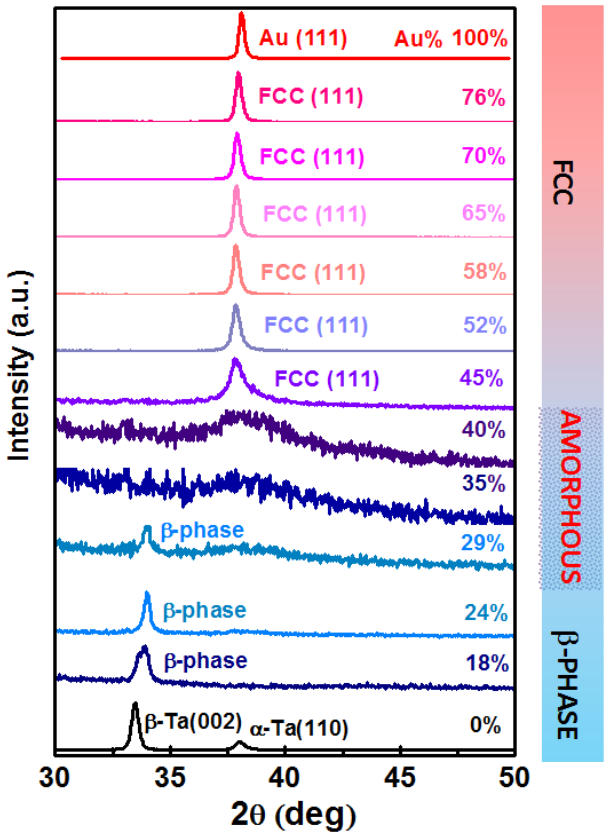

Fig. 2.10 XRD pattern for AuTa alloy films.

Fig.2.10 is the X-ray diffraction peaks the author obtained for thin Au_xTa_{1-x} films with different Au and Ta compositions. Au has fcc structure, and only diffraction peaks with unmixed index (all odd or all even) can be seen. Ta has two structures, the alpha-phase which is a bcc structure, and the beta-phase which is a tetragonal structure. In the middle, the Au_xTa_{1-x} alloy thin film show amorphous peaks which are broad and have low intensity.

2.5.3 Small-Angle Reflectivity

At small angles ($2\theta<10^{\circ}$), from Bragg's Law, one calculates d>1 nm. Clearly, it is much larger than the distance between atomic planes (a few Å) but is comparable with the thin film thicknesses. In fact, not only the atomic planes can reflect the X-ray, film surfaces and interfaces can also reflect the X-ray. Therefore, at small incident angle, X-ray reflectivity oscillations represent the thickness of a thin film.

Fig.2.11(a) is the small angle reflectivity of thin W film on Si substrate, from the oscillation and Bragg's Law, we calculate the thickness of the film $d = 42\ nm$. Fig.2.11(b) is the reflectivity of $[Au/Ta]_6$ multilayer, it is clear there are two series of oscillation peaks with different $\Delta(2\theta)$. $\Delta(2\theta)=0.317°$ corresponds to the total thickness of the multilayer, where $d_{[AuTa]_6} = 8.83/0.32 = 28\ nm$, and $\Delta(2\theta)=2.032°$ corresponds to the thickness of a single $[Au/Ta]_1$ stack, where $d_{[AuTa]_1} = 8.83/2.03 = 4.3\ nm$.

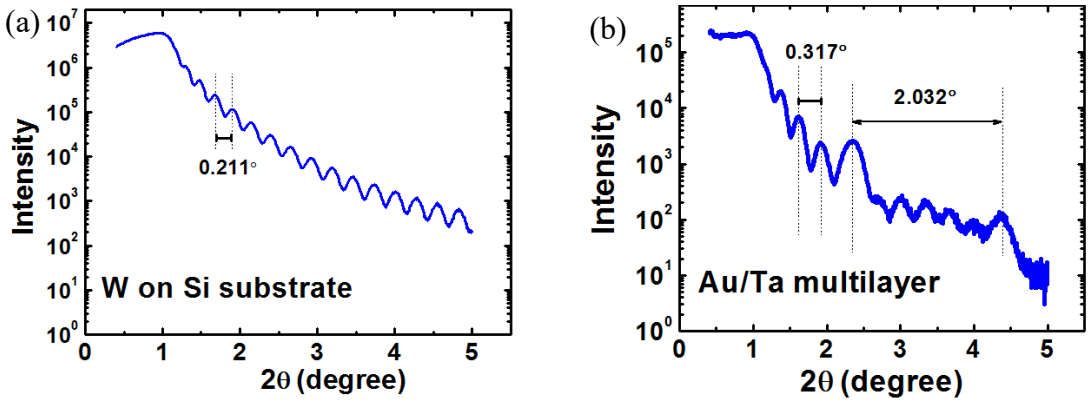

Fig.2.11 (a) Small angle XRR for thin W film on Si substrate. (b) Small angle XRR for Au/Ta multilayer structure.

2.5.4 Pole Figures

For single crystals, one obtains one set of diffraction peaks characterizing the single-crystal out-of-plane structure, without tilting the sample plane. And if one wants to get another set of crystalline peaks characterizing the inplane structure, one has to properly tilt the sample plane and perform the pole figure scan.

To perform the pole figure measurement, one first sets 2θ at a certain Bragg peak position, then tilt the sample stage by changing ψ (0-90°) and ϕ (0-360°). The angle ψ, representing the tilted normal axis direction, can be calculated for any given crystalline lattice. For example, for a simple cubic structure with out-of-plane texture being the (100) plane, in order to see the (111) planes, as shown in Fig.2.12, one needs to first tilt the sample stage by changing ψ to 54.7°(the angle between the (111) plane and the (100) plane), and then rotate the sample stage along its normal axis by scanning ϕ. One is expecting to see four peaks during the ϕ scan, representing the (111), $(\bar{1}11)$, $(1\bar{1}1)$ and $(11\bar{1})$ planes.

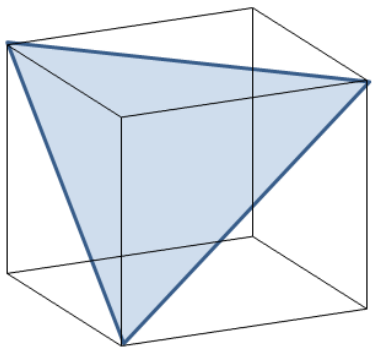

Fig.2.12 Schematic drawing of the (111) plane for the cubic structure.

2.6 Atomic Force Microscope

The atomic force microscope (AFM) was invented by IBM scientists in 1982. It is used to map the surface morphology of samples.[5] AFM does not suffer from the limitation of optical resolution nor a vacuum environment for electron beam. It can operate at ambient atmosphere with atomic spatial resolution. The lateral resolution of AFM is about 30 nm, but the vertical resolution can reach as high as 0.1 nm.

The AFM consists of a cantilever with a sharp probe (a 3-6 μm tall pyramid with 15-40 nm end radius) at its free end, which operates in close proximity with the sample surface. A laser beam is focused on the cantilever above the probe, and a position sensitive photodetector is used to detect the reflected laser beam. There is also a piezoelectric element in the cantilever holder oscillating at the cantilever's resonance frequency, Fig.2.13.

When the AFM operates, it picks up atomic forces that include mechanical contact, van der Waals interaction, capillary action, chemical bonding, electrostatic attraction/ repulsion, and magnetic response in the MFM mode. Due to the force between the probe tip and the sample, the cantilever bends, shifting the position of the reflected laser beam on the photodetector. There are two operation modes for AFM imaging, the contact mode and the tapping mode, which are discussed next.

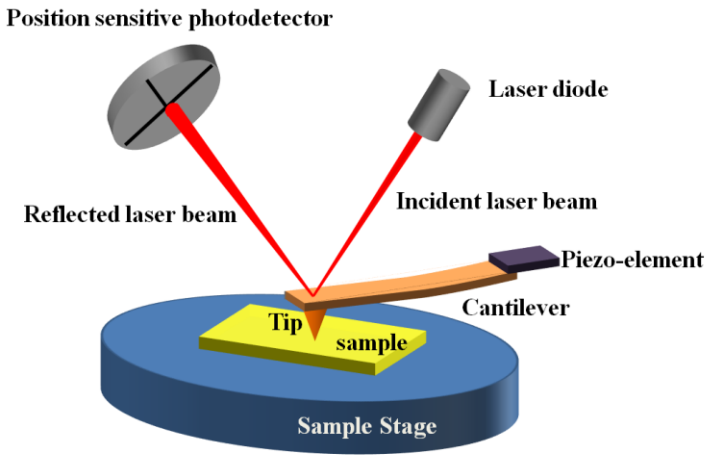

Fig.2.13 Schematic drawing of the atomic force microscope.

In the contact mode, the tip is in close contact with the sample surface, as shown in Fig.2.14(a). When the tip approaching the sample surface, it first experiences a strong attractive Van der Waals force, and then, when it gets closer to the sample surface, the repulsive force, because of the Pauli principle, becomes stronger. In the contact mode, the tip is placed at a close distance from the surface, where the overall atomic force is repulsive. The drawback of this method is that the parallel-to-sample-surface force exerted on the sample can be very high and may result in sample damage.

In order to solve the problem in the contact mode, the tapping mode where the cantilever oscillates during imaging is used, Fig.2.14(b). In the tapping mode, the driving frequency of the cantilever oscillation is kept constant at its resonance frequency, and the amplitude varies from several nm to 200 nm, depending on the distance between the tip and the surface. The tapping mode reduces the tip damage to the sample surfaces.

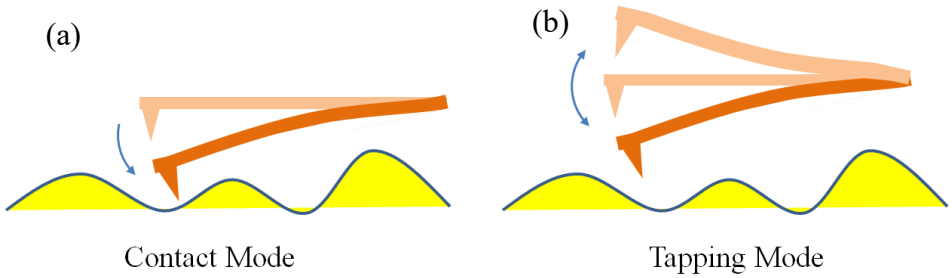

Fig. 2.14 Schematic drawing of the two operating mode for AFM: (a)the contact mode and (b)the tapping mode.

2.7 Vibrating Sample Magnetometer

The vibrating sample magnetometer (VSM) was invented by Simon Foner at the Lincoln Laboratory MIT in the 1950s. [6] A schematic side view and top view of a VSM is shown in Figs.2.15 and 2.16. The VSM consists of an electromagnet that provides a uniform magnetic field and of a Hall probe attached to the magnet to measure the magnetic field. A sample rod is placed between the electromagnets and in the center of the eight pick up coils, as shown in Fig.2.15.

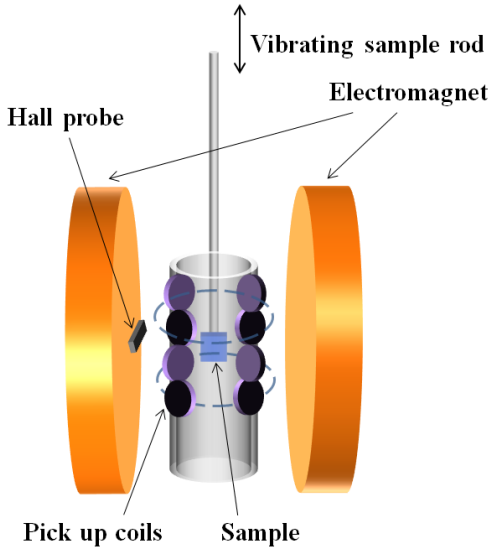

Fig.2.15 Schematic drawing of the vibrating sample magnetometry.

During the measurement, the sample attached to the rod vibrates with small amplitude A, normally between 0.1 mm and 1 mm, and with a frequency ω in the vertical direction perpendicular to the magnetic field. The frequency of vibration is chosen to avoid frequencies from common noise sources, such as 60 Hz of the electricity, 60, 75, 85, or 100 Hz of the scan rates of computer monitors, and integer multiples of those frequencies.

The VSM is based on Faraday's law of induction, which states that a changing magnetic field flux induces an electric field. Suppose that an external magnetic field induces magnetic moment M in the sample. The magnetic field generated by the magnetic moment of the sample is,

$$B_S = gM \ ,$$

where g is a function of the sample position. According to Faraday's law, the changing magnetic flux induces a voltage V in the pick-up coils.

$$V \propto \frac{d}{dt} B_S \propto \frac{dg}{dt} M \propto A \frac{de^{i\omega t}}{dt} M \propto A\omega e^{i\omega t} M$$

The voltage is measured by the lock-in amplifier, which can measure small signals accurately by using a narrow bandpass filter to allow and amplify signals with certain frequencies. After comparing the measured voltage with the reference, the magnetization of the sample can be obtained.

When performing a measurement of the sample magnetization dependence on the magnetic field orientation, instead of rotating the sample and coils, the electromagnet is rotated. Because the relative position of the sample and of the pickup coils is fixed, this

mode eliminates the variation of the proportionality coefficient between the magnetic moment and the voltage in the coils. The sensitivity can reach as little as 10^{-6} emu.

A top view of the VSM is shown in Fig.2.16. The eight pickup coils sit very closely to each other with four on the top panel and four on the bottom panel. The purpose of using eight detection coils is to compensate the positional dependence of the samples on each coil. For instance, if with only four pickup coils, fairly large errors are introduced if the sample is not centered. Therefore, the eight-coil system allows accurate measurements of the magnetization of a material in more than one direction.

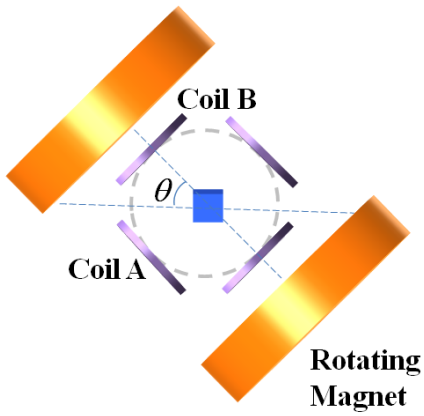

Fig.2.16 Schematic drawing of the top view of the VSM.

2.8 Probe Station

To measure electrical properties of a material, one needs to wire the sample with the electrical sources and meters. Common bonding methods include the usage of metal wires, indium sphere, silver paste, solder etc. A probe station provides a method to precisely position thin needles on the surface of the material mechanically. Since no bonding is required for a probe contact, it is the most convenient method to measure the

electric transport properties of a material. Moreover, a station environment can be combined with many other functional parts, such as a magnet or a closed cycle refrigerator. In this section, we describe electrical and thermal transport measurements.

2.8.1 Electrical Transport Measurement

Electrical transport measurements usually include resistivity, IV curve, Hall resistivity, etc. In this section, resistivity and Hall measurements are discussed.

Longitudinal Resistivity

The longitudinal resistivity (ρ_{xx}) is obtained when voltage is measured along the direction of the current. To measure the resistivity of a material, there are a few methods, such as two-point, four-point, Van Der Pauw for arbitrary shape, and other methods.

Compared with the two-terminal resistivity measurement, which suffers from the contact resistance, the four-point measurement offers a more accurate method to measure resistivity. As illustrated in Fig. 2.17, in the Hall bar patterned sample, the two current probes send an electrical current through the wire, and the two voltage probes pick up voltage signal over length l. The resistivity of this sample is therefore $\rho = \frac{V}{I} \cdot \frac{wt}{l}$, here w is the width, t is the thickness, I is the current and V is the voltage.

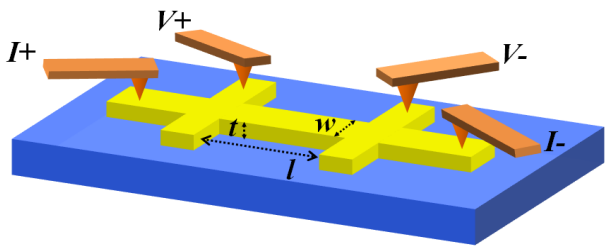

Fig.2.17 Schematic drawing of the four probe resistivity measurement.

For samples with arbitrary shape, the Van der Pauw measurement is illustrated in Fig.2.18. In this method, the four probes are located around the perimeter of the sample, a current is passed along one edge of the sample (I_{12}), and the voltage is measured along the opposite edge (V_{43}). One then switches a voltage probe with a current probe, passes the current along the third edge (I_{32}), and measures the voltage at the fourth edge (V_{41}). In this way, one obtains two resistances, $R_{12,34} = \frac{V_{43}}{I12}$ and $R_{32,41} = \frac{V_{41}}{I32}$.

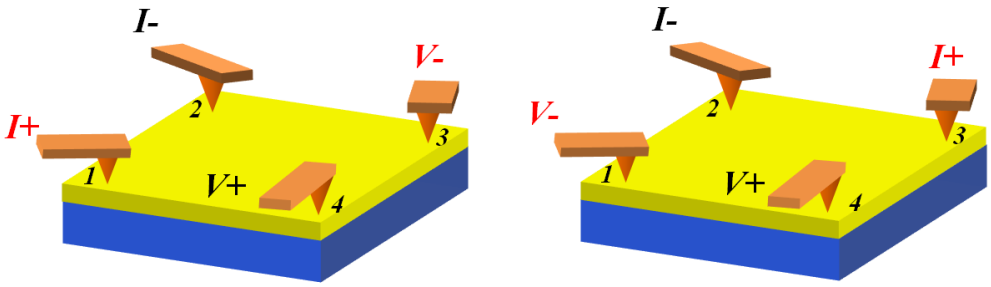

Fig.2.18 Schematic drawing of the Van der Pauw resistivity measurement.

The van der Pauw formula relate the sheet resistance of the material with these resistances as follows:

$$exp\left(-\pi\frac{R_{12,43}}{R_S}\right) + exp\left(-\pi\frac{R_{32,41}}{R_S}\right) = 1$$

This leasd to $$R_S = \frac{\pi}{ln2}\frac{R_{12,43}+R_{32,41}}{2} f\left(\frac{R_{12,43}}{R_{32,41}}\right)$$

Therefore $$\rho = R_S t = t\frac{\pi}{ln2}\frac{R_{12,43}+R_{32,41}}{2} f\left(\frac{R_{12,43}}{R_{32,41}}\right)$$

f is the van der Pauw factor, define $r = \frac{R_{12,43}}{R_{32,41}}$, the relation between f and r is

$$\frac{r-1}{r+1} = \frac{f}{ln2} cosh^{-1}\left[\frac{exp(ln2/f)}{2}\right],$$

and the numeric solution to the equation is shown in Fig.2.19.

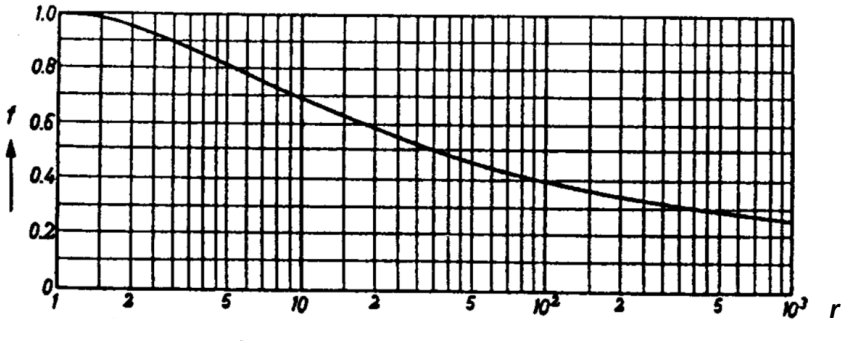

Fig.2.19 Numerical solution for $\frac{r-1}{r+1} = \frac{f}{ln2} cosh^{-1}[\frac{\exp(ln2/f)}{2}]$

Transverse Resistivity

The transverse resistivity (ρ_{xy}) is obtained when voltage is measured in the direction transverse to the current, as shown in Fig.2.20. To achieve a better alignment of the voltage probes, a Hall bar structure is usually used. With an out-of-plane magnetic field, this geometry measures the Hall resistivity, and with an in plane magnetic field, this geometry measures the planar Hall resistivity.

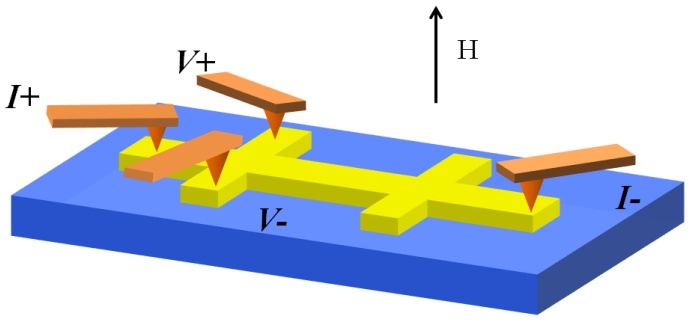

Fig.2.20 Schematic drawing of the Hall measurement.

2.8.2 Magneto-Thermal Transport Measurement

In a thermo-electrical transport measurement, an electric current is driven by a temperature gradient. In the the author's measurements of the spin Seebeck effect, the sample was placed between a resistive heater and a Cu heat sink to establish a constant vertical temperature gradient across the sample. Cu wires were indium-bonded to the surface of the thin film to measure the generated voltage. An inplane field is supplied by an external electromagnet, as shown in Fig.2.21.

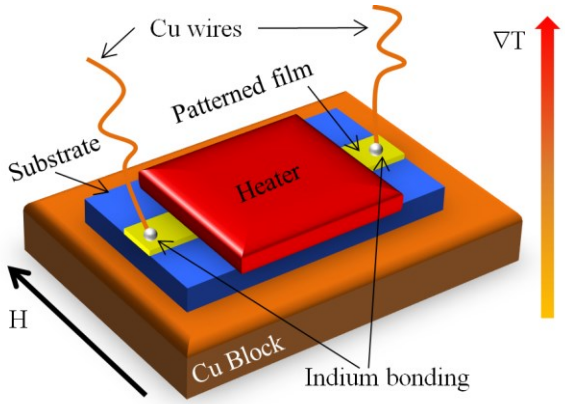

Fig.2.21 Schematic drawing of the thermal spin injection measurement.

2.9 Low Temperature Systems

When the temperature approaches absolute zero, excitations such as phonons and magnons freeze out.[7] The low temperature systems used in this dissertation include a physical property measurement system (PPMS), a superconducting quantum interference device (SQUID) and a closed-cycle cryostat combined with an external electromagnet. The PPMS and SQUID use liquid cryogens to reach low temperatures. The boiling temperature is 77 K for liquid nitrogen and 4.2 K for liquid helium. Usually, a proportional-integral-derivative (PID) temperature feedback loop is used to control the

temperature by adjusting the flow rate of the cryogen into the system. The closed-cycle cryostat does not consume liquid cryogens, and is cooled by thermal conduction with a cold head kept at around 4 K. The cold head works with the helium gas under the Stirling cycle of gas expansion and compression by a compressor.

Reference to Chapter 2

1. W. R. Grove, “on the electro-chemical polarity of gases”, Phil. Trans. R. Soc. Lond. **142**, 87 (1852)
2. D. L. Smith, “Thin film deposition”, McGraw-Hill, Inc., New York (1995)
3. K. Jousten, “Handbook of vacuum technology”, John Wiley & Sons, New York, (2008)
4. B. D. Cullity and S. R. Stock, “Elements of X-ray Diffraction”, Addison Wesley, London (1978)
5. G. Binnig, C. F. Quate, and Ch. Gerber, “Atomic Force Microscope”, Phys. Rev. Lett. **56**, 930 (1986)
6. S. Foner, “Versatile and Sensitive Vibrating-Sample Magnetometer” Rev. Sci. Instrum. **30**, 548 (1959)
7. Charles Kittel, “Introduction to Solid State Physics”, John Wiley & Sons, New York (2004)

Chapter 3

Spin Current, Spin Hall Effect and Inverse Spin Hall Effect

3.1 Introduction

An electron carries a negative electric charge and a spin angular momentum, which is often described in analogy to the rotation of a classical particle around some axis, thus the name. However, there is no classical analog since electron has no measurable size to execute mechanical spinning. Spin is purely quantum mechanical in nature, and it is an intrinsic property of the electron.

The first experimental demonstration of electron spin was the Stern-Gerlach experiment in 1922, where silver atoms traversing through an inhomogeneous magnetic field are split into two discrete symmetrically located components, one displaced upward and the other downward. That result established the value of a magnetic moment, and indicated the existence of a non-integer angular momentum even before Uhlenbeck and Goudsmit introduced the concept of spin in 1925. Later in 1928, Paul Dirac developed a relativistic version of quantum mechanics, establishing a solid theoretical foundation for the spin. An electron has intrinsic angular momentum of $\pm\hbar/2$ and spin magnetic moment of $\pm\mu_B$, projected on a given axis. [1]

They say the Higgs boson is the God's particle. That may be so. But the most important particle for technologies is the electron. Modern electronics manipulates only

the electronic charges, whereas magnetism, superconductivity, and many other important solid-state properties are the results of the charge and spin of electrons. In this chapter, the concept of spin current, spin Hall effect and various important phenomena of pure spin current are introduced. If one can control the spin orientation of the electrons, there are new physics and new phenomena to explore. More importantly, that would open up technological applications.

3.2 Pure Spin Current

3.2.1 Charge Current and Spin Polarized Current

A moving electron transports its -*e* charge in the direction of motion and also a spin angular momentum of quantum number ½ . For a stream of electrons with random spin orientations, such as the current in a common electric wire, no net angular momentum is transported, only electric charge. In such instances, the spin ½ of the electron plays no role; might as well have spin 0. In a non-magnetic metal, such Cu and Au, electron bands are degenerate in spin. Because there are equal number of spin-up and spin-down electrons, only a charge current with no spin polarization flows out of a non-magnetic metal as shown in Fig 3.1(a). However, the electric current that flows out of a ferromagnetic metal can be substantially spin-polarized because there are different numbers of spin-up and spin-down electrons at E_F. The exiting current has spin polarization $P = (N_\uparrow - N_\downarrow)/(N_\uparrow + N_\downarrow)$, where $N_\uparrow$ and $N_\downarrow$ are the densities of electron states for the spin-up and spin-down bands at E_F, respectively, as shown in Fig 3.1(b). In

the extreme case of a half metal, where there is only one spin band at E_F, $P = 1$, i.e., all the electrons have the same spin direction, creating a fully spin polarized current.

In the above cases, a spin current may or may not exist, but a charge current is always present. The only question is whether it is a pure charge current, a spin-polarized current, or a fully spin polarized current. It should also be noted that in all of these cases, a charge current can be generated by ordinary electrical means, for example, by applying a voltage.

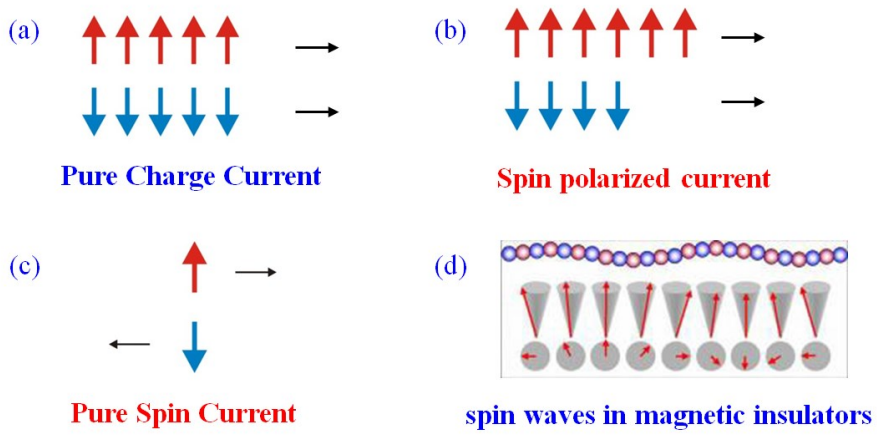

Fig. 3.1 (a) Pure charge current consisting of *10* electrons with *5* up spin and *5* down spin. (b) Spin polarized current consisting of *10* electrons with *6* up spin and *4* down spin, carrying an angular momentum of $2 \cdot \frac{\hbar}{2}$. (c) Pure spin current consisting of *2* electrons with opposite spins moving in the opposite direction, carrying an angular momentum of $2 \cdot \frac{\hbar}{2}$. (d) Magnon spin current, spin waves in magnetic insulators, carrying an angular momentum of $\hbar$.

3.2.2 Pure Spin Current and its Attributes

Suppose we can compel equal number of electrons with opposite spins to move in *opposite* directions. In this case there is only a pure spin current carrying angular momentum but with no net charge flow, as illustrated in Fig.3.1 (c). A pure spin current

differs from all the cases mentioned above because there is no net charge current. In fact, by comparing with the spin polarized current, as shown in Fig. 3.1 (b), a pure spin current, in Fig. 3.1 (c), carries the same amount of angular momentum but using the least amount of electrons. Therefore, the pure spin current generates the *least* amount of Joule heat. This is why pure spin current phenomena and devices are so important in future spintronic devices, high performing and energy efficient.

Moreover, a pure spin current can even transmit in a magnetic insulator where there are no charge carriers at all. In a magnetic insulator, the magnons, or quantized spin waves, can carry the spin current. The magnon is a quasiparticle, a collective excitation of electron spins in a magnetic solid, as shown in Fig. 3.1(d). The spin of a magnon is one, and therefore magnons are bosons.

3.2.3 Spin Diffusion Length

In the Drude model, electrons are pictured as moving ballistically between collisions, and the average distance between collisions of a moving electron is the mean free path, Fig.3.2 (a). Similarly, the average distance between spin-flip collisions of a moving electron is the spin-flip length, Fig.3.2 (b). In contrast, spin diffusion length is the decay length of non-equilibrium magnetization, where it obeys a diffusion equation $\nabla^2(n_\uparrow - n_\downarrow) = \frac{1}{\lambda^2}(n_\uparrow - n_\downarrow)$, and $\lambda = \sqrt{D\tau_s}$ is the spin diffusion length, here $\tau_s$is the spin life time and *D* is the diffusion constant, n is the electron concentration . Generally, the spin diffusion length is larger than the electron mean free path due to both spin-flipping and spin conserving collisions.

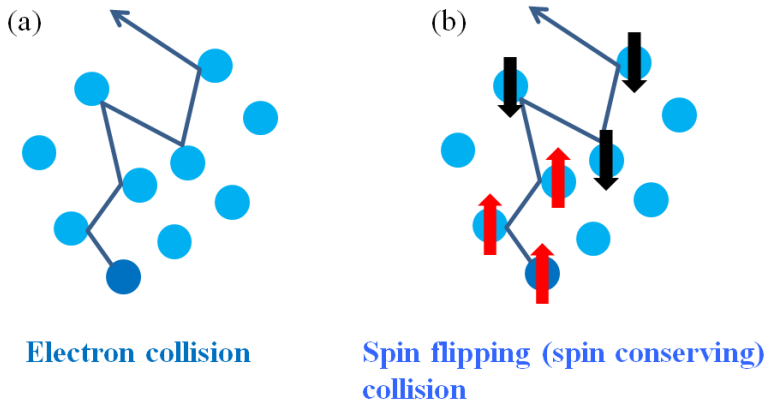

Fig. 3.2 (a) Schematic drawing of electron mean free path. (b) Schematic drawing of spin diffusion length.

The spin diffusion length of each material depends on its spin-orbit coupling strength, and on the concentration of impurities and defects. For single-crystal semiconductors with low spin-orbit coupling such as GaAs, the spin diffusion length can be very long, a few micrometers or even longer. [2] For metal thin films with strong spin-orbit coupling, the spin diffusion length can vary from less than a few nanometers to a few tens of nanometers. Cu is usually regarded as a metal with a very long spin diffusion length of the order of *500 nm* and has been widely used in spintronic devices as a spin current conductor. The impurity scattering is also important in determining the spin diffusion length, therefore different samples made from the same material can have different spin diffusion lengths. Because of the short spin diffusion length in most metals, nanostructures are required for exploring pure spin current phenomena.

The spin diffusion length can be measured by various techniques; for example, the current-perpendicular to plane (CPP) magnetoresistance, lateral-non-local spin valve, weak localization, and others.

3.2.4 Generation of Pure Spin Current

Charge current can be driven by electrical field, temperature gradient, photo-excitations, mechanical forces and other excitations. It is much more difficult to generate pure spin current. The usual electric means, for generating a charge current, e.g., a voltage, cannot be directly used for generating pure spin current, instead, one needs new phenomena with new physics.

The methods to generate pure spin current include spin diffusion at the interface of ferromagnetic metal (FM) /nonmagnetic metal (NM) [3], spin pumping [4], spin Hall effect [5], and the spin Seebeck effect [6]. Details on the spin Hall effect and the spin Seebeck effect are discussed in Section 3.3 and Chapter 4, respectively. Here we give a brief introduction into other methods of generating a pure spin current.

Nonlocal Spin Valve

Spin current can be generated through the non-equilibrium spin accumulation at the interface of FM/NM in the non-local spin valve geometry, as shown in Fig. 3.3 (a) and (b). When a charge current passes through an FM electrode, the densities of electrons for opposite spins at the Fermi level are different, Fig. 3.3 (c), and thus the conductivities for the majority and minority spin electrons are unequal. On the other hand, in NM, the conductivity for spin up and spin down electrons are equal, Fig. 3.3 (c). Because of the sudden change of the spin-dependent conductivity, electrons with a preferred spin orientation accumulate at the FM/NM interface.

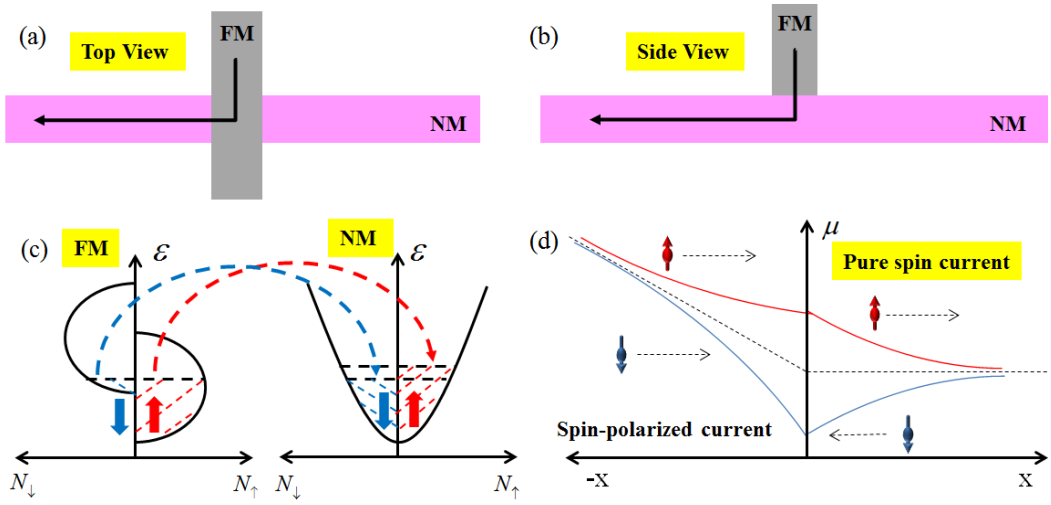

Fig. 3.3 Schematic drawing of the (a) top view and (b) side view of the FM/NM spin valve devices. (c) Illustration of the band structure and Fermi level for the FM and NM materials. (d) Illustration of the spin current and charge current distribution in the FM/NM junction structures.

The spin accumulation can be quantified by the spin-dependent chemical potential μ. The interface spin accumulation results in spin diffusion in NM. Since no charge current passes through NM, the spin diffusion in NM is a pure spin current, Fig. 3.3 (d). In the non-local spin valve method, the pure spin current is analyzed downstream by the inverse spin Hall effect, to be discussed later.

Spin Pumping

Another way to generate spin current is spin pumping in the FM/NM structure, which is the reciprocal effect of the spin transfer torque, and in spin pumping the precessing magnetic moment generates pure spin current in the attached nonmagnetic layer, Fig. 3.4. The equation that describes this process is

$$\boldsymbol{J_0^s} = \frac{\hbar}{8\pi} Re\left(2g^{\uparrow\downarrow}\right)[\hat{m} \times \frac{\partial \hat{m}}{\partial t}],$$

Where $Re(\ g^{\uparrow\downarrow})$ is the real part of the spin-mixing conductance, $\hat{m}$ is the unit vector of the magnetization of the ferromagnet. As we will see different from the electrical spin injection in the non-local spin valve, spin pumping can pump spin into a non-magnetic conductor from a ferromagnetic insulator via the magnetization dynamics.

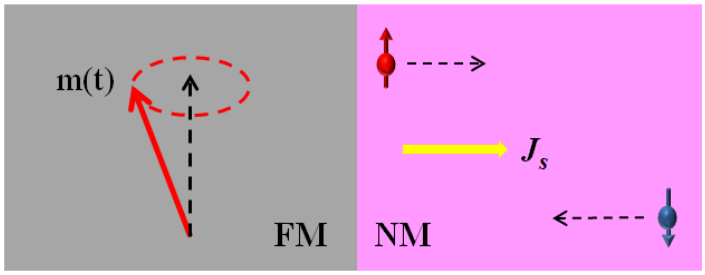

Fig. 3.4 Schematic drawing of the spin pumping in FM/NM structures.

3.2.5 Detection of Pure Spin Current

A pure spin current, not accompanied by a charge current, cannot be directly detected by conventional electrical methods. The main technique, the inverse spin Hall effect, is an indirect method discussed in the next section. Here, we briefly mention other methods that can be used to detect pure spin current: the magneto-optic Kerr effect (MOKE) [7] and the spin transfer torque effect (STT) [8, 9].

Magneto-Optic Kerr Effect (MOKE)

As a result of the pure spin current, equal amount of electrons with opposite spin are accumulated on opposite side of the specimen. The spin accumulation can be detected optically using magneto-optic Kerr effect (MOKE) if the spin separation is larger than the optical wavelength. Only high quality semiconductors can meet this stringent requirement.

The physical origin of MOKE is the magnetic circular dichroism effect, where the absorption of left and right circularly polarized light differs in materials with nonzero spin polarizations. In a MOKE measurement, linearly polarized or elliptically polarized light is hitting the sample surface, and the reflected light from the spin polarized/magnetized surface changes its original polarization and intensity. Therefore, incident light experiences a rotation of its polarization plane. Measuring the change of the polarization of the reflected light provides information about the spin polarization/magnetization state of the sample. MOKE detection of the pure spin current was first demonstrated in semiconductor GaAs and InGaAs. This experiment was also the first experimental detection of the spin Hall effect, as shown in the Fig. 3.5. Although optical methods are successful in detecting spin accumulation in high-quality semiconductors, this approachcannot be extended to metallic systems because of the short spin diffusion length in metals with strong spin-orbit coupling.

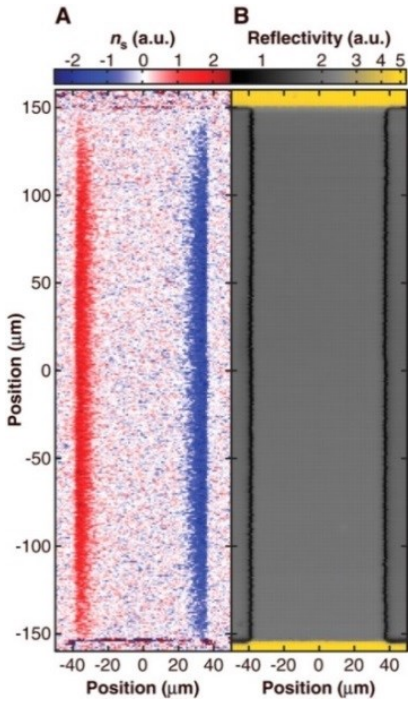

Fig. 3.5 Experimental observation of the spin Hall effect in semiconductor GaAs by MOKE microscope. (Figure is obtained from Ref. [7])

Spin Transfer Torque (STT)

An alternative way to detect pure spin current is through the spin transfer torque which transfers angular momentum from spin current to the magnetization of FM layer. In magnetic heterostructures, when spin current is generated in the non-magnetic layer through the spin Hall effect, the spin current diffuses into the FM layer causing the dynamical steady-state precession of the magnetic moment. When the spin current is large enough, the magnetization of the FM layer can be switched, Fig. 3.6. The transverse (to magnetization) component of spin (spin index $\hat{\sigma}$) can be absorbed by the FM (magnetization direction $\hat{m}$). The torque per unit moment can be written as

$$\vec{\tau}_{ST} = \frac{\hbar}{2eM_S t} J_s[(\hat{m} \times \hat{\sigma}) \times \hat{m})] \text{ (Equation is obtained from ref. [9])}$$

where M_S is the saturation magnetization of the FM layer, t is its thickness and J_S is the spin current. By analyzing the magnetization dynamics through spectroscopy of the ferromagnetic resonance or through the detection of the magnetization switching, one infers the presence of a spin current in the NM layer.

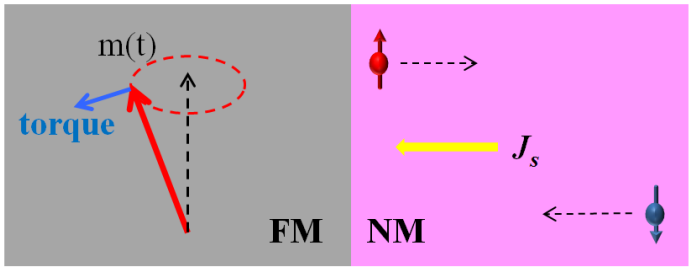

Fig. 3.6 Schematic drawing of the spin transfer torque in the FM/NM structures.

3.3 Spin Hall Effect and Inverse Spin Hall Effect

The spin Hall effect and the inverse spin Hall effect are two widely used electrical methods to generate and detect pure spin current. The concept of the spin Hall effect is closely related to the Hall effects discovered by Edwin Hall. We will first describe the ordinary and anomalous Hall effects before discussing the spin Hall effect. [10]

3.3.1 Hall Effects

The Hall effect was discovered by Edwin Hall in 1879, 18 years before the electron was discovered, while he was working towards his doctoral degree at the Johns Hopkins University. In the ordinary Hall effect, when a charge current passes through a conductor,

under an out-of-plane magnetic field, the charge carriers are deflected by the Lorentz force and accumulated at the edges, creating a transverse electric field, Fig. 3.7(a).

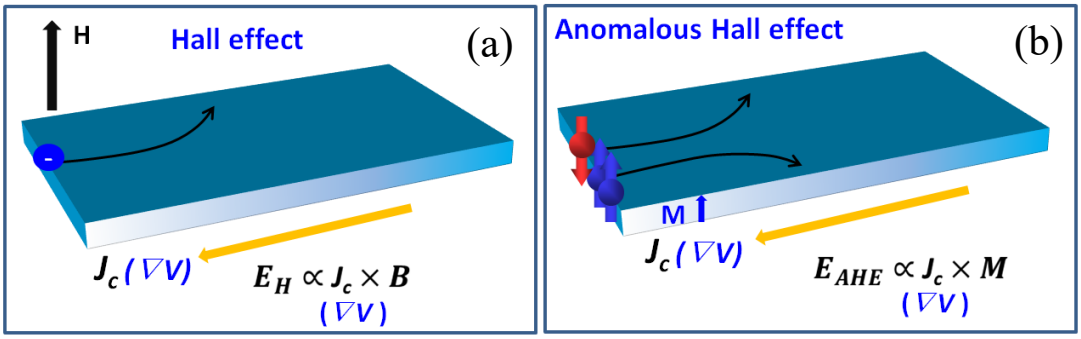

Fig. 3.7 (a) Schematic drawing of the Hall effect. (b) Schematic drawing of the anomalous Hall effect.

An important physical quantity in this context is the Hall resistivity, defined as the ratio of the transverse electric field to the current, $\rho_{xy} = \frac{E_y}{J_x}$. For the ordinary Hall effect, the Hall resistivity can be deduced from the Drude Model. The drift velocity of a charge carrier in an electric field is $\vec{v} = \frac{q\vec{E}\tau}{m}$, where q is the charge, E is the electric field, τ is the relaxation time, m is the mass of the charge carrier. The Lorentz force experienced by charge carrier under a perpendicular magnetic field B is $q(\vec{v} \times \vec{B})$. This force induces a transverse velocity of

$$v_y = \frac{qE_y\tau}{m} + \frac{\tau q}{m}(\vec{v} \times \vec{B})_y.$$

Therefore the total charge current flows in a material under a perpendicular magnetic field can be written as

$$\vec{J} = nq\vec{v} = \frac{nq^2\tau}{m}\vec{E} + \frac{\tau q}{m}\left(nq\vec{v} \times \vec{B}\right) = \sigma\vec{E} + \frac{\tau q}{m}(\vec{J} \times \vec{B}),$$

where $\sigma = \frac{nq^2\tau}{m}$, n is the charge carrier density. The transverse charge accumulation reaches a limit when a transverse electric field is established balancing the charge carriers moving transversely, resulting $J_x = \sigma E_x$ and $J_y = \sigma E_y - \frac{\tau q}{m} J_x B = 0$. This gives

$$E_y = \frac{1}{nq} J_x B,$$

from the Hall resistivity is

$$\rho_{xy} = \frac{E_y}{J_x} = \frac{B}{nq},.$$

The Hall resistivity is proportional to the external magnetic field inversely proportional to the carrier density, and is independent of the relaxation time τ. The Hall effect can thus be used to measure the magnetic field using a material with a known density of charge carriers (n) or to determine n in conductors, especially in semiconductors using a magnetic field of known strength.

3.3.2 Anomalous Hall effect

Two years after the discovery of the ordinary Hall effect, in 1881, Edwin Hall reported that the signal was ten times larger in the ferromagnetic iron, which is known as the anomalous Hall effect (AHE). Although the anomalous Hall effect has been observed a century ago, the physical mechanisms responsible for it has been elucidated only in recent times.

When a charge current passes through a ferromagnet with out-of-plane magnetization, electrons of opposite spins (present in unequal numbers) are deflected in the transverse directions and accumulated at the edges through the relativistic spin-orbit interaction, Fig. 3.7(b). For materials that exhibit the AHE, the transverse resistivity is $\rho_{xy} = R_0 B + 4\pi R_S M_Z$, where the first term is from the ordinary Hall effect that depends on the external magnetic field, $R_0 = 1/nq$ with q as the charge of the charge carrier, and n the density of charge carriers. The second term is the contribution from magnetization; the coefficient R_S depends on the material. There are three mechanisms that contribute to R_S : an intrinsic contribution, skew scattering and the side jump. See Sec. 3.3.4.

3.3.3 Spin Orbit Coupling, Spin Hall effect and Inverse Spin Hall Effect

The spin Hall effect (SHE) and the inverse spin Hall (ISHE) effect are two key effects widely used in the pure spin current phenomena and both are driven by spin-orbit interactions. In the following we provide a pictorial way to describe the spin-orbit interaction, spin Hall effect and inverse spin Hall effect.

Spin Orbit Coupling in Atoms

In atomic physics, consider an electron orbiting an atomic nucleus. In the *rest frame* of the electron, the positively charged and moving nucleus creates a magnetic field. The electron spin is coupled to the magnetic field. This is the physical origin of the spin-orbit coupling. [11]

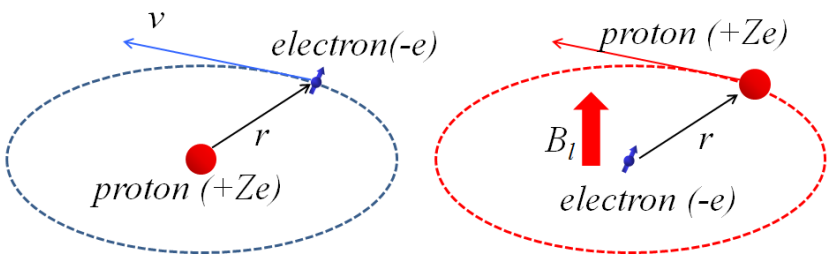

Fig. 3.8 Schematic drawing of the electron (with negative charge -*e*) moving around proton (with positive charge +*Ze*, *Z* is the atomic number) (left) and in the rest frame of electron, the proton moving around electron, generating a relativistic magnetic field affecting the electron spin.

Thus, in the rest frame of electron, due to the relativistic effect, the magnetic field seen by the electron is

$$\vec{B}_l = \frac{Ze\mu_0}{8\pi r^3 m_0}\vec{l}$$

And the magnetic potential energy of the spin-orbit coupling is

$$V_{l,s} = \frac{Ze^2\mu_0}{8\pi r^3 {m_0}^2}(\vec{s}\cdot\vec{l})$$

Here, *Z* is the atomic number, -*e* is the electron charge, and *Ze* is the charge carried by the proton, μ_0 is the vacuum permeability, *r* is the distance from the electron to proton, *v* is the relative tangential velocity between electron and proton. Therefore, we can conclude that element with larger *Z* (atomic number) and with a shorter *r* (electron to proton distance), has stronger spin-orbit coupling.

Spin Orbit Coupling in Solids

Similar to the SOC in an atom, in solids, electrons move across the lattices experience the electric field given by the gradient of the crystal potential ($\vec{E} = -\vec{\nabla}V$), and in their rest frame they feel the effective magnetic field, which deflect electrons with opposite directions of spins in opposite directions.

From a coarse-grained low energy view, the SOC in solids exists in crystals with broken inversion symmetry, such as the Dresselhaus interaction from bulk induced asymmetry, and the Bychkov-Rashba type interaction from surface induced asymmetry. Due to the breaking of symmetry, for example in the Rashba effect, a vertical to the surface electric field exists, and similarly, electrons moving in this electric field experience an effective magnetic field, results in spin-orbit interaction in these systems. [12, 13]

Spin Hall Effect and Inverse Spin Hall Effect

The spin Hall effect (SHE) was first predicted by Dyakonov and Perel in 1971 but attracted little or no attention until 1999, when Hirsch rediscovered the effect and gave it the name universally adopted by the community. [5, 14] The SHE is different from the ordinary Hall effect and the AHE; it occurs in a *non-magnetic* metal with strong SOC. When charge current flows in the material, without external magnetic field, equal numbers of electrons with opposite spins are deflected by relativistic spin orbit interaction in the transverse directions. Spins accumulate at the edges. Therefore, this

effect *cannot* be directly detected by electrical means, Fig. 3.9(a). Details of the scattering mechanisms are discussed in section 3.3.4.

The inverse spin Hall effect (ISHE) is the reciprocal effect of the spin Hall effect. The spin orbit interaction process, the same as in the spin Hall effect, converts the spin current into a charge current. Charges accumulate at the edges. Therefore, the ISHE allows electrical detection of pure spin current, Fig. 3.9 (b).

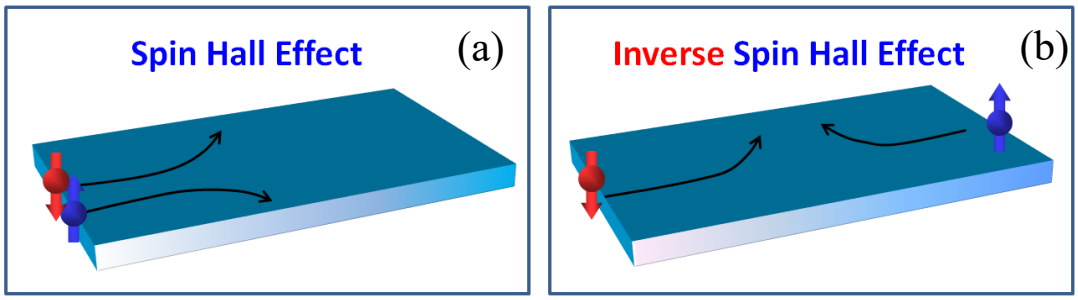

Fig. 3.9 (a) Schematic drawing of the spin Hall effect. (b) Schematic drawing of the inverse spin Hall effect.

3.3.4 Deflection Mechanisms

Three distinct mechanisms are responsible for the spin dependent deflection (in SHE, ISHE, and AHE): intrinsic deflection, skew scattering and side jump. , Fig. 3.11 [15]

Intrinsic Deflection

The intrinsic deflection was first derived by Karplus and Luttinger in 1954 to describe the anomalous Hall effect, but its topological nature, related to the Berry phase of an electron in k-space was not fully appreciated until recently[16, 17].

To understand the concept of the Berry phase, we first describe the parallel transport of a vector along a contour in curved space. Suppose a vector $\vec{v}$ is travelling along a closed path *C,* and $\vec{n}$ is the normal axis to the local tangential plane, there are two constrains the vector has to obey:

1. the vector must lie in the local tangential plan ($\vec{v} \cdot \vec{n} = 0$)
2. the vector must not twist along its local tangential plane normal axis ($d\vec{v} \times \vec{n} = 0$)). This is known as "parallel transport".

For a vector $\vec{v}$ travelling on a *plane* from 1->2->3->1, as shown in Fig.3.10(a), since $\vec{n}$ always points to the same direction at any point on the flat plane, $\vec{v}$ gains no geometric phase when it travels back to 1.

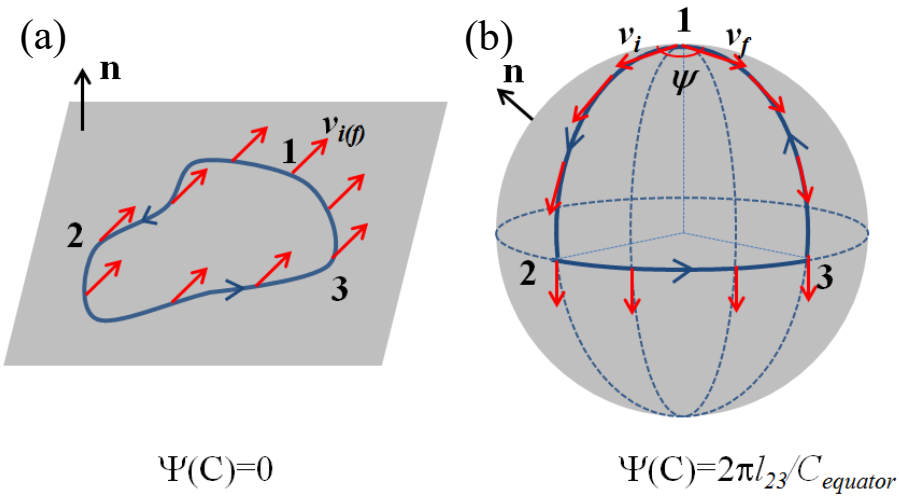

Fig. 3.10 (a) Schematic drawing of a vector moving on a plane. (b) Schematic drawing of a vector moving on a sphere.

However, in a curved space, for example, on the surface of a sphere, Fig. 3.10(b), when the vector travels around a loop 1-2-3-1. After parallel transport around the loop,

vector $\vec{v}$ rotates in the tangential plane through angle ψ. In the special case described in Fig. 3.10(b), $\psi = 2\pi \frac{l_{23}}{C_{equator}}$, where l_{23} is the length of arc 2->3, and $C_{equator}$ is the circumference of the equator. Generally, the rotation angle equals the solid angle subtended by the loop.

The geometrical phase (also known as the Berry phase) concept was introduced by Michael Berry in 1984 to emphasize its importance in the frame of quantum physics. In a quantum system with Hamiltonian $\widehat{H}(\boldsymbol{R})$ and eigenstates $|n, \boldsymbol{R}>$, where n labels the level of the Hamiltonian and $\boldsymbol{R}$ is a set of parameters. Suppose an electron is initially in the eigenstate $|n, \boldsymbol{R}>$with eigenvalue $\mathcal{E}_n(\mathbf{R})$**,** denoted by $|\psi_n>$, and it keeps the same energy $\mathcal{E}_n(\mathbf{R})$ when $\widehat{H}(\boldsymbol{R}(t))$ undergoes adiabatic changes controlled by parameter $\boldsymbol{R}(t)$ (varies with time t). When the system eventually returns back to its original form (completing a closed path C in the parameter space), the eigenstates $|n, \boldsymbol{R}(t)>$ change along the path and return back to their initial values. However, the electron system eigenstate $|\psi_n(t)>$ does not return to its original form, but instead it acquires an additional phase $\gamma(C)$, such that

$$|\psi_n(t)>= e^{i\gamma(C)} e^{-\frac{i}{\hbar}\int_0^t dt' \mathcal{E}_n(\boldsymbol{R}(t'))} |n, \boldsymbol{R}(t)>.$$

Here, the second exponential term is the dynamic phase term, and the first exponential term $\gamma(C)$ is the Berry phase, which depends on the path C. It can be related to the parallel transport that $|\psi>$ gains a phase upon completing a closed path C.

In the calculation of Hall conductivity, in electron system with non-zero Berry phase, the electron group velocity is $\hbar\mathbf{v} = \boldsymbol{\nabla_k}\varepsilon_n(k) + \frac{\partial V}{\partial \boldsymbol{x}} \times \boldsymbol{\Omega}(\boldsymbol{k})$, where $\varepsilon_n(k)$ is the

energy of electron for n^{th} band. The second term, $\Omega(k)$, the Berry phase curvature in momentum space, equals to $\nabla_k \times X(k)$, where $X(k)$ is the Berry vector potential related to the Berry phase in momentum space $\chi(k) = -\int_C^k dk' X(k')$.

The AHE conductivity of a translationally invariant electron gas is

$$\sigma'_{xy} = n\frac{e^2}{\hbar} < \Omega >,$$

where $< \Omega > \equiv n^{-1} \sum_k \Omega_z(k) f_k^0$ is the weighted average of the Berry phase curvature. Here, *n* is the electron density and f_k^0 is the equilibrium Fermi-Dirac distribution function. [18] This expression is known as the intrinsic anomalous Hall conductivity, reflecting the topology of electron bands. Corrections resulting from scattering by impurities and defects are considered extrinsic effects.

The intrinsic Hall conductivity does not depend on electrical conductivity of the material nor on the Bloch state lifetime τ, $\sigma_{xy} \propto const.$ It is proportional to the integration over the Fermi sea of the Berry curvature of each occupied band. The intrinsic deflection can be evaluated accurately even for complex materials in theoretical studies.

Skew Scattering

Skew scattering is due to the spin-orbit interaction with *impurities*, Fig. 3.11 (b). [15] When an electron approaches an impurity with electric potential, in the rest frame of the electron, the moving impurity generates an effective magnetic field, which scatters

electrons with opposite spins in opposite directions. The skew scattering contribution to the spin Hall effect can be defined as the contribution that is proportional to the Bloch state transport lifetime and to the longitudinal charge conductivity of the material, $\sigma_{xy} \propto \sigma_{xx}$

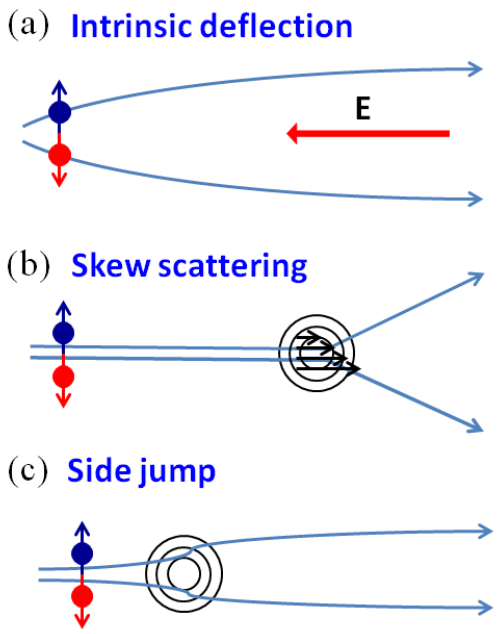

Fig. 3.11 Schematic drawing of (a) intrinsic deflection, (b) skew scattering and (c) side jump.

Side Jump

The side jump contribution to the spin Hall effect is from the transverse velocity obtained by electron upon approaching and leaving an *impurity*. [15] The side jump conductivity can be calculated as the scattering of a Gaussian wavepacket from a spherical impurity with spin orbit interaction. The side jump conductivity has similar feature of the intrinsic deflection that it does not depend on the charge conductivity and the Bloch electron life time. Normally, the side jump contribution is the smallest among the three scattering

mechanism, but it may be dominant at high impurity concentration sample due to repeated scattering.

The scaling behavior of anomalous Hall effect, experimentally verified by T. Miyasato et al. [19] showed that in the superclean metal regime (σ_{xx} >10^6 Scm), the skew-scattering dominates over the intrinsic contribution because of $\sigma_{xy} \propto \sigma_{xx}$. The intrinsic deflection dominates in the moderately dirty metal regime (10^4 Scm <σ_{xx} <10^6 Scm) because of $\sigma_{xy} \propto const.$, as shown in Fig. 3.12.

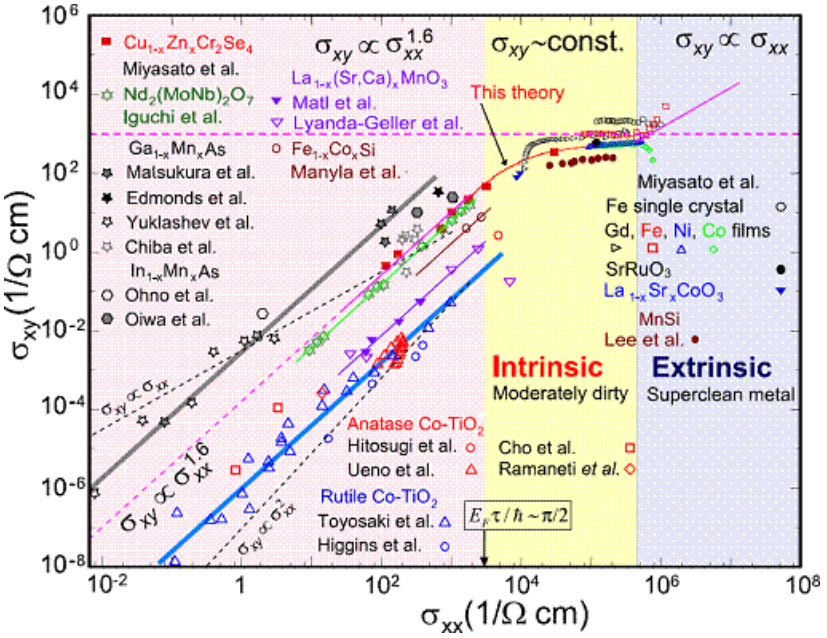

Fig.3.12 Absolute value of anomalous Hall conductivity σ_{xy} as a function of longitudinal conductivity σ_{xx} in ferromagnets. [Figure is obtained from S. Onoda's homepage at riken.jp]

3.3.5 Nernst Effect

The Nernst effect is a thermo-electric version of the Hall effect, in which the role of electric field is played by a temperature gradient, Fig. 3.13. All of the different varieties of the Hall effect (ordinary, anomalous, etc.) have a Nernst counterpart.

The anomalous Nernst voltage is proportional to the cross product $\nabla T \times \boldsymbol{m}$ of temperature gradient (∇T) and the magnetization direction m. For a stand alone slab of material, the gradient can be applied in the transverse (in-plane) direction $\nabla_x T$, or in the longitudinal out-of-plane direction $\nabla_z T$. A voltage can be in the direction of $\nabla T \times \boldsymbol{m}$ provided ∇T and $\boldsymbol{m}$ are not collinear. However, for a metal thin film deposited on a thick substrate, the thermal conduction of the film will be overwhelmed by that of the substrate. An intentional in-plane thermal gradient $\nabla_x T$ would inadvertently generate an out-of-plane thermal gradient $\nabla_z T$. [20]

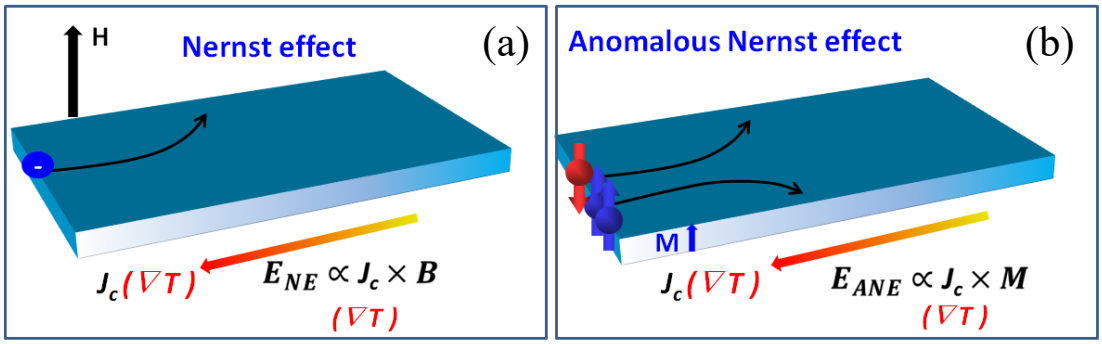

Fig. 3.13 (a) Schematic drawing of the Nernst effect. (b) Schematic drawing of the anomalous Nernst effect.

It is important to note there are numerous electrical insulators, such as MgO, glass, Si, GaAs, etc., whose electric conductivities are ten or more orders of magnitude lower than those of metals. When a metallic thin films is deposited on such an insulating substrate, even though the substrate is typically 10^4 times thicker, the electrical conduction through the substrate is entirely negligible. In contrast thermal conductivities of all solids are roughly similar (within three orders of magnitude). Many electrical insulators are in fact good thermal conductors, with higher thermal conductivities than

those of electrical conductors. For example, the thermal conductivities of semiconductors Si and GaAs are higher than those of metallic Fe and Py. This fact poses serious problems in thermal measurements in general, and especially thermal measurement of thin metal films on thick substrate.

Thus, when performing a spin-dependent thermal measurement of a magnetic thin film on a substrate, one needs to be very careful. The anomalous Nernst effect (ANE) can mix with the spin-dependent thermal signal in a ferromagnetic conductor.

3.4 Spin Hall Angle

The quantity used to measure how much charge current is deflected in the transverse direction in the ordinary Hall effect is the Hall angle.[21] As shown in Fig. 3.14(a), the Hall angle is defined as $tan(\theta_{Hall}) = \frac{J_H}{J_C}$, and can be approximated by $\theta_{Hall} \approx \frac{J_H}{J_C}$ for a small angle. Similarly, the quantity used to measure the conversion efficiency between the charge current and spin current in the SHE and ISHE is known as the spin Hall angle, Fig. 3.14 (b). In the SHE, when charge current is converted to spin current, the spin Hall angle is defined as $\theta_{SH} = \frac{2e}{\hbar}\frac{J_S}{J_C}$. In the ISHE, when spin current is converted to charge current, the spin Hall angle is defined as $\theta_{SH} = \frac{\hbar}{2e}\frac{J_C}{J_S}$. θ_{SH} is a dimensionless quantity.

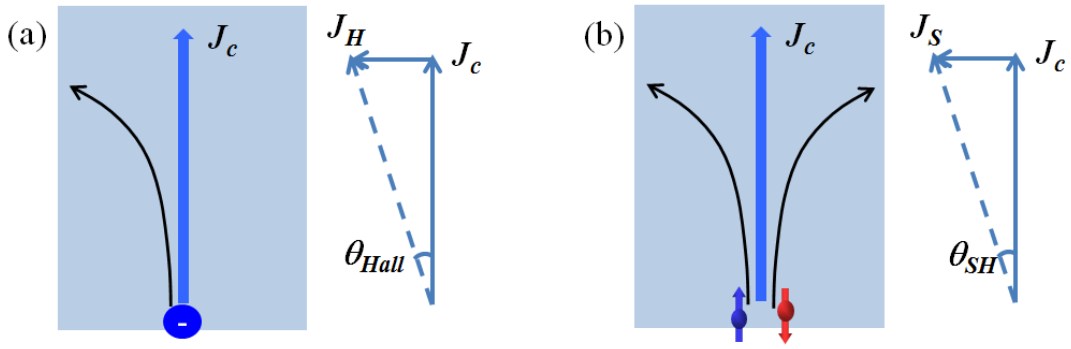

Fig. 3.14 Schematic drawing of the (a) Hall angle and (b) spin Hall angle.

The most outstanding problem for $\theta_{SH}$is the large disparity in the values determined experimentally for the same material. For example, the spin Hall angle in Au determined by different groups using the same or different methods have a large variance from 0.0016 to 0.113[22, 23], as large as two orders of magnitude. The large variances in the spin Hall angles may be a result of different measurement technique and analysis method. Several methods based on the SHE or ISHE to determine spin Hall angle in materials, including the non-local spin valve method [23-25], the spin pumping method [26-29], spin Hall switching method [30- 33] and H-bar method [34] are discussed here.

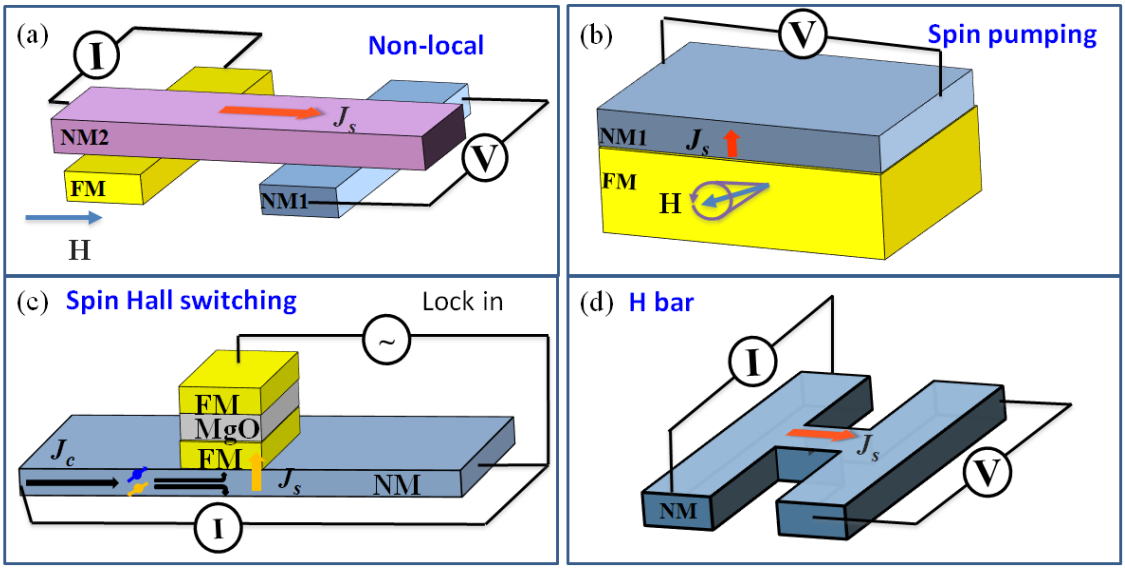

Fig. 3.15 Schematic drawing of (a) non-local spin valve structure, (b) spin pumping in NM/FM structure, (c) spin Hall switching in FM/MgO/FM heterostructure with a spin Hall metal as under layer and (d) H-bar structure.

3.4.1 Non-local Spin Valve Geometry

In the *non-local spin valve* method, Fig. 3.15(a) pure spin current is generated upstream using the spin diffusion method mentioned in Sec. 3.2.4, and then transported downstream using a copper bar as a conduit and analyzed in a spin current detector using the ISHE. [23-25] This method requires sophisticated electron lithography of several materials on very short length scales. Only two or three groups in the world (e.g., Otani at University of Tokyo, Ji at University of Delaware) can perform non-local spin valve measurements. This method also involves a large number of interfaces, all of which may cause complications and are essential for the success. Moreover, the electrical current distribution in the metal/metal non-local spin valve structure complicates the determination of the spin Hall angle because of current shunting.

3.4.2 Spin Pumping Geometry

The *spin pumping* method uses ferromagnetic resonance (FMR) to excite magnon spin current in the FM layer, which may be metallic such as Py, or insulating such as YIG, as has been mentioned in Sec. 3.2.4. The spin current is injected into an attached spin current detector based on the ISHE, Fig. 3.15(b). [26-29] The spin pumping method has been most widely used in determining the spin Hall angle of a material because of its simplicity in spin current generation. On the downside, the method is prone to many parasitic effects in the FM layer, e.g., the anisotropy magnetoresistance, the inverse spin Hall effect (discussed in Chapter 8), or the longitudinal spin Seebeck effect (caused by the FMR radiation). These parasitic effects have an adverse effect on the inferred values of spin Hall angle and spin diffusion length.

3.4.3 Spin-Hall-Switching Geometry

A heterostructure that uses spin current to switch the FM layer magnetization is shown in Fig. 3.15(c). [30- 32] In the spin-Hall-switching geometry, the spin current is generated through the spin Hall effect in the NM and diffuses vertically into the FM junctions. When the spin current reaches density critical value the magnetization of the FM layer is switched. However, the spin Hall angle calculated by this method depends on the thickness of the material, with thinner films usually having higher spin Hall angles. This method also gives very high values for some materials, for instances, the spin Hall angle reported for Bi_2Se_3 is in the order of one. [33] In fact, the switching mechanism in this type of structures is still under intense debate. A potential switching mechanism, the

interfacial Rashba effect, has not been included in the spin Hall angle analysis yet. Furthermore, the FM magnetization switching mechanism may not be a macroscopic spin current switching effect, but rather current-driven domain wall movement.

3.4.4 H-Bar Geometry

The H-bar method uses only one, nonmagnetic material without any ferromagnet in the vicinity, Fig. 3.15(d). [34] The spin current is created in one arm of the H-bar by the SHE and detected in the other arm by the ISHE. This method is limited by the spatial decay of spin current in transfer between the arms. It either requires a material with long spin diffusion length or a small H-bar. Additional complications are the inhomogeneous current distribution and the issue of diffusive vs. ballistic transport.

Although the wildly divergent values of the spin Hall angles obtained by different methods for the same material remain an outstanding issue. The experimentalists at least agree on the sign of the spin Hall angle. The ratios of the spin Hall angles among different materials using the same method appear to be converging. During the course of this PhD project, we have developed another consistent method based on the longitudinal spin Seebeck effect to explore pure spin current phenomena, including the determination of the spin Hall angle and spin diffusion length, which also has its own complications and pitfalls, as we describe in chapter 7.

Reference to Chapter 3

1. D. J. Griffiths, “Introduction to Quantum Mechanics”, Pearson Prentice Hall, New Jersey (2005)
2. J. Bass and W. P. Pratt Jr., “Current-perpendicular (CPP) magnetoresistance in magnetic metallic multilayers”, J. Magn. Magn. Mater. **200**, 274 (1999)
3. F. J. Jedema, A. T. Filip, and B. J. Van Wees, “Electrical spin injection and accumulation at room temperature in all-metal mesoscopic spin valve”, Nature **410**, 345 (2001)
4. E. Saitoh, M. Ueda, H. Miyajima and G. Tatara, “Conversion of spin current into charge current at room temperature: Inverse spin Hall effect”, Appl. Phys. Lett. **88**, 182509 (2006)
5. J. E. Hirsch, “Spin Hall effect”, Phys. Rev. Lett. **83**, 1834 (1999)
6. K. Uchida, S. Takahashi, K. Harii, J. Ieda, W. Koshibae, K. Ando, S. Maekawa, and E. Saitoh, “Observation of the spin Seebeck effect”, Nature, **455**, 778 (2008)
7. Y. K. Kato, R. C. Myers, A. C. Gossard and D. D. Awschalom, “Observation of the spin Hall effect in semiconductors”, Science **10**, 1910 (2004)
8. D. C. Ralph and M. D. Stiles, “Spin transfer torques”, J. Magn. Magn. Mater. **320**, 1190 (2008)
9. L. Liu, O. J. Lee, T. J. Gudmundsen, D. C. Ralph, and R. A. Buhrman, “Current-induced switching of perpendicularly magnetized magnetic layers using spin torque from the spin Hall effect”, Phys. Rev. Lett. **109**, 096602 (2012)

10. C. L. Chien and C. R. Westgate, “The Hall effect and its applications”, Plenum Press, New York (1980)
11. M. Born, “Atomic Physics”, Dover Publications Inc, New York (1989)
12. G. Dresselhaus, “Spin-orbit coupling effects in zinc blende structures”, Phys. Rev. **100**, 580 (1955),
13. E. Rashba, “Properties of semiconductors with an extremum loop”, Sov. Phys. Solid State **2**, 1109 (1960)
14. M. I. Dyakonov and V. I. Perel, “Current-induced spin orientation of electrons in semiconductors”, Phys. Lett. **A35**, 459 (1971)
15. N. Nagaosa, J. Sinova, S. Onoda, A. H. MacDonald, and N. P. Ong, “Anomalous Hall effect”, Rev. Mod. Phys. **82**, 1539 (2010)
16. R. Karplus, J. M. Luttinger, “Hall effect in ferromagnetics” Phys. Rev. **95**, 1154 (1954)
17. M. V. Berry, “Quantal phase factors accompanying adiabatic changes”, Proc. R. Soc. Lond. A **392**, 45 (1984)
18. N. P. Ong and W. –L. Lee, “Geometry and the anomalous Hall effect in ferromagnets”, arXiv:0508236v1(2005)
19. T. Miyasato, N. Abe, T. Fujii, A. Asamitsu, S. Onoda, Y. Onose, N. Nagaosa, and Y. Tokura, “Crossover behavior of the anomalous Hall effect and anomalous Nernst effect in itinerant ferromagnets”, Phys. Rev. Lett. **99**, 086602 (2007)
20. S. Y. Huang, W. G. Wang, S. F. Lee, J. Kwo, and C. L. Chien, “Intrinsic spin-dependent thermal transport”, Phys. Rev. Lett. **107**, 216604 (2011)

21. J. Sinova, S. O. Valenzuela, J. Wunderlich, C. H. Back, and T. Jungwirth, “Spin Hall effect”, Rev. Mod. Phys. **87**, 1213 (2015)

22. T. Seki, Y. Hasegawa, S. Mitan, S. Takahashi, H. Imamura, S. Maekawa, J. Nitta and K. Takanashi, “Giant spin Hall effect in perpendicularly spin-polarized FePt/Au devices”, Nature Mater., **7**, 125 (2008)

23. T. Kimura, Y. Otani, T. Sato, S. Takahashi and S. Maekawa, “Room-temperature reversible spin Hall effect” Phys. Rev. Lett. **98**, 156601 (2007).

24. S. O. Valenzuela and M. Tinkham, “Direct electronic measurement of the spin Hall effect”, Nature (London) **442**, 176 (2006).

25. M. Morota, Y. Niimi, K. Ohnishi, D. H. Wei, T. Tanaka, H. Kontai, T. Kimura, and Y. Otani, “Indication of intrinsic spin Hall effect in *4d* and *5d* transition metals”, Phys. Rev. B **83**, 174405 (2011).

26. K. Ando, S. Takahashi, K. Harii, K. Sasage, J. Ieda, S. Maekawa, and E. Saitoh, “Electric manipulation of spin relaxation using the spin Hall effect”, Phys. Rev. Lett. **101**, 036601 (2008).

27. O. Mosendz, J. E. Pearson, F. Y. Fradin, G. E. W. Bauer, S. D. Bader, and A. Hoffmann, “Quantifying spin Hall angles from spin pumping: experiments and theory”, Phys. Rev. Lett. **104**, 046601 (2010)

28. O. Mosendz, V. Vlaminck, J. E. Pearson, F. Y. Fradin, G. E. Bauer, S. D. Bader, and A. Hoffmann, “Detection and quantification of inverse spin Hall effect from spin pumping in permalloy/normal metal bilayers”, Phys. Rev. B, **82**, 214403 (2010).

29. Z. Feng, J. Hu, L. Sun, B. You, D. Wu, J. Du, W. Zhang, A. Hu, Y. Yang, D. M. Tang, B. S. Zhang, and H. F. Ding, "Spin Hall angle quantification from spin pumping and microwave photoresistance", Phys. Rev. B, **85**, 214423 (2012).
30. L. Liu, T. Moriyama, D. C. Ralph, and R. A. Buhrman, "Spin-torque ferromagnetic resonance induced by the spin Hall effect", Phys. Rev. Lett. **106**, 036601 (2011).
31. L. Liu, C. Pai, Y. Li, H. W. Tseng, D. C. Ralph, R. A. Buhrman, "Spin-torque switching with the giant spin Hall effect of Tantalum", Science **336**, 555 (2012).
32. C. Pai, L. Liu, Y. Li, H. W. Tseng, D. C. Ralph, R. A. Buhrman, "Spin transfer torque devices utilizing the giant spin Hall effect of tungsten", Appl. Phys. Lett. **101**, 122404 (2012).
33. A. R. Mellnik, J. S. Lee, A. Richardella, J. L. Grab, P. J. Mintun, M. H. Fischer, A. Vaezi, A. Manchon, E. –A. Kim, N. Samarth and D. C. Ralph, "Spin-transfer torque generated by a topological insulator", Nature, **511**, 449 (2014).
34. G. Mihajlovic, J. E. Pearson, M. A. Garcia, S. D. Bader, and A. Hoffmann, "Negative nonlocal resistance in mesoscopic gold Hall bars: absence of the giant spin Hall effect", Phys. Rev. Lett. **103**, 166601 (2009)

Chapter 4

Spin Seebeck Effect

4.1 Introduction

In order to solve the energy crisis, we may scavenge the waste heat and convert it into electrical power with the aid of the thermoelectric (TE) effect, which studies the interplay between heat and charge. [1] We can move one step higher by exploring spin caloritronics, which represents interplay between heat, spin and charge. [2] Therefore, this direction of spintronics research holds the potential not only in heat to charge conversion, but also in utilizing heat in information storage and processing.

Spin caloritronics studies the thermal generalization of many spintronic phenomena. For example, thermal magnetoresistance is the thermal analog of the electro-magneto transport coefficient, with voltage replaced by a heat gradient. In the spin Seebeck effect magnons are driven by a heat gradient. The anomalous Nernst effect is the thermal version of the relativistic effect of anomalous Hall effect, where transverse spin current are generated by a heat gradient and the spin orbit coupling.

This chapter is focused on the spin Seebeck effect (SSE), which generates spin current in a magnet from a temperature gradient. Ironically, this effect, a centerpiece of spin caloritronics, has been shrouded in controversy. [3] In this chapter, we first introduce the conventional (charge) Seebeck effect and then proceed to discuss the spin version.

The controversies in both the experimental geometries of SSE and the theoretical models of SSE are also introduced and discussed.

4.2 Charge Seebeck Effect

The conventional (charge) Seebeck effect, which utilizes temperature gradient to generate a charge current, was discovered by T. J. Seebeck in 1821. However, Seebeck incorrectly described it as a "thermomagnetic effect". In the original experiment, a compass needle was deflected near the closed loop of two different wires with two junctions held at different temperatures. He did not recognize that there was an electric current passing through the wires that causes the compass deflection. The more appropriate term "thermoelectricity" was introduced by Oersted. It is now widely known as the charge Seebeck effect.

In the charge Seebeck effect, a temperature difference is created in a conductor, the charge carriers at the hot side possess higher energy and thus move faster than those at the cold side. The charge carriers, diffusing from the hot side to the cold side, generate a voltage that is proportional to the temperature difference and is independent on the temperature distribution, Fig.4.1. The charge Seebeck effect can be described by the relation

$$-\nabla V = S\nabla T.$$

Here, S is the Seebeck coefficient, and is often referred to as the "thermopower", an unfortunate misnomer.

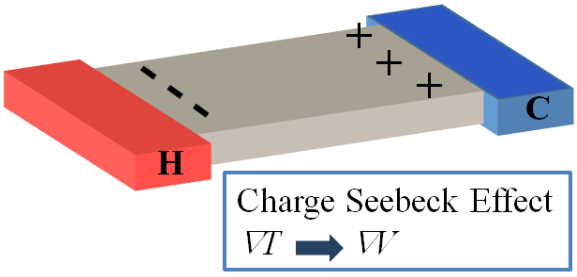

Fig.4.1 Schematic drawing of the charge Seebeck effect.

An important application of the charge Seebeck effect is the thermocouple, well known to experimentalists for measuring temperature. The standard configuration of a thermocouple consists of two different conductors with one end joint as the temperature sensor, and the other ends at a reference temperature, as shown in Fig.4.2. If the Seebeck coefficients for the two conductors (S_1 and S_2) are different, a voltage V_{12} can be measured at the separated ends of the two wires. $V_{12} = (S_1 - S_2)(T_{sense} - T_{reference})$.

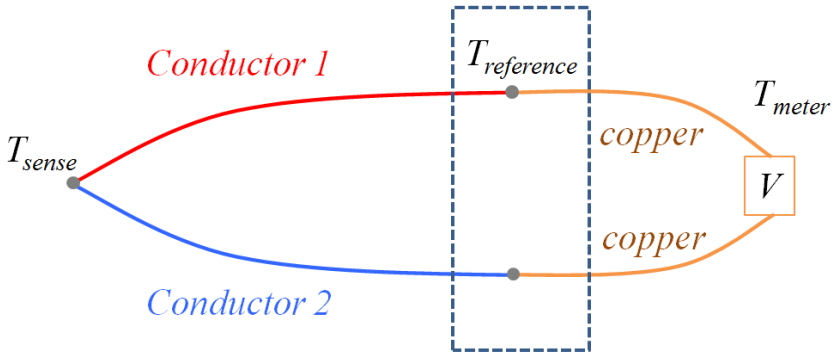

Fig.4.2 Schematic drawing of the thermocouple.

A good thermoelectric material needs not only high Seebeck coefficient and charge conductivity, but also low thermal conductivity. The dimensionless quantity that

measures the ability a material to convert heat to electric current or vice versa is the figure of merit given by

$$ZT = \frac{\sigma S^2 T}{\kappa}$$

where σ is the charge conductivity, S is the Seebeck coefficient, T is the temperature, and κ is the thermal conductivity. Materials with high ZT are notoriously difficult to realize. They include Bi_2Te_3 and Bi_2Se_3 with ZT between 0.8 and 1.0 at room temperature. The material with the highest ZT=2.2 reported at 915 K is p-type PbTe endotaxially nanostructured with SrTe, which converts 15 to 20 percent of waste heat to electricity. [1]

4.3 Spin Seebeck effect

In 2008, *Uchida et al.* [3] claimed to have observed for the first time the spin Seebeck effect in permalloy (Py) thin films on a sapphire substrate. Under a temperature gradient, the two spin channels respond differently, therefore creating spin imbalances at the edges, Fig.4.3(a). This was truly a major event in 2008. In additional to the spin current generated in conductors carried by electrons, temperature gradient can also excite magnons in a ferromagnetic insulator, where spin current is carried by magnons, Fig.4.3(b). [4] The spin Seebeck effect has been studied in ferromagnetic metals such as permalloy [3], semiconductors such as GaMnAs [5], and insulators such as $Y_3Fe_5O_{12}$ [4].

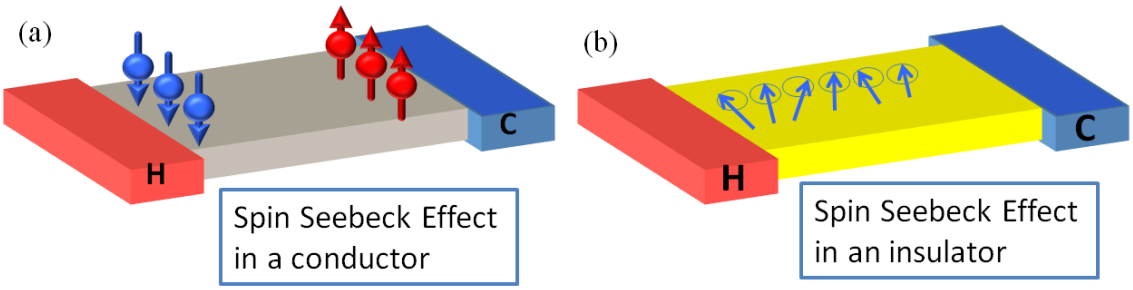

Fig. 4.3 Schematic drawing of the (a) spin Seebeck effect in a ferromagnetic conductor and (b) spin Seebeck effect in a ferromagnetic insulator.

For a thin film on a substrate, the temperature gradient may be intentionally applied parallel or perpendicular to the substrate plane, with a spin current detector located on top of thin film. The spin currents generated in the parallel and perpendicular to plane configurations are also known as the *transverse* spin Seebeck effect (TSSE) [3] and the *longitudinal* spin Seebeck effect (LSSE) [4], respectively. However, three years after the initial discovery of the *TSSE*, serious questions, first by this group, and subsequently by many others, have been raised against the 2008 claim. [6, 7] It has been firmly established that the first SSE experiment by Uchida *et al.,*[3] revealed not the SSE but rather the anomalous Nernst effect in the ferromagnetic metal. [6] In this section, the transverse and longitudinal spin Seebeck effect and the theoretical models are discussed.

4.3.1 Transverse Spin Seebeck Effect

In the transverse geometry, ideally, an in-plane temperature gradient generates an in-plane spin current in the ferromagnetic material, which diffuses vertically into a non-magnetic material with strong spin-orbit coupling and then converted to charge current by

the inverse spin Hall effect, Fig.4.4. [3, 5] The transverse spin Seebeck effect in principle exists for magnetic metals, semiconductors and insulators. However, experimentally the transverse SSE has not been reliably detected in any of these materials. [6, 7]

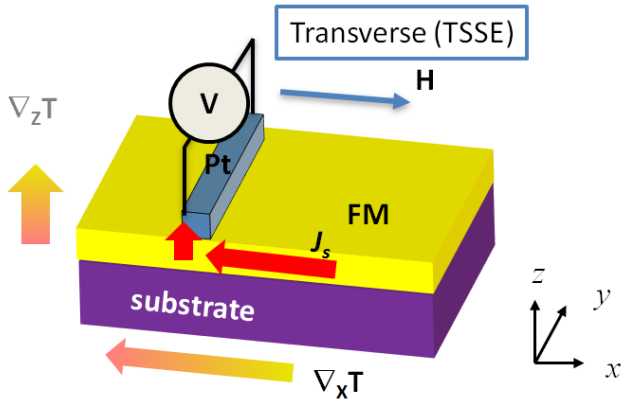

Fig.4.4 Schematic drawing of the transverse spin Seebeck effect.

The first experiment of SSE by *Uchida et al*. [3] was carried out in thin Py films on the sapphire substrate with Pt strip as spin current detector. The telltale sign of the transverse SSE is the opposite signs of the voltage in Pt strips on the hot or cold side of Py, which indicates that spins with opposite signs are injected into the Pt strips, Fig.4.5. The transverse SSE geometry implies that heat current can be used to drive spin current in a ferromagnetic metal across a millimeter length scale. However, the spin diffusion length of a ferromagnetic metal is only on the scale of nm, it is natural to ask: why can heat current drive spin current in Py over much longer distances?

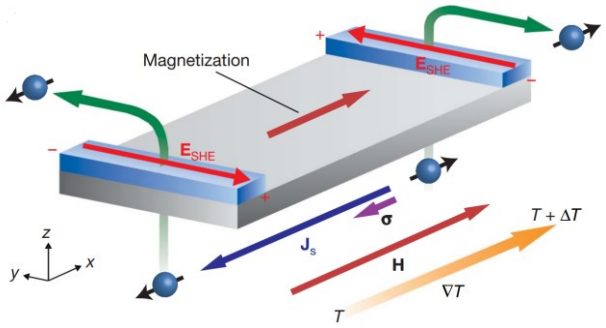

Fig.4.5 The first observation of the spin Seebeck effect in the transverse geometry. Here, ∇T is the temperature gradient, H is the magnetic field, J_s is the spin current, σ is the spin index, and E_{SHE} is the inverse spin Hall voltage in the Pt strips. Two Pt strips are located on the hot or cold side of the Py thin film. (Figure is obtained from Ref. [3])

The mystery deepens when we realize that in the diluted magnetic semiconductor GaMnAs on GaAs substrate, the GaMnAs layer was intentionally cut through, blocking the transport of any current, however the claimed SSE signal remains, Fig.4.6. [5] This result leads to the revision of SSE theory. Instead of the two spin channels mentioned above, the spin current in the new model is transported through the coupling between phonons and magnons in the substrate and in the ferromagnetic sample, respectively. Although new models have been attempted to explain this result, the result itself cast serious doubt to the validity of the transverse SSE.

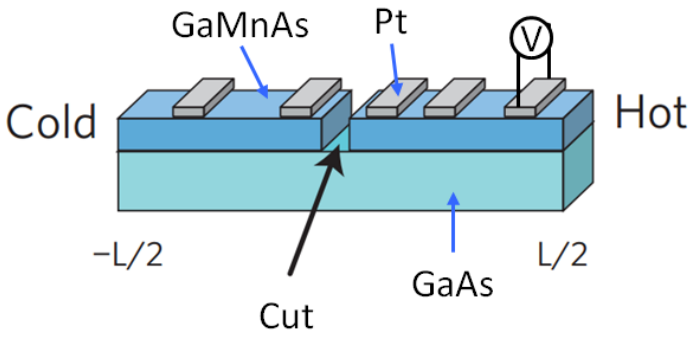

Fig.4.6 Schematic drawing of Pt strips on GaMnAs thin film, which is on top of the GaAs substrate. The thin GaMnAs film was intentionally cut through. (Figure is obtained from Ref. [5])

To resolve the mystery of the spin current transport in Py, Huang *et. al.* from this lab studied the intrinsic spin dependent thermal transport in a Py thin film on a Si substrate *without* the Pt spin current detector, as shown in Fig.4.7. [6] Surprisingly, with the same transverse SSE geometry as above, voltages obtained on the hot and cold sides of the Py film have opposite signs or the same sign depending on the vertical location of the heater, above or below the sample, in regardless of its horizontal location. Therefore, this voltage is *independent* of the direction of the in-plane temperature direction. In other words, the measured voltage has nothing to do with the transverse spin Seebeck effect!

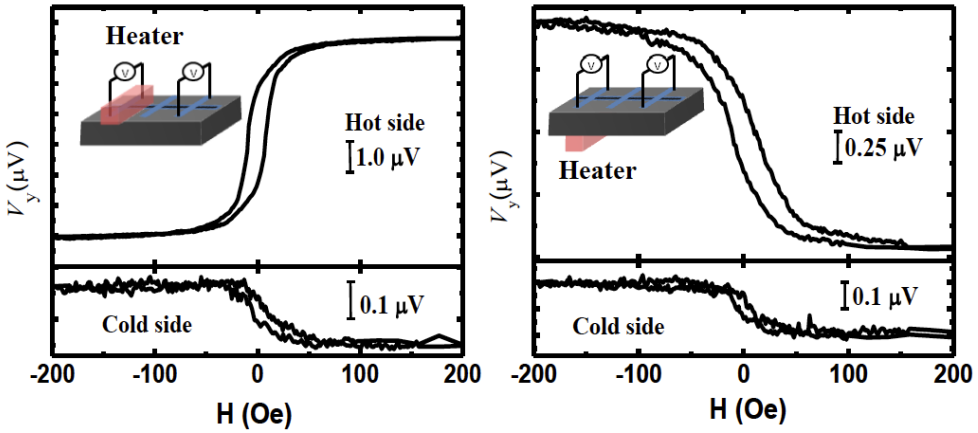

Fig.4.7 Thermal voltage obtained at the hot side and cold side of Hall bar Py on Si substrate sample with heater placed on (a) top or (b) bottom of the sample. (Figures obtained from Ref. [6])

These results show a nontrivial temperature distribution of temperature gradient in the system. In the transverse geometry, for a thin film on a thick substrate, the temperature distribution is not entirely in-plane. The substrate is ten thousand times thicker than the thin film. The thermal conductivity of Si, GaAs and Py at room temperature are 125, 56, and 30 W/m-K, respectively. When an in-plane temperature gradient is applied to a magnetic thin film on a thick substrate, a *thermal conductivity*

mismatch in the thin film, the bulk substrate and the interface unavoidably creates an out-of-plane temperature gradient which gives rise to the anomalous Nernst effect in the ferromagnetic metal. Since the anomalous Nernst effect voltage in the ferromagnet $(E_{ANE})_{FM} \propto \nabla_z T \times \hat{m}$ has the same angular dependence on the magnetic field as the inverse spin Hall effect in a non-magnetic material $(E_{ISHE})_{NM} \propto \nabla_z T \times \hat{\sigma}$, these experiments cannot conclusively establish the existence of the transverse spin Seebeck effect.

To capture the intrinsic thermal spin dependent transport in ferromagnetic metal, *substrate-free* samples or near substrate-free samples are required. *Huang et al.,*[6] used a free-standing Py foil, applied a transverse temperature gradient and observed only field-symmetric signal without any indication of the transverse SSE. *Avery et al.,* [7] used microfacbrication for thin Py film on top of a thin suspended Si-N thermal isolation bridge, with Pt strip as spin detector, as shown in Fig. 4.8. Since the thermal conductivity of Si-N is very low, it can be taken as a nearly substrate-free sample with a temperature gradient applied in-plane with negligible out-of-plane component. The results show that, with the heat current flow purely in-plane, instead of the transverse spin Seebeck voltage with $sin\theta$ field angular dependence, only the planar Nernst voltage with the $sin2\theta$ field angular dependence is observed in the Pt/Py junction. The planar Nernst voltage comes entirely from the ferromagnetic metal Py. It appears that unless one day one could do ultra sensitive measurements on the nm scale, one would not observe the transverse spin Seebeck effect any time soon.

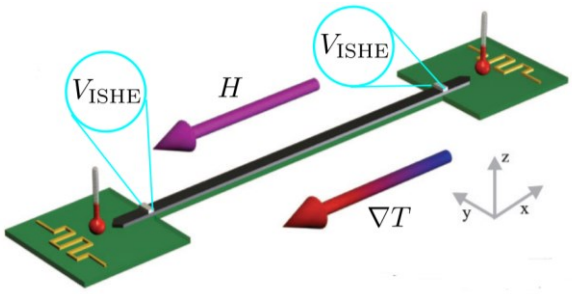

Fig.4.8 Schematic drawing of the nearly substrate free Py/Si-N bridge sample with Pt strip as spin current detector. [Figure is obtained from Ref. [7]]

4.3.2 Longitudinal Spin Seebeck Effect

The spin Seebeck effect in the transverse geometry suffers from the unintended and unavoidable out-of-plane temperature gradient in a thin film on a thick substrate. In order to capture the intrinsic SSE, one may resort to the longitudinal geometry, which entails a thin spin-current detecting layer (e.g. Pt) on a ferromagnetic insulator (e.g. YIG). In the longitudinal geometry, a vertical temperature gradient in the ferromagnetic insulator generates a spin current carried by magnons in the same direction; the spin current is then injected into the spin current detector, where it is revealed through the inverse spin Hall effect. [4] However, the longitudinal spin Seebeck effect is feasible only for ferromagnetic insulators. In a ferromagnetic conductor, there are potential complications because of the anomalous Nernst effect. The temperature gradient is well defined, allowing one to avoid the pitfalls of the transverse geometry.

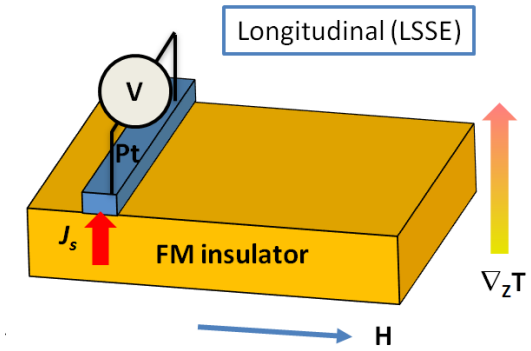

Fig.4.9 Schematic drawing of the longitudinal spin Seebeck effect.

However, the longitudinal SSE suffers from another complication, the magnetic proximity effect in Pt/YIG structure. [8] It has been shown that in the vicinity of a ferromagnetic material, sizable magnetic moment may be acquired at the interface of Pt. Therefore, the SSE signal may again be contaminated by the anomalous Nernst effect just like in the transverse geometry. In order to observe the intrinsic SSE, a non-magnetic metal with strong spin orbit coupling and without the complication of magnetic proximity is required. [9] Details of the magnetic proximity effect and the detection of intrinsic spin Seebeck effect are discussed in the Chapters 5 and 6.

4.4 Magnon Spin Current Model

Aside from the controversy about the transverse spin Seebeck effect, another unresolved issue is the mechanism of spin current generation in the longitudinal SSE. Theoretical models include the phonon-magnon drag [10, 11] and the bulk magnon descriptions [12], attributing the origin to the effective magnon temperature difference at the metal/FM interface and the bulk magnon transport, respectively. The phonon-magnon drag model was intended for the transverse spin Seebeck effect, with dubious validity. The bulk

magnon spin current model explains quantitatively the longitudinal spin Seebeck effect, so we briefly describe it.

This model [12] considers a ferromagnetic insulating (FMI) layer in contact with a non-magnetic metal (NM) layer. Denoting the magnons with wave vector $\vec{k}$, wave number n_k and energy $\hbar\omega_k$, the Bose-Einstein distribution gives the number in the thermal equilibrium $n_k^0 = \frac{1}{e^{\hbar\omega_k/k_BT}-1}$. The number of magnon excesses the equilibrium is $\delta n_k = n_k - n_k^0$. Therefore, the total magnon accumulation in excess of equilibrium is

$$\delta n_m = \frac{1}{(2\pi)^3}\int d^3k(n_k - n_k^0).$$

The spin current flows along the z direction can be written as

$$\vec{J}_S^z = \frac{\hbar}{(2\pi)^3}\int d^3k\vec{v}_k(n_k - n_k^0).$$

In the relaxation approximation, $n_k - n_k^0 = -\tau_k\vec{v}_k \cdot \nabla n_k(\vec{r})$, where τ_k is the *k*-magnon relaxation time. The spin current is the sum of two parts, the contributions from the flow of magnons due to temperature gradient and spatial variation of the magnon accumulation

$$\vec{J}_S^z = \vec{J}_{S\nabla T}^z + \vec{J}_{S\delta n}^z = -\frac{\hbar}{(2\pi)^3}\int d^3k\tau_k\vec{v}_k[\frac{\partial n_k^0}{\partial T}(\vec{v}_k \cdot \nabla T) + (\vec{v}_k \cdot \nabla\delta n_k(\vec{r}))].$$

When the magnetic moment in the FMI layer starts precessing, a spin current is pumped into the adjacent NM layer at the interface at the rate

$$\vec{J}_S^z(0) = \frac{\hbar g_r^{\uparrow\downarrow}}{4\pi M^2}(\vec{M} \times \frac{\partial\vec{M}}{\partial t})$$

where $g_r^{\uparrow\downarrow}$ is the spin mixing conductance. Consider all these equations with the magnon dispersion relation $\omega_k = \gamma H + \omega_{ZB}(1 - cos\frac{\pi k}{2k_m})$, ω_{ZB} is the zone boundary frequency, boundary conditions where $\vec{J}_S^z(t_{FM}) = 0, \vec{J}_S^z(0^+) = \vec{J}_S^z(0^-)$ and with some approximations, one obtain the spin current density at the FMI/NM interface

$$\vec{J}_S^z(0) = C\nabla T$$

where $C = -\frac{\gamma\hbar\rho' k_m^3 l_m}{4\pi M\pi^2}\frac{B_1 B_S}{B_2} g_{eff}^{\uparrow\downarrow} k_B$, $\rho' = \frac{cosh(t_{FM}/l_m)-1}{sinh(t_{FM}/l_m)}$, t_{FM} is the thickness of the FMI layer. When $t_{FM} \gg l_m$, $\rho' \to 1$. $\gamma = g\mu_B/\hbar = 1.76 \times 10^{11} s^{-1}T^{-1}$ is the gyromagnetic ratio. g is the spectroscopic splitting factor. $\hbar = 1.054 \times 10^{-34} J \cdot s$ is the reduced Plank constant. $k_m = 2 \times 10^9 m^{-1}$ is the maximum wave number assuming a spherical Brillouin zone. $4\pi M = 1.76kG$ is the YIG magnetization. $k_B = 1.38 \times 10^{-23} JK^{-1}$ is the Boltzmann constant. $l_m = 70nm$ is the magnon diffusion length for thin YIG film. $g_{eff}^{\uparrow\downarrow} = 6.9 \times 10^{18} m^{-2}$ is the spin mixing conductance at the Pt/YIG interface. $B_1 = 0.55$, $B_s = 2.2 \times 10^{-4}$ and $B_2 = 5.1 \times 10^{-3}$ are the parameters in the diffusion equation. From this model, the spin current injected into Pt, generated from YIG under a temperature gradient $\nabla T = 20K \cdot mm^{-1}$ is

$$J_S^z(0) = 4.05 \times 10^{-11} Jm^{-2}.$$

This model [12] agrees well with the experimental data from the longitudinal spin Seebeck effect in a ferromagnetic insulator and a metal bilayer structures. In Chapter 7, we describe a similar model inspired by the experimental approach to calculate the spin Hall angle and spin diffusion length of various materials from the thermal spin injection.

Reference to Chapter 4

1. G. J. Snyder and E. S. Toberer, “Complex thermoelectric materials”, Nat. Mater. **7**, 105 (2008)
2. G. E. W. Bauer, E. Saitoh and B. J. van Wees, “Spin caloritronics”, Nat. Mater. **11**, 391 (2012)
3. K. Uchida, S. Takahashi, K. Harii, J. Ieda, W. Koshibae, K. Ando, S. Maekawa, and E. Saitoh, “Observation of the spin Seebeck effect”, Nature, **455**, 778 (2008)
4. K. Uchida, H. Adachi, T. Ota, H. Nakayama, S. Maekawa and E. Saitoh, “Observation of longitudinal spin-Seebeck effect in magnetic insulators”, Appl. Phys. Lett. **97**, 172505 (2010)
5. C. M. Jaworski, J. Yang, S. Mack, D. D. Awschalom, J. P. Heremans and R. C. Myers, “Observation of the spin-Seebeck effect in a ferromagnetic semiconductor”, Nat. Mater. **9**, 898 (2010)
6. S. Y. Huang, W. G. Wang, S. F. Lee, J. Kwo, and C. L. Chien, “Intrinsic spin-dependent thermal transport”, Phys. Rev. Lett. **107**, 216604 (2011)
7. A. D. Avery, M. R. Pufall, and B. L. Zink, “Observation of the planar Nernst effect in permalloy and nickel thin films with in-plane thermal gradients”, Phys. Rev. Lett. **109**, 196602 (2012)
8. S. Y. Huang, X. Fan, D. Qu, Y. P. Chen, W. G. Wang, J. Wu, T. Y. Chen, J. Q. Xiao, and C. L. Chien, “Transport magnetic proximity effect in platinum”, Phys. Rev. Lett. **109**, 107204 (2012)

9. D. Qu, S. Y. Huang, Jun Hu, Ruqian Wu, and C. L. Chien, “Intrinsic spin Seebeck effect in Au/YIG”, Phys. Rev. Lett. **110**, 067206 (2013)
10. H. Adachi, K. Uchida, E. Saitoh, and S. Maekawa, “Theory of the spin Seebeck effect”, Rep. Prog. Phys. **76**, 036501 (2013)
11. J. Xiao, G. E. W. Bauer, K. Uchida, E. Saitoh, and S. Maekawa, “Theory of magnon-driven spin Seebeck effect”, Phys. Rev. B **81**, 214418 (2010)
12. S. M. Rezende, R. L. Rodriguez-Suarez, R. O. Cunha, A. R. Rodrigues, F. L. A. Machado, G. A. Fonseca Guerra, J. C. Lopez Ortiz, and A. Azevedo, “Magnon spin-current theory for the longitudinal spin-Seebeck effect”, Phys. Rev. B **89**, 014416 (2014)

Chapter 5

New Type of Magnetoresistance and Hall Resistance at the Pt/YIG Interface and Controversies

5.1 Magnetic Proximity Effect

Platinum (Pt) thin film on a ferromagnet has been used in establishing most of the pure spin current phenomena because of its large spin-orbit coupling. Given the prominent role of Pt in spin-based phenomena, it is important to determine the transport and magnetic property of thin Pt film on a ferromagnet. One notes that only materials passing the Stoner Criterion, $J\,D(E_F) > 1$, where J is the exchange integral and $D(E_F)$ is the density of states at Fermi energy, become ferromagnets. When Pt is in close proximity to a ferromagnet, because of its large density in *d* electrons, it almost satisfies the Stoner criterion, resulting in the polarization of the Pt/FM interface spins.

Unfortunately, when a thin Pt film is in contact with a FM metal, its magnetic transport properties are strongly modified by the FM metal. This problem may be alleviated by replacing an FM metal with an FM insulator. In the electric transport study of a Pt thin film on the ferromagnetic insulator yttrium iron garnet (YIG), we have observed strong magnetic proximity effect (MPE) in Pt films. [1] These FM characteristics in Pt question the suitability of using Pt to study pure spin current phenomena.

Because Pt is a non-magnetic metal, a Pt thin film has only ordinary magnetoresistance (negligible at low magnetic field) and ordinary Hall resistance (linear dependence with magnetic field). This has been confirmed with the magnetoresistance (MR) measurement, which is performed in a Hall-bar-patterned thin film deposited on a substrate. The MRs are denoted as $\rho_{||}$ and ρ_T, when the field is applied parallel (x-axis) or transverse (y-axis) to the current direction, respectively. And the MR ratio is defined as $(\rho_{||}-\rho_T)/\rho_{||}$. For 10-nm thick thin Pt films on a Si substrate and 10-nm Cu thin films on a YIG substrate, negligible MR ratios are observed, as shown in Fig.5.1(b). However, surprisingly, when Pt is adjacent to a ferromagnetic insulator YIG layer, a pronounced difference in $\rho_{||}$ and ρ_T is observed. The behavior of the MR in Pt/YIG is related to the magnetization of YIG as shown in Fig.5.1(c), where M_x an M_y are magnetization of the rectangular YIG along the length (x) and width (y) axes. In both $\rho_{||}$ and ρ_T, the resistivity near the zero magnetic field is roughly at $(\rho_{||}+\rho_T)/2$ due to the remnant state of the polycrystalline YIG with a near zero magnetization from magnetic grains of random orientations. These results strongly suggest the MPE in Pt in on an FM insulator.

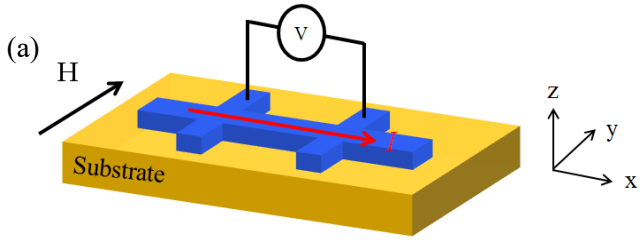

Fig.5.1 (a) Schematic drawing of the magnetoresistance measurement.

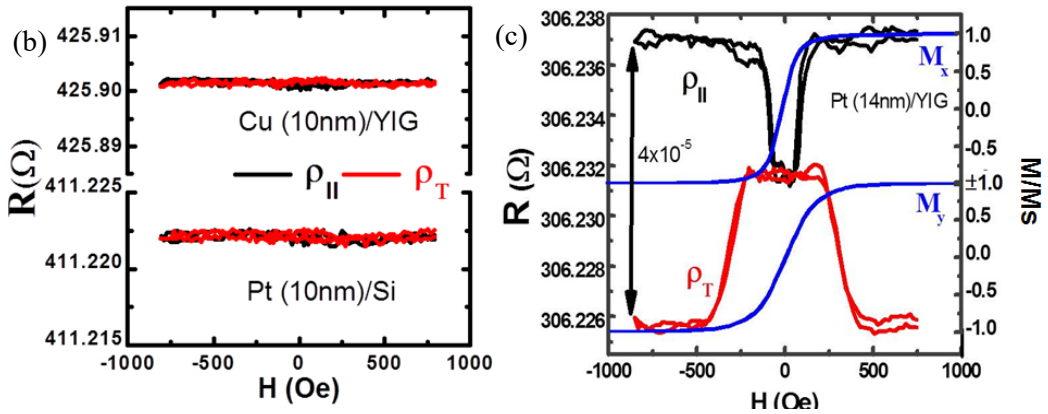

Fig. 5.1(continue) (b)The magnetoresistance of Cu(10 nm)/YIG and Pt(10 nm)/Si. (b) The magnetoresistance and magnetization of Pt(14 nm)/YIG. Black line is the longitudinal resistance, red line is the transverse resistance and the blue line is the magnetization.

Another key feature is the anomalous Hall effect. The Hall measurement setup is shown in Fig 5.2 (a). An electrical current and a magnetic field are applied along the *x* and *z* axes, respectively. A Hall voltage is read along the *y*-axis. The Hall resistance ($R_H=V_{xy}/I$) of the 10-nm Cu/YIG and 15-nm Pt/Si show only the ordinary Hall effect with the Hall voltage linearly dependent on *H* and independent of temperature, as shown in Fig.5.2(a). These are the expected features of a nonmagnetic metal. In contrast, completely different Hall resistances have been observed in 10-nm Pt/YIG sample, as shown in Fig.5.2(b). The anomalous Hall resistance R_{AHE} increases sharply with decreasing temperature and even changes the sign. Drastically different Hall responses for Pt/Si and Pt/YIG again strongly suggest the magnetic proximity effect in Pt/YIG.

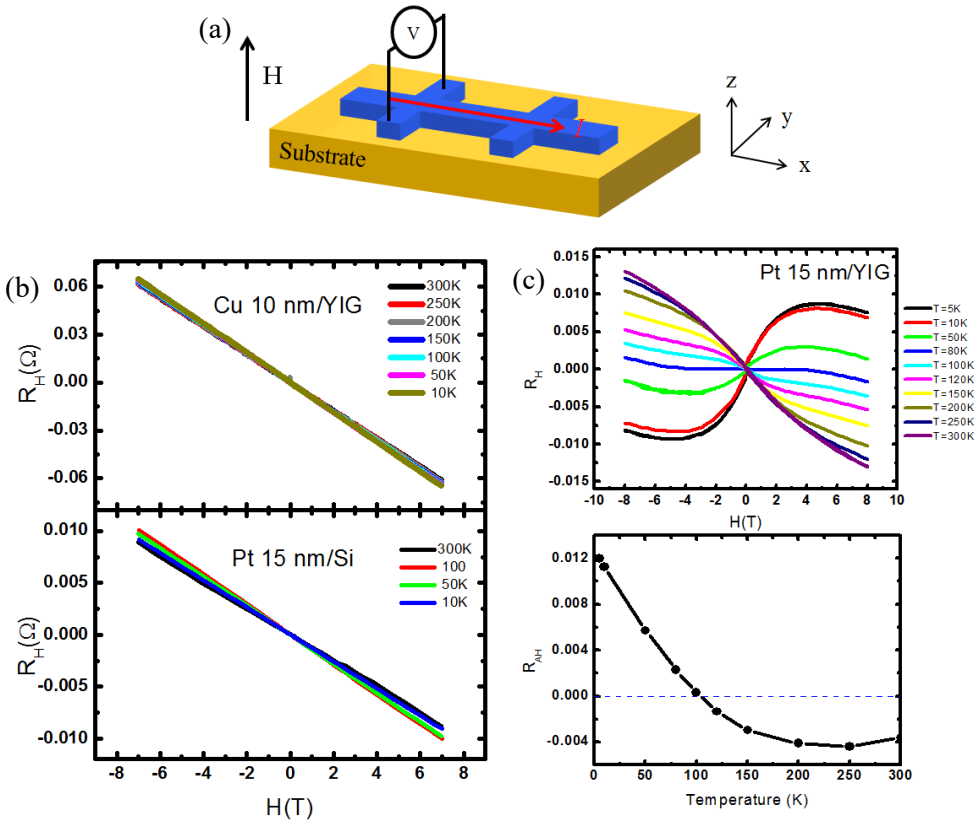

Fig. 5.2 (a) Schematic drawing of the Hall measurement. (b) Hall resistance of Cu (10 nm)/YIG and Pt (15 nm)/Si under various temperatures from 10 K to 300 K. (c) Hall and anomalous Hall resistance of Pt (15 nm)/YIG under various temperatures from 5 K to 300 K.

It should be noted that there is a sharp difference between the magnetic proximity MR and the anisotropic MR (AMR) in a common FM metal. AMR is a bulk property of an FM layer, thus when the FM metal layer becomes thinner, the AMR ratio in a FM decreases because of the finite size effect. In contrast, for Pt /YIG, the MR ratio increases when the Pt film thickness decreases, indicating that this effect has an interfacial origin, see Fig. 5.3. For thin films with thickness less than 2 nm, the MR ratio of Pt/YIG decreases because of enhanced surface scattering. Therefore, the resistivity increases sharply as the thickness decreases, resulting in a decrease in MR ratio. The MR in Pt/YIG

is clearly not the common AMR in an FM metal. We show their differences in the next sections.

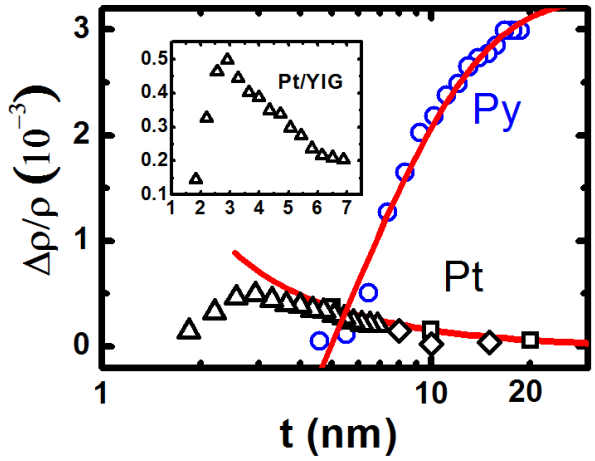

Fig.5.3 Thickness dependent MR ratio for Pt(t)/YIG (black dots) and Py(t)/YIG (blue dots). Inset is the zoom in for Pt/YIG samples.

5.2 Magnetic Proximity Magnetoresistance

5.2.1 Magnetoresistance in Pt/YIG

With only an *in-plane* magnetic field, the MR in Pt/YIG resembles the anisotropic MR (AMR) as in a common FM metal, where $\rho_{||} > \rho_T$. In fact, the novelty of the MR in the Pt/YIG heterostructure lies in the *out-of-plane* MR ($\rho_\perp$), where the magnetic field is applied along the z-axis. [2]

Out-of-Plane MR in a Common FM Metal

The AMR in the FM conductors is caused by the spin-orbit coupling and *d* band splitting. [3] In a ferromagnet, the resistance is larger when magnetic field is parallel with current and smaller when magnetic field is perpendicular to current.

$$\textbf{AMR: } \rho_{||} > \rho_T \approx \rho_{\perp} \quad \textbf{(1)}$$

Here, ρ_T and $\rho_{\perp}$ are transverse and perpendicular MR where magnetic field is applied along the *y* (in-plane) and *z* (out-of-plane) axes, respectively. To verify Eq. (1), one can use the experimental geometry illustrated in Fig 5.4, with the current and voltage applied and measured along the x axis. The magnetic field scans in the xy, xz and yz planes, with field to current angle ϕ, α and θ, respectively.

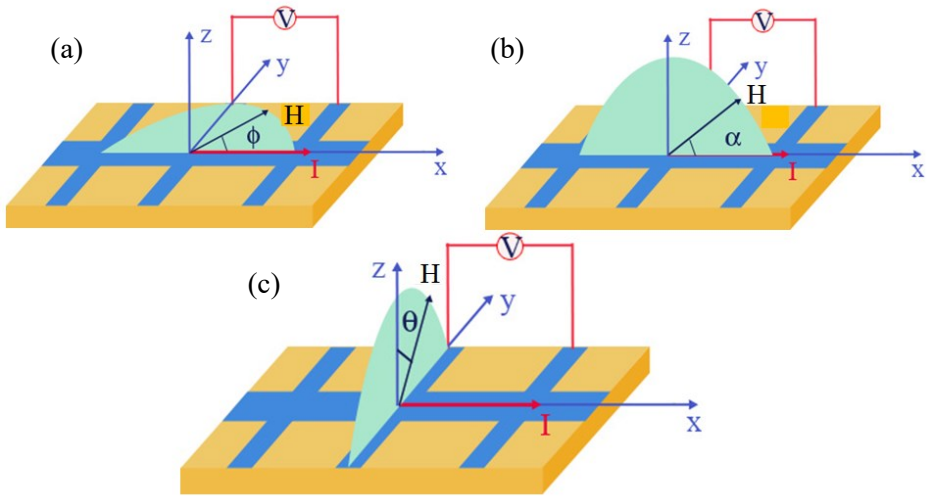

Fig.5.4 Schematic drawing of the magnetic field angular dependent measurement in the (a) xy plane, (b) xz plane and (c) yz plane.

The representative AMR results in Py using the ϕ_{xy}, α_{xz}, and θ_{yz} field scan are shown in black, red, and blue in Fig.5.5 respectively. With an inplane magnetic field, the

ϕ_{xy} scan shows the $cos^2\phi_{xy}$ dependence, and $\rho_{||} > \rho_T$. With a large magnetic field (40 kOe) the out of plane scan α_{xz} also shows a $cos^2\alpha_{xz}$ angular dependence and $\rho_{||} > \rho_\perp$. For FM films with in-plane anisotropy, the θ_{yz} scan is almost a constant value, thus $\rho_T \approx \rho_\perp$. The slight variation in the θ_{yz} scan is caused by the geometrical size effect. [4]

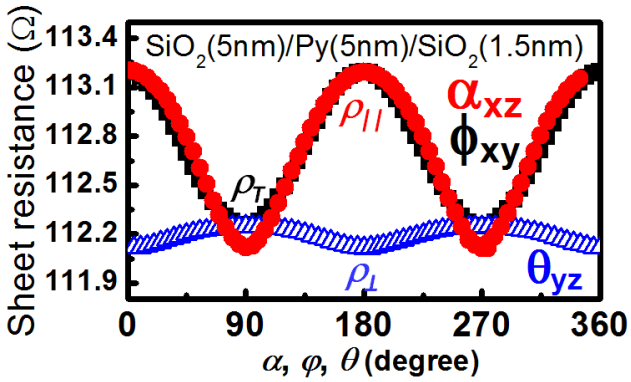

Fig.5.5 Magnetic field angular dependent magnetoresistance for SiO_2(5 nm)/Py(5 nm)/SiO_2(1.5 nm) sample. Magnetic field scans in the xz, xy, and yz planes are represented by red, black and blue curves, respectively.

Out-of-Plane MR in Pt/YIG Structure

For Pt thin film on Si, no measurable MR appears as expected. In contrast, Pt thin film on YIG shows pronounced unusual MR, as shown in Fig.5.6. It first appears similar to the AMR in the inplane ϕ_{xy} scan, where $\rho_{||} > \rho_T$ and follows the $cos^2\phi_{xy}$ angular dependence. However, the out of plane α_{xz} and θ_{yz} scan are very different from the conventional AMR feature, where θ_{yz} scan shows a $cos^2\theta_{yz}$ angular dependence while α_{xz} scan shows no variation. This means $\rho_\perp \neq \rho_T$, and instead $\rho_\perp \approx \rho_{||}$. Therefore,

Magnetic Proximity MR: $\rho_\perp \approx \rho_{||} > \rho_T$ (2)

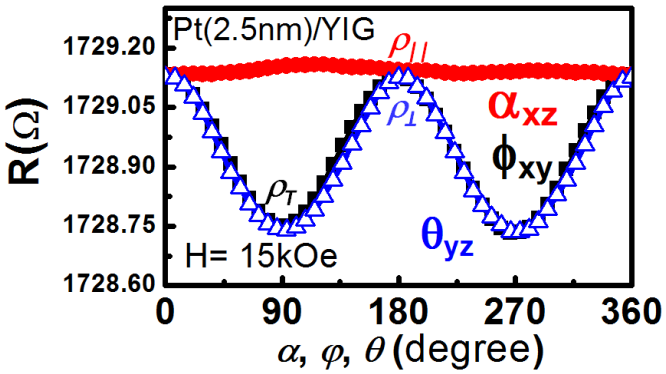

Fig.5.6 Magnetic field angular dependent magnetoresistance for Pt(2.5 nm)/YIG sample under a magnetic field of 1.5 T. Magnetic field scans in the xz, xy, and yz planes are represented by red, black and blue curves, respectively.

For the new MR, the question is what causes the perpendicular MR ($\rho_{\perp}$) to be different from the transverse MR (ρ_T) and to be the same as the parallel MR ($\rho_{||}$). To understand the physics behind the new MR, we designed different heterostructures, such as Pt/FM metal, Pt/bombarded YIG, and Pt/SiO(dopped Fe), for the MR measurement.

5.2.2 Magnetoresistance in Pt/Py/Pt

The MPE has also been reported and confirmed by x-ray magnetic circular dichroism (XMCD) in Pt in contact with FM metals, including Pt/Co, Pt/Ni, and Pt/Fe. Since Pt on ferromagnetic insulator YIG shows the new MR, one would also want to verify whether Pt on ferromagnetic metal shows the same new MR behavior. We have measured a series of samples of Pt(3 nm)/Py(t_{py})/Pt(1.5 nm) for which the MR results in the ϕ_{xy}, α_{xz}, and θ_{yz} scan can be well described by $\cos^2$ function as shown in Fig.5.7. The results also show that $\boldsymbol{\rho_{||} > \rho_{\perp} > \rho_T}$, which is the combination of the AMR in FM and magnetic proximity MR at the Pt/FM interface.

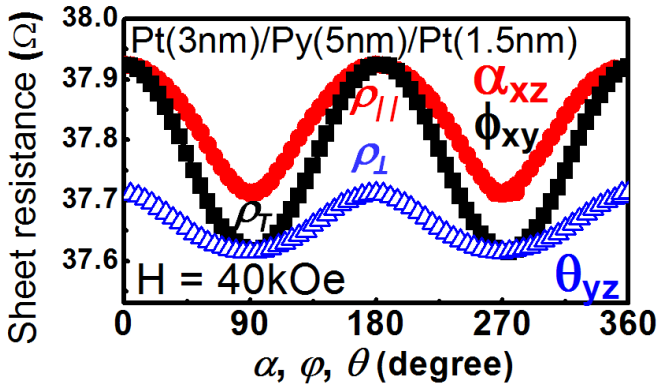

Fig.5.7 Magnetic field angular dependent magnetoresistance for Pt(3 nm)/Py(5 nm)/Pt(1.5 nm) sample under a magnetic field of 4 T. Magnetic field scans in the xz, xy, and yz planes are represented by red, black and blue curves, respectively.

The thickness dependent MR for each scan for Pt/Py (t)/Pt shows that when the Py thickness decreases, the AMR component decreases, and the new MR component increases, reflecting the bulk and interfacial nature for the two MR effects in this hybrid heterostructures. The strong correlation between the new MR and the magnetic proximity effect strongly suggests the new MR is a result of the MPE of Pt in contact with a ferromagnet. Therefore we denote this MR as magnetic proximity MR (MPMR).

5.3 Controversies on the New Magnetoresistance

5.3.1 Spin Hall Magnetoresistance

The MPMR has controversies, and one of the main controversies stems from an argument by *Nakayama, et al*. [5] about spin Hall magnetoresistance (SMR) in Pt/YIG heterostructure. In the SMR model, shown in Fig. 5.8, Pt remains nonmagnetic. When a current flows in Pt, a transverse spin current generated by the spin Hall effect diffuses

towards the Pt/YIG interface. When the magnetization of YIG is parallel with the spins (transverse to the electrical current direction), the spins are reflected back to Pt layer, and converted back to charge current through the inverse spin Hall effect, thus reducing the resistance. On the other hand, when the magnetization direction is perpendicular to the spin direction (and either parallel or perpendicular to the electrical current direction), the spins get absorbed by the YIG layer, thus increasing the resistance. Therefore, ρ_T has the smallest value, and $\rho_{||}$ and $\rho_{\perp}$ have similar and large values.

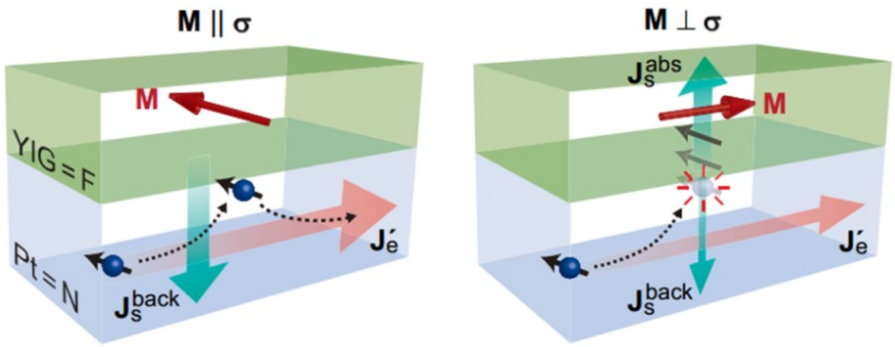

Fig. 5.8 Schematic drawing of the spin Hall magnetoresistance. (Figure is obtained from Ref.[5])

The theoretical calculation for the SMR ratio is

$$\frac{\Delta\rho_{xx}}{\rho_0} \approx \theta_{SH}^2 \frac{\frac{2\lambda^2}{\sigma_N d_N} G_r tanh^2 \frac{d_N}{2\lambda}}{1+\frac{2\lambda}{\sigma_N} G_r coth \frac{d_N}{\lambda}}.$$

Where $\Delta\rho_{xx}$ is the change of the resistivity, $\rho_0$is the resistivity, θ_{SH} is the spin Hall angle, λ is the spin diffusion length, σ_N is the conductivity of Pt, d_N is the thickness of the Pt layer, G_r is the spin mixing conductance between the Pt layer and YIG. Therefore, in the SMR model, the MR ratio is proportional to the spin Hall angle, the interface spin mixing conductance and some other quantities. The SMR model thus uses the spin current

conversion and absorption to explain the new MR observed in the Pt/YIG system. However, there are some drawbacks in the SMR model as we discuss next.

5.3.2 Magnetoresistance in Surface Treated Samples

In order to determine whether the new MR behavior originates from the magnetic proximity effect or from spin current conversions, we modified the interfaces between Pt/YIG by using Ar^+ bombardment. We also prepared another sample using 7% Fe dopped SiO_2 as a substrate that does not transmit spin current but has an artificially introduced MPE. [6]

The YIG sample was purposely altered by Ar ion beam bombardment (500 V, 0.4mA/cm^2) for 5 mins, which changes the surface termination of the YIG substrate. The change of the YIG surface termination greatly alters the spin-mixing conductance of Pt/YIG, which to a large extent determines the transmission efficiency for spin current between two different materials. As shown in Fig.5.9, after the bombardment, the spin current generated in bulk YIG cannot pass through the Pt/YIG interface. Similarly, since no spin current is generated in the SiO_2(7% Fe) sample, no inverse spin Hall effect is observed in the Pt/SiO_2 (7% Fe) sample. Therefore we would expect no SMR behavior in these heterostructures.

We performed the same field angular dependent scans for these samples. Although no spin current passes through the interfaces, we still observed the new MR behaviors in all the samples with $\rho_{||} > \rho_T$, $\rho_{||} \approx \rho_{\perp}$ as we have seen in the Pt/YIG samples as shown in the right column of Fig.5.10.

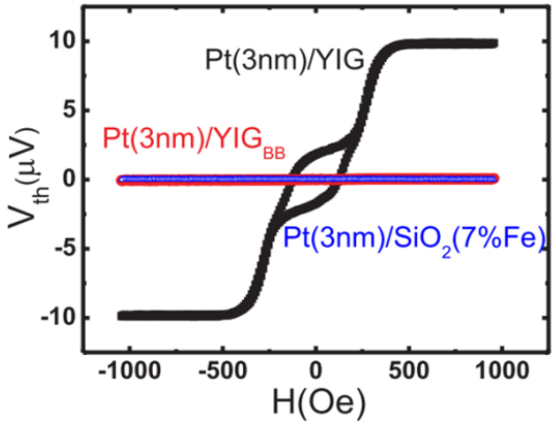

Fig.5.9 Inverse spin Hall voltage in the Pt layer due to thermal spin injection from untreated YIG (black), bombardment treated YIG (red), and the 7% Fe dopped SiO_2.

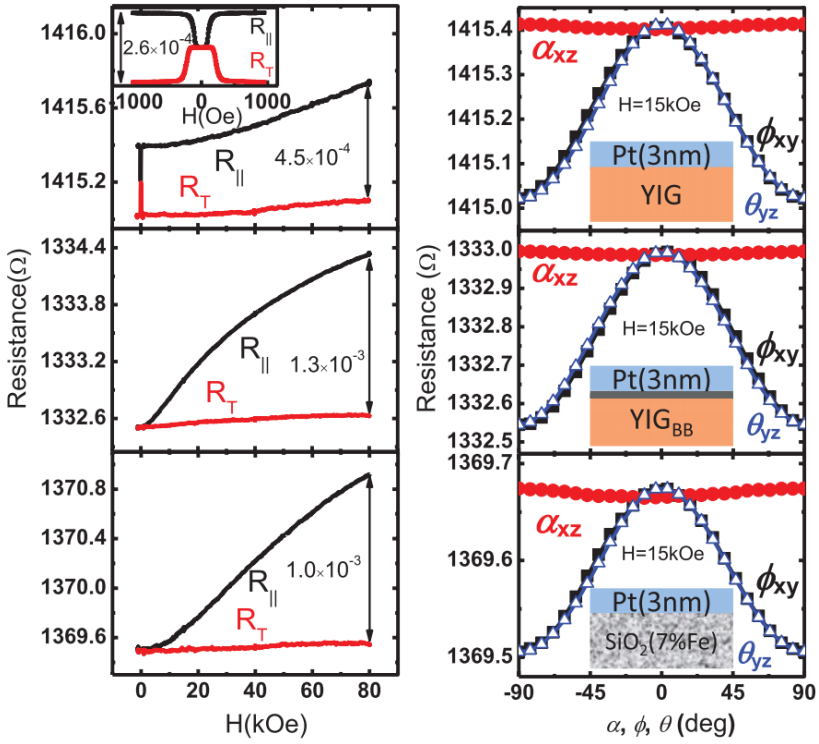

Fig.5.10 (Left panel) Magnetoresistance in the parallel (black) and transverse (red) direction for Pt(3 nm)/YIG, Pt(3 nm)/YIG_{BB}, and Pt (3nm)/SiO_2(7% Fe) samples. (Right pane) The corresponding angular dependence for these samples.

The left panel of Fig.5.10 describes the MR dependence on the magnetic field. A clear difference between the Pt/YIG sample and the surface treated samples are the MR at

small magnetic field (< 1kOe). No measureable MR can be observed for the Pt/YIG_{BB} samples or the Pt/SiO_2 (Fe dopped) samples at low field where the spin current has been blocked.

The results indicate that there are two contributions to the MR in the Pt/YIG structure. The small field MR correlates with the spin current transmission across the Pt/YIG interfaces that appear or disappear with the interface qualities. And the high field MR with the unique angular dependence is related to the MPE at the Pt/FM interfaces.

Reference to Chapter 5

1. S. Y. Huang, X. Fan, D. Qu, Y. P. Chen, W. G. Wang, J. Wu, T. Y. Chen, J. Q. Xiao, and C. L. Chien, "Transport magnetic proximity effect in platinum", Phys. Rev. Lett. **109**, 107204 (2012)
2. Y. M. Lu, J. W. Cai, S. Y. Huang, D. Qu, B. F. Miao, and C. L. Chien, "Hybrid magnetoresistance in the proximity of a ferromagnet", Phys. Rev. B **87**, 220409(R) (2013)
3. T. R. McGuire and R. I. Potter, "Anisotropic magnetoresistance in ferromagnetic 3d alloys", IEEE Trans. Mag. **11**, 1018 (1975)
4. A. Kobs, S. Hesse, W. Kreuzpaintner, G. Winkler, D. Lott, P. Weinberger, A. Schreyer, H. P. Oepen, "Anisotropic interface magnetoresistance in Pt/Co/Pt sandwiches", Phys. Rev. Lett. **106**, 217207 (2011)
5. H. Nakayama, M. Althammer, Y.-T. Chen, K. Uchida, Y. Kajiwara, D. Kikuchi, T. Ohtani, S. Geprags, M. Opel, S. Takahashi, R. Gross, G. E. W. Bauer, S. T. B. Goennenwein, and E. Saitoh, "Spin Hall magnetoresistance induced by a nonequilibrium proximity effect", Phys. Rev. Lett. **110**, 206601 (2013)
6. B. F. Miao, S. Y. Huang, D. Qu, and C. L. Chien, "Physical origins of the new magnetoresistance in Pt/YIG", Phys. Rev. Lett. **112**, 236601 (2014)

Chapter 6

Intrinsic Spin Seebeck Effect in Ferromagnetic Insulator YIG

6.1 Introduction

The spin Seebeck effect (SSE), first claimed in 2008, exploiting the interplay of spin, charge, and heat, has been reported in a variety of ferromagnetic materials including metals, semiconductors and insulators.[1 - 3] Pure spin current induced by a temperature gradient in an FMs is detected by an attached Pt strip by means of the inverse spin Hall effect. However, in 2011 members of this group demonstrated that the transverse SSE using a ferromagnetic thin film on a substrate, thanks to the overwhelming heat conduction through the substrate, suffers from an out-of-plane temperature gradient, which gives rise to the anomalous Nernst effect (ANE) in the ferromagnetic metal. [4] Since the ANE and the SSE have the same angular dependence, the two voltages are always additive, entangled and inseparable. No transverse SSE has been unequivocally observed. Many groups have subsequently made the same conclusion. These aspects have been discussed in the Chapter 4.

In the longitudinal geometry of SSE using Pt on a FM insulator YIG (Yttrium Iron Garnet), while the temperature gradient is unequivocally out-of-plane, one encounters a different issue of the magnetic proximity effect (MPE) in Pt in contact with a FM material, as has been discussed in the previous chapter. [5] As a result, in the longitudinal configuration there may also be entanglement with the MPE induced thermal

effects. These complications, when present, prevent the unequivocal establishment of the SSE in the longitudinal configuration. A convincing demonstration of the SSE has thus not been achieved. It is essential to identify a metal with large spin orbit coupling but with small enough MPE. In this chapter, we discuss the intrinsic longitudinal SSE in Au/YIG. [6]

6.2 Ferromagnetic Insulator YIG

We first describe the ferromagnetic insulator Yttrium Iron Garnet ($Y_3Fe_5O_{12}$, YIG). It has been extensively used for studies of spin waves, and the spin Seebeck effect thanks to its low magnetic damping. In this section, some physical properties of YIG, including the crystal structure and magnetic properties, are discussed.

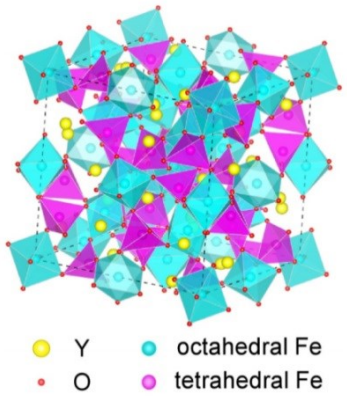

Fig. 6.1 Crystalline structure of the Yttrium Iron Garnet. (Figure is obtained from Ref. [7])

6.2.1 Crystal Structure

YIG has a cubic crystalline structure with a lattice constant of a = 12.376 Å and space group *Ia-3d* as shown in Fig.6.1. [7] The large unit cell contains 160 atoms with complex atomic arrangements. Of those 40 are Fe^{3+} ions, each carrying a magnetic moment of $5\ \mu_B$.

These Fe^{3+} ions are located differently, 16 on the octahedral and 24 on the tetrahedral sites. The magnetic moments are parallel for all the Fe^{3+} in octahedral or tetrahedral sites, but are antiparallel for the two crystalline structures, resulting in a ferrimagnetic order with a small net magnetization.

GGG (gadolinium gallium garnet) has been well established as the best substrate to fabricate epitaxial YIG films, because of the similarity in crystal structure and lattice parameters. The x-ray diffraction pattern (XRD) for the polycrystalline bulk YIG and epitaxial YIG thin film grown on GGG are shown in Fig.6.2. The lattice constant for GGG is 12.383 Å, which is very close to that of YIG. For the single crystalline (111)-oriented GGG substrate, the (444) peak is at 2θ=*51.06*°, very close to that of the YIG at *51.07*°. Therefore, it is very difficult to distinguish the peaks between YIG and GGG, as shown in Fig. (b).

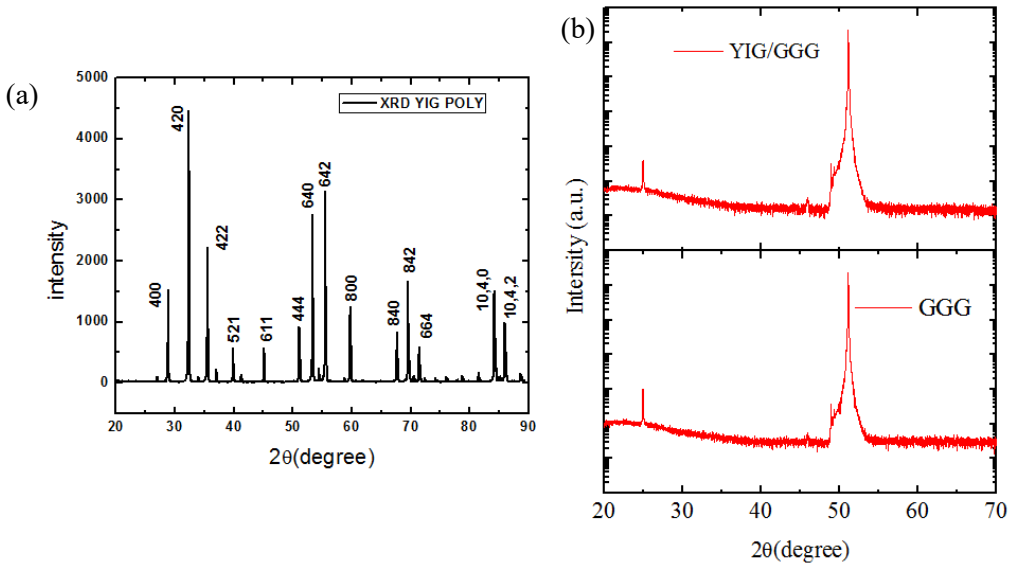

Fig. 6.2 (a) XRD for polycrystalline YIG. (b)XRD for single crystalline YIG (top) and the GGG substrate (bottom).

6.2.2 Magnetic Property

YIG is a ferrimagnetic material with a Curie temperature of 550 K and saturation magnetization $4\pi M_S$=1.7 *kG*. We have used two types of YIG samples: commercially available polycrystalline YIG substrate with a typical thickness of 0.5 mm, and an epitaxial YIG film grown on GGG substrate by this group. The polycrystalline YIG substrates and the epitaxial YIG thin films on GGG substrate are roughly rectangular in shape with dimensions 3×7×0.5 mm^3.

Magnetometry measurements show that YIG is magnetically very soft with small remnant magnetization, small coercivity, and with in-plane anisotropy, as shown in Fig. 6.3. For the polycrystalline YIG substrates, the in-plane saturation field varies from 200 Oe to 500 Oe depending on the shape, whereas the out-of-plane saturation field is 1700 Oe, reflecting its $4\pi M_S$ values. For the thin epitaxial YIG films, in-plane saturation field is smaller; from a few Oe to 10 Oe. But its saturation magnetization is only 2/3 of that of the bulk YIG. This reduction of magnetization in YIG films has been observed in many YIG thin films. Many factors may cause the reduction of the net magnetization in thin films, from changes of either the sublattice magnetization to the finite size effect in thin YIG layers.

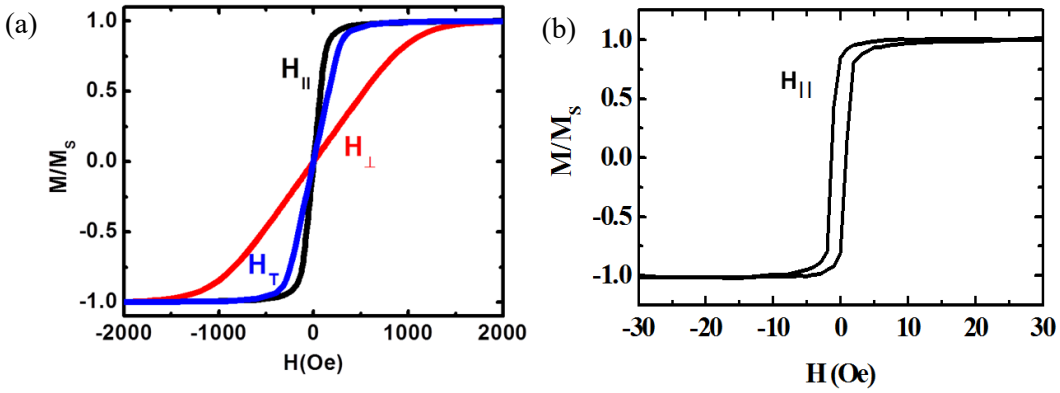

Fig. 6.3 (a) Magnetization for polycrystalline YIG. (b) Magnetization for single crystalline YIG.

6.3 Intrinsic Spin Seebeck Effect in Au/YIG

6.3.1 Experimental Methods

Thin Au films with wedged layer have been made by magnetron sputtering on YIG and patterned into parallel wires and Hall bars. As shown in Fig. 6.4, the wires are patterned parallel to the edges of the YIG substrates. The parallel wires are arranged with ascending order of thickness from 4 to 12 nm. Each wire is 4-mm long, 0.1-mm wide, and 2-mm apart. Another set of Hall bar patterned samples consist of one long segment for current leads and several short segments for voltage leads. We use the four-probe or two-probe measurement for the MR and thermal voltage measurements respectively. The multiple wires facilitate a systematic study of the thickness dependence of electric transport and thermal measurement under the same uniform thermal gradient with a temperature difference of 10 K. The sample was sandwiched between, and in thermal contact with, two large Cu blocks that kept at a constant temperature differing by 10 K as described in Chapter 2.

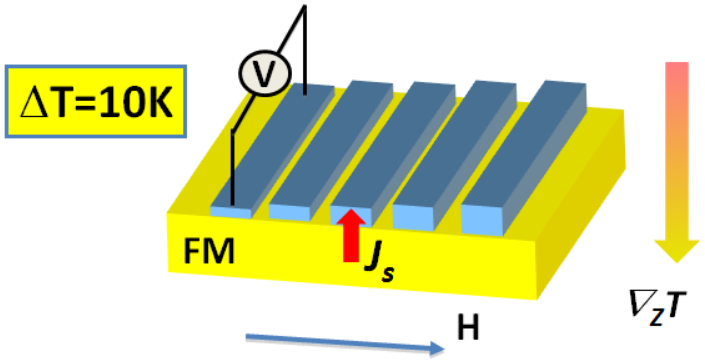

Fig. 6.4 Schematic drawing of the longitudinal spin Seebeck geometry with out of plane temperature gradient and patterned wedge film on top.

6.3.1 Resistivity of Au thin films

We first describe the thickness dependence of electrical resistivity (ρ) of the Au thin films. As expected ρ increases as the film thickness decreases as shown in Fig. 6.5. The results can be well described by a semiclassical theoretical model in the frame of the Fuchs-Sondheimer theory [8], which includes contributions from thickness (t) as well as the surface scattering (p) and grain boundary scattering (ξ)

$$\rho = \rho_{\infty} \frac{1 - (\frac{1}{2} + \frac{3\lambda}{4t})[1 - pe^{-t\xi/\lambda}]}{e^{-t/\lambda}}$$

For $t/\lambda > 0.1$, using bulk resistivity $\rho_{\infty} = 2.2$ μΩ-cm , and the mean free path $\lambda = 37$ *nm*, we find the data can be well described by $p = 0.89$ and $\xi = 0.37$ as shown by the solid line in Fig. 6.5(a). The thickness dependent resistivity for Pt is also shown in Fig. 6.5(b) for comparison.

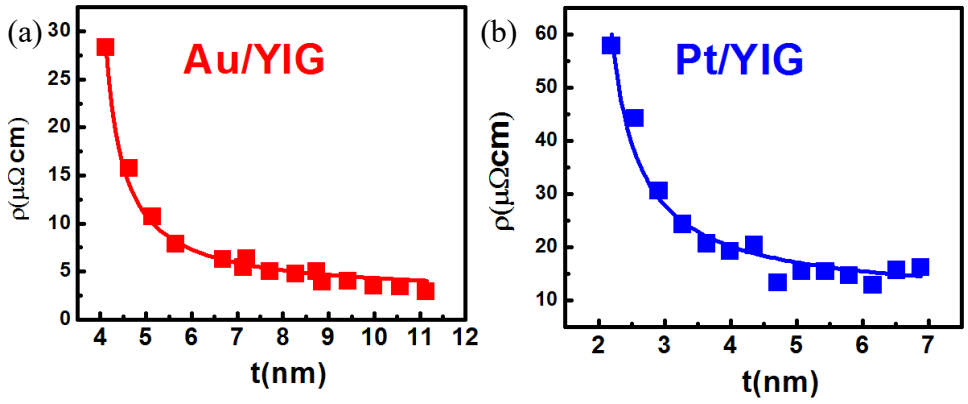

Fig. 6.5 Thickness dependent resistivity for (a) Au(t)/YIG and (b) Pt(t)/YIG.

6.3.2 Negligible Magnetic Proximity Effect

As mentioned in Chapter 5, magnetic proximity effect, revealed as the unexpected magnetoresistance, anomalous Hall effect and others, has complicated the unequivocal

realization of the intrinsic SSE. Despite the controversies in the magnetoresistances, the anomalous Hall effect remains to be an essential measurement for assessing the magnetic proximity effect.

The Hall measurements of the Au/Si and Au/YIG Hall bar samples have been taken from 2 to 300 K as shown in Fig 6.6. The Hall resistance of Au/YIG is linear in the magnetic field at all temperatures, showing only the ordinary Hall effect with no observable AHE. These Hall effect results are similar to those of Au/Si, where there is also MPE. In contrast, as shown in Chapter 5, strong AHE has been observed in Pt/YIG due to the acute MPE. The Hall constant ($R_H=1/ne$) of Au/YIG indicates the carrier concentration $n \approx 6\times10^{22}\text{cm}^{-3}$ as shown in Fig 6.6 (b), which are essentially constant from 2 to 300 K, in good agreement with the bulk carrier concentration of $n=5.9\times10^{22}\text{cm}^{-3}$. There is no injection that Au in Au/YIG is affected by MPE.

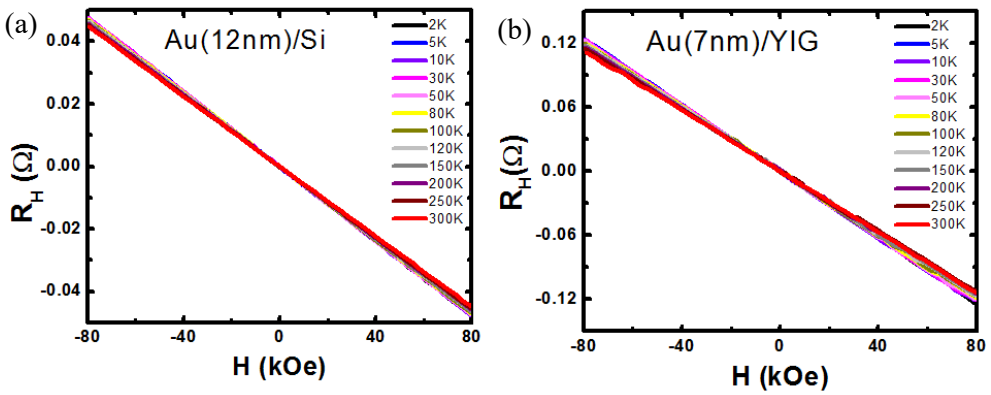

Fig. 6.6 Hall measurement for (a) Au(12 nm)/Si and (b) Au(7 nm)/YIG under different temperatures from 2 K to 300 K.

We have found very small magnetoresistance ratio $\Delta\rho/\rho \approx -4\times10^{-6}$, where $\Delta\rho =(\rho_{//}-\rho_T)$, in Au(7 nm)/YIG Hall bar sample, which is about 2 orders of magnitude smaller than that of Pt(t)/YIG as shown in Fig. 6.7. All the Au(t)/YIG with 4 nm< t <11

nm show similarly small but measurable $\Delta\rho/\rho$. More unexpectedly, the MR of Au(t)/YIG has the opposite angular dependence to that of the Pt MR dependence. The common behavior for either the AMR or new MR has positive $\Delta\rho$, that is, $\rho_{//} > \rho_T$, the resistivity with magnetic field parallel to, is higher than that perpendicular to the current direction. The mechanism of this very small negative MR, $\rho_{//} < \rho_T$, in Au(t)/YIG is not yet understood, and cannot be explained by any of the usual MR or proposed spin current based mechanisms. At any rate, the negligibly small MR and anomalous Hall effect in Au/YIG are strong evidence that the MPE in Au is negligible.

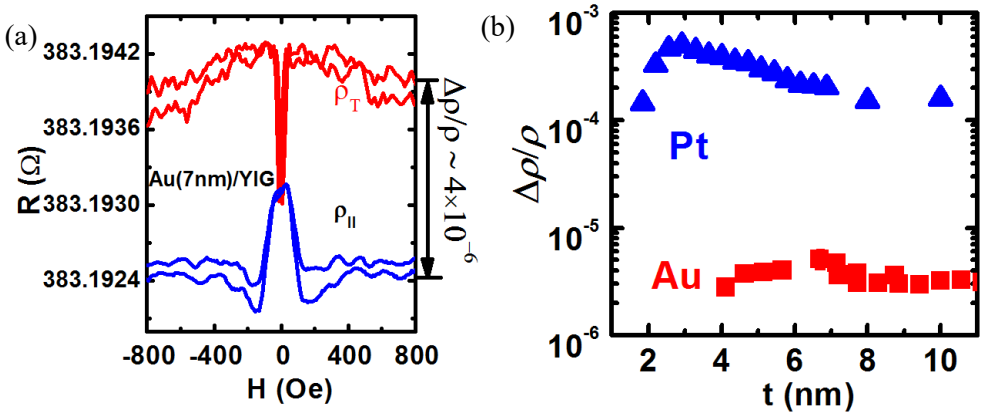

Fig. 6.7 (a) Magnetoresistance for the Au (7 nm)/YIG sample. (b) Thickness dependent MR ratio for Au (red) and Pt (blue) samples.

6.3.3 Intrinsic longitudinal Spin Seebeck effect in Au/YIG

After demonstrating that Au is free from the MPE in the Au/YIG structure, we employ the *longitudinal spin Seebeck* configuration to inject spin current from YIG into a series of Au thin films with different thicknesses. The results of Au/YIG are compared with those of Pt/YIG, Fig. 6.8(b). In both cases, the thermal voltage across either the Au or the Pt strip is asymmetrical with respect to the magnetic field that aligns the magnetization of the YIG. This is because when the spin Seebeck effect drives pure spin current in YIG,

magnetization direction of YIG dictates the spin orientation. When the pure spin current enters either Au or Pt, the spin orientation dictates the sign of the inverse spin Hall effect voltage.

The same sign of the thermal voltage, in this case the inverse spin Hall voltage, between Pt and Au indicates the positive values of spin Hall conductivity in Pt and Au. However, there are several differences between the thermal results of Au/YIG and Pt/YIG. We take ΔV_{th} as the magnitude of spin-dependent thermal voltage between the positive and the negative switching fields. As shown in Fig. 6.8(c) and (d), the value of ΔV_{th} of the Pt(t)/YIG is far larger, increasing sharply and unabatedly as t decreases to a value of $64\ \mu V$ at $t=2.2\ nm$. In contrast, the thermal voltage ΔV_{th} of the Au/YIG samples is much smaller than that of Pt/YIG and it varies with thickness (t) in a non-monotonic manner. The value of ΔV_{th} is negligible (less than 0.2 μV) for t<7 nm, increasing to a maximum of 1.3 μV at t = 8 nm before decreasing at larger thicknesses. Au is the material free from the MPE, therefore the non-monotonic thickness dependent ISHE voltage in Au should represent *intrinsic* behavior of spin current injected due to *only* the SSE in YIG without any contamination of other effect such as the MPE at the interfaces.

We describe further details about the non-monotonic behavior. Au has a long spin diffusion length, which is larger than 10 nm. When the thickness of Au is smaller than its spin diffusion length, the spins have not yet been effectively scattered and converted to charge current, meanwhile, the spin current flows backwards when reaching the surface or interfaces, creating a spin current back flow. Thus, when the film thickness increases, the ISHE signal also increases at smaller thickness due to the reasons mentioned above. The decrease of ISHE signal at larger thickness range is due to the decay of spin current

and the shunting effect of the thicker film.

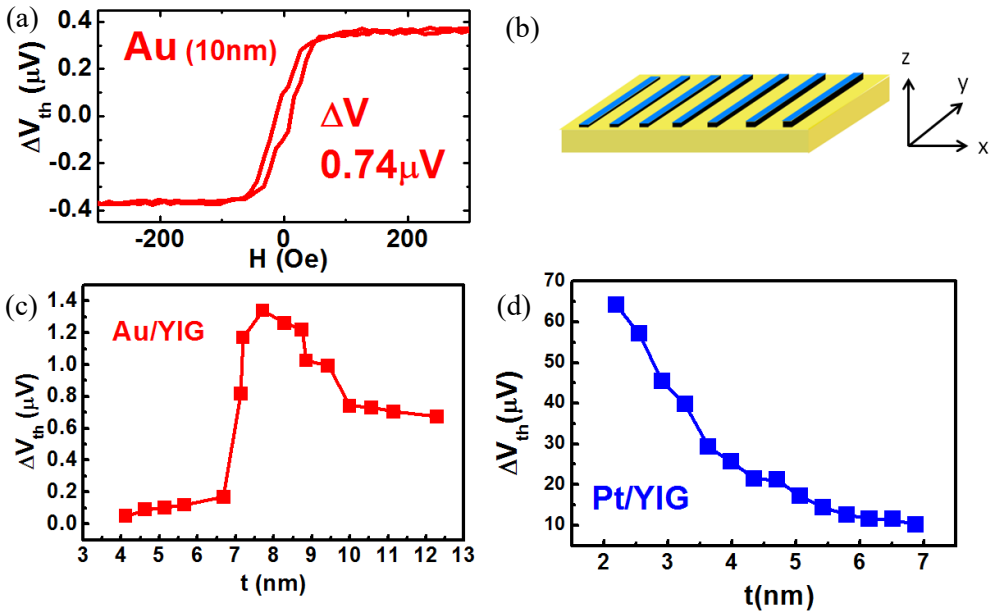

Fig. 6.8 (a) Inverse spin Hall voltage for 10 nm Au due to the thermal spin injection from YIG (b) Schematic drawing of the line patterned wedged thin metal film on YIG. (c)Thickness dependent thermal voltage for Au (red) and (d)Pt (blue) samples.

Moreover, first principles calculations have been carried out by our collaborators at the University of California, Irvine. They show a maximum local spin moment, *0.05 μB*, in Au, and *1.1 μB* in Pt atomic layers. Therefore, one can view Au as nearly "nonmagnetic" in contact with YIG, in contrast to Pt, which has a sizable moment. The sizable magnetic moments of Pt near the interface from the theoretical calculations is consistent with the strong MPE shown in the Pt(*t*)/YIG as we have described in the previous chapter. The negligible Au moments from theoretical calculations are also consistent with the observed absence of AHE in Au(*t*)/YIG described in this chapter. Given the weak negative MR and the nonexistent AHE, the acute magnetic proximity effects that plagued Pt/YIG do not affect Au/YIG. We have established the intrinsic

longitudinal spin Seebeck effect for the first time in Au/YIG as published in Phys. Rev. Lett. [6]. Professor *Saitoh's* group have also come to the same conclusion in Au/YIG and published [9] in the same issue of Physical Review Letters.

Reference to Chapter 6

1. K. Uchida, S. Takahashi, K. Harii, J. Ieda, W. Koshibae, K. Ando, S. Maekawa, and E. Saitoh, “Observation of the spin Seebeck effect”, Nature, **455**, 778 (2008)
2. C. M. Jaworski, J. Yang, S. Mack, D. D. Awschalom, J. P. Heremans and R. C. Myers, “Observation of the spin-Seebeck effect in a ferromagnetic semiconductor”, Nat. Mater. **9**, 898 (2010)
3. K. Uchida, H. Adachi, T. Ota, H. Nakayama, S. Maekawa and E. Saitoh, “Observation of longitudinal spin-Seebeck effect in magnetic insulators”, Appl. Phys. Lett. **97**, 172505 (2010)
4. S. Y. Huang, W. G. Wang, S. F. Lee, J. Kwo, and C. L. Chien, “Intrinsic spin-dependent thermal transport”, Phys. Rev. Lett. **107**, 216604 (2011)
5. S. Y. Huang, X. Fan, D. Qu, Y. P. Chen, W. G. Wang, J. Wu, T. Y. Chen, J. Q. Xiao, and C. L. Chien, “Transport magnetic proximity effect in platinum”, Phys. Rev. Lett. **109**, 107204 (2012)
6. D. Qu, S. Y. Huang, Jun Hu, Ruqian Wu, and C. L. Chien, “Intrinsic spin Seebeck effect in Au/YIG”, Phys. Rev. Lett. **110**, 067206 (2013)
7. C. Du, H. Wang, P. C. Hammel, and F. Yang, “Y3Fe5O12 spin pumping for quantitative understanding of pure spin transport and spin Hall effect in a broad range of materials (invited)” J. Appl. Phys. **117**, 172603 (2015)
8. P. Fan, K. Ti. J. D. Shao, and Z. X. Fau, “Electrical transport in metallic films”, J. Appl. Phys. **95**, 2527 (2004).

9. T. Kikkawa, K. Uchida, Y. Shiomi, Z. Qiu, D. Hou, D. Tian, H. Nakayama, X. –F. Jin, and E. Saitoh, “Longitudinal spin Seebeck effect free from the proximity Nernst effect”, Phys. Rev. Lett. **110**, 067207 (2013)

Chapter 7

Self-Consistent Method to Determine the Spin Hall Angle and Spin Diffusion Length in Non-magnetic Metals (Pt, Au, Ta, and W)

7.1 Introduction

After the observation of the spin Hall effect and inverse spin Hall effect in Pt and Au, various other *5d* materials have been demonstrated as effective spin current generators/converters, including Ta and W. [1-4] In this chapter, we study pure spin current phenomena and determine the spin Hall angle and spin diffusion length in these *5d* metals with pure spin current generated through the spin Seebeck effect in YIG.

Unlike a charge current, a pure spin current can only be preserved within a short distance of the order of the spin diffusion length λ_{SF}. While λ_{SF} in low-*Z* metals can be significant, its values in many nonmagnetic high-*Z* metals with a strong *SOC* are very small (only a few nm). The short λ_{SF} also creates serious challenges in spin current detection and the determination of θ_{SH}. [5]

As described in Sec. 3.4, the θ_{SH} values can be of either sign and of different magnitudes for different metals. However, experimental values of θ_{SH} for one metal can vary by as much as two orders of magnitude depending on the experimental technique or the analyses, and in some cases can disagree even in sign with theory. [6, 7] The disparity in the values of θ_{SH} is one of the most outstanding issues in pure spin current phenomena. The use of a magnetic insulator in this study circumvents the parasitic effects that may

plague metal/metal structures, for example, the shunting effect, spin backflow and the heating effect.

7.2 Spin Current Diffusion Model

We first describe the model used to calculate the spin Hall angle and spin diffusion length. This model is deduced based on experimental observation. It is similar to but not exactly the same as the magnon spin current model discussed in Sec. 4.4.

We first denote in our experiment the pure spin current injected into the metal film from SSE in YIG at the NM/YIG interface as

$$J_{SO} = C\nabla T \quad (1)$$

where C is the spin current injection coefficient and ∇T is the temperature gradient. Since the injection of spin current from a ferromagnet to a nonmagnetic layer is commonly characterized by the spin-mixing conductance $g_{eff}^{\uparrow\downarrow}$, which can be obtained from an FMR measurement, the spin current injection coefficient C should include the spin-mixing conductance $g_{eff}^{\uparrow\downarrow}$. The factor C should also contain the magnetic properties of the YIG substrate.

The bulk YIGs used in this dissertation have the same magnetization properties and surface qualities. The spin injection coefficient $g_{eff}^{\uparrow\downarrow}$ at the NM/FMI interface is therefore the same for the same NM metal. This has been confirmed by our consistency check as shown in Fig. 7.1. The values of $g_{eff}^{\uparrow\downarrow}$ may be different for different metals, but are all within the same order of magnitude [8]. Therefore, for simplicity, we may assume C to be the same for all the non-magnetic metals deposited on YIG.

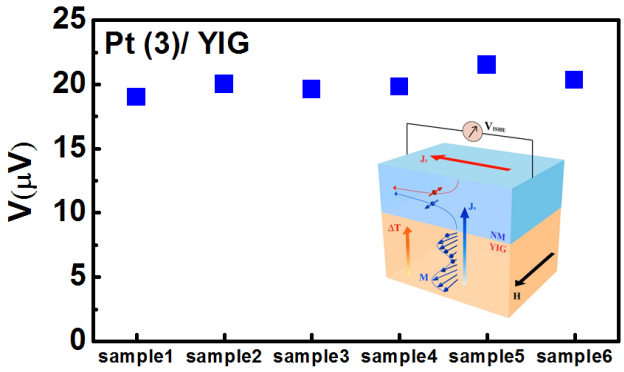

Fig. 7.1 Different samples with the same thickness Pt films deposited onto the YIG substrates. Inset is the schematic drawing of the spin Seebeck effect in the NM/YIG structure.

For the analyses, if one assumes the spin current is continuous across the interface, as the spin current enters into the metal along the z direction, its magnitude decreases as it traverses through the metal layer, Fig. 7.2. Based on the diffusion equation [9]

$$\nabla^2[\mu^{\sigma}(r) - \mu^{-\sigma}(r)] = \frac{\mu^{\sigma}(r) - \mu^{-\sigma}(r)}{\lambda_{SF}^2} \qquad (2)$$

Whose solution in the z direction is

$$\mu^{\sigma}(z) - \mu^{-\sigma}(r) = Aexp\left(\frac{z}{\lambda_{SF}}\right) + Bexp(-\frac{z}{\lambda_{SF}}) \qquad (3)$$

here $\mu^{\sigma}(z)$ is the chemical potential for spin index σ, and $\lambda_{SF}$is the spin diffusion length.

Considering the boundary condition

$$\frac{d\mu}{dz}|_{z=t_N} = 0 \text{ (the spin current vanishes on the surface)}$$

$$\text{and } \frac{d\mu}{dz}|_{z=0} = J_s^0 \text{ (the spin current is continuous at the interface)}$$

the spin current in the z direction decays as

$$J_s(z) = J_s^0 \frac{\sinh[(t_N - z)/\lambda_{SF}]}{\sinh(t_N/\lambda_{SF})} \quad (4)$$

where t_N is the thickness of the metal film, z is the distance from the interface at which the spin current density is J_s^0. The pure spin current is then converted to a charge current in the transverse direction through the ISHE according to

$$\boldsymbol{J_C} = \theta_{SH}\boldsymbol{J_S} \times \boldsymbol{\sigma} \quad (5)$$

One obtains the voltage due to the charge accumulation based on Ohm's Law as

$$\Delta V_{th}(t) = 2\rho(t)L < J_C > \quad (6)$$

Where $\rho(t)$is the resistivity of the thin metal film with thickness of t, L is the length of the wire, $< J_C >$ is the averaged charge current in the transverse direction. We define ΔV_{th} as voltage difference from positive to negative saturation field, and we obtain

$$< J_S >= \int_0^t J_s(z)dz = \int_0^t J_s^0 \frac{sinh[(t_N - z)/\lambda_{SF}]}{sinh(t_N/\lambda_{SF})} dz = J_s^0 \frac{\lambda_{SF}}{t} tanh(\frac{t_N}{2\lambda_{SF}}) \quad (7)$$

By combining equation (1), (4), (5), (6) and (7), one obtains

$$\Delta V_{th}(t) = 2[CL\nabla T][\rho(t)\theta_{SH}]\left[\left(\frac{\lambda_{SF}}{t}\right) tanh\left(\frac{t}{2\lambda_{SF}}\right)\right]. \quad (8)$$

The thermal voltage $\Delta V_{th}(t)$is the product of three factors as marked by the brackets, where $CL\nabla T$relates to spin injection efficiency, the length of the wire, and the temperature gradient, and $\rho(t)\theta_{SH}$ is a material-specific quantity. The last factor characterizes the decay of the thermal in space. Equation 8 is strongly thickness dependent, highlighting the importance of capturing the thickness dependence for quantitative determination of $\theta_{SH}$and λ_{SF}.

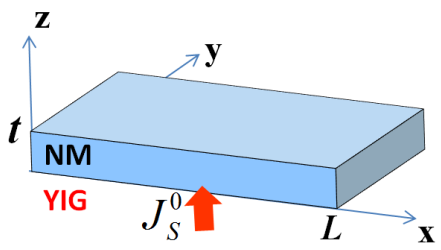

Fig. 7.2 Schematic drawing of the spin current enters into the NM metal layer from YIG.

By comparing *Eq. 8* with the magnon spin current model [10] discussed in Sec. 4.4, we obtain the quantity $C = -\frac{\gamma\hbar\rho' k_m^3 l_m}{4\pi M\pi^2}\frac{B_1 B_S}{B_2} g_{eff}^{\uparrow\downarrow} k_B$, which depends on the magnetic properties of YIG, such as the gyromagnetic ratio γ, magnetization M and magnon spin diffusion length l_m and the spin-mixing conductance $g_{eff}^{\uparrow\downarrow}$ at the metal/YIG interface, as we discussed previously. $\hbar$ is the reduced Planck constant, $\rho' = \frac{cosh(t_{FM}/l_m)-1}{sinh(t_{FM}/l_m)}$ is the finite FMI thickness factor, k_m is the maximum wave number, B_1, B_2 and B_S are parameters in diffusion equation, k_B is the Boltzman constant. Knowing C would allow us to determine the absolute value of the spin Hall angles in various materials.

7.3 Spin Hall Angle and Spin Diffusion Length in the *5d* metals

7.3.1 Thickness Dependent Resistivity

We first measured the thickness dependence of the resistivity for each material, including Pt, Au, Ta and W, deposited on YIG substrate with a patterned Hall bar structure. As shown in Fig. 7.3, the resistivity ρ of a thin film is constant at large thicknesses but increases as the film thickness decreases in the limit of a very thin film. This is due to the increase of surface scattering same as the thickness dependent resistivity in Au as described in Chapter 6.

At the same thickness, the resistivity for W is slightly smaller than that of Ta but much larger than those of Pt and Au. The variation of resistivity with thickness can be well accounted for by surface and boundary scattering, as described by the semiclassical Fuchs-Sondheimer theory [11]. The author also noticed that some reports attribute the increase of resistivity in Ta and W to the change of crystalline structures from α-Ta and α–W to β-Ta and β-W, respectively. [3, 4] In order to identify the existence of such phases, the author performed the x-ray diffraction studies mentioned in Chapter 2. However, only the α phase in W and a mix of α and β phase in Ta were found down to the film thickness of 10 nm.

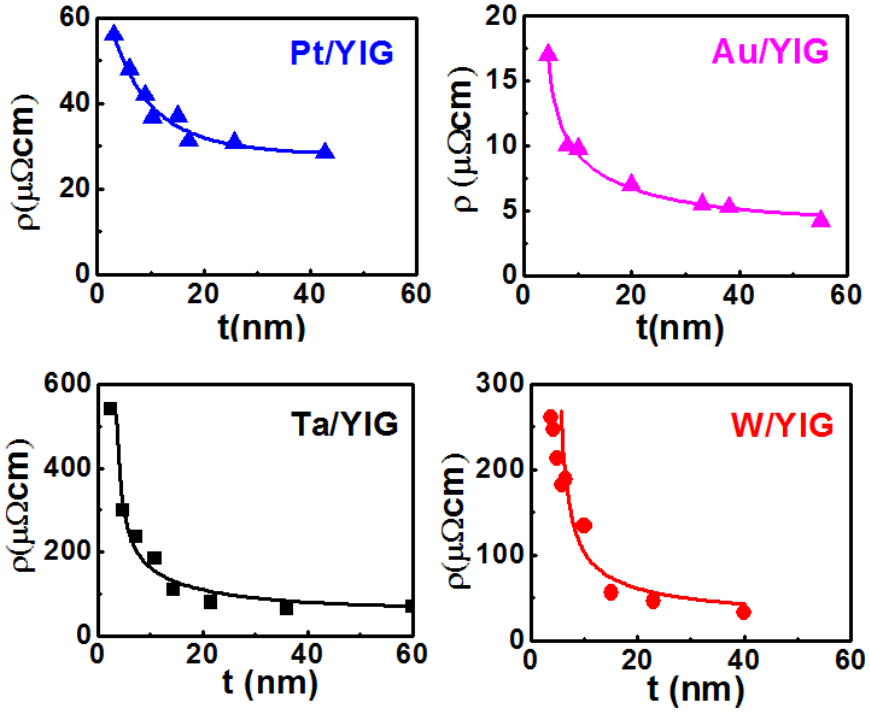

Fig. 7.3 Thickness dependent resistivity for Pt(t)/YIG (blue), Au(t)/YIG (pink), Ta(t)/YIG (black), and W(t)/YIG (red). Solid lines are fits to the semiclassical Fuchs-Sondheimer theory.

7.3.2 Thickness Dependent ISHE Voltage

We next describe thermal spin injection and conversion in these metallic thin films. [12] As shown in Fig. 7.4, the ISHE voltage of Pt, Au, Ta and W on YIG display an antisymmetric behavior as a function of the magnetic field. Under a temperature gradient of 20 K/mm, the thermal voltages of the L=5 mm long Ta (10 nm)/YIG and W (10 nm)/YIG are 2.1 μV and 6.0 μV, respectively. These values are slightly smaller than the 6.8 μV for Pt (10 nm)/YIG sample, but much larger than the 0.76 μV for Au (10 nm)/YIG sample of the same length. However, one should note here that although the thermal voltages for Ta, W, and Pt for the same thicknesses are comparable, this does not necessarily mean the spin Hall angles for these materials are similar. The large resistivity of Ta and W have consequences in the calculation of spin Hall angles in these materials.

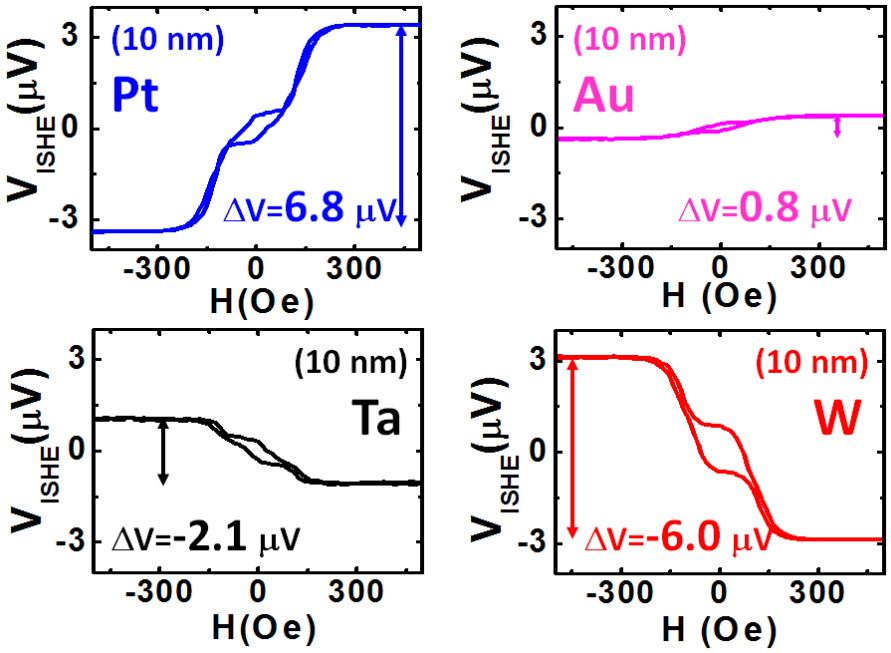

Fig. 7.4 Inverse spin Hall voltages for 10 nm thick Pt on YIG (blue), 10 nm Au onYIG (pink), 10 nm Ta on YIG (black), and 10 nm W on YIG (red) due to the thermal spin injection from YIG.

The results, shown in Fig. 7.4, clearly indicate that the sign of the spin Hall angle of Pt and Au is opposite to that of Ta and W, which is consistent with the theoretical calculations and other reports. The sign of the spin Hall angle is due to the *5d* electron filling. The spin Hall conductivity is proportional to $<\boldsymbol{l}\cdot\boldsymbol{s}>$, which is the expectation value of the spin orbit $\boldsymbol{l}\cdot\boldsymbol{s}$ coupling. [13] According to Hund's third rule, the sign of $\boldsymbol{l}\cdot\boldsymbol{s}$ is opposite for electron numbers of more than and less than half full. This simple argument is valid for the *5d* metals; the signs of the spin Hall angles in Ta and W (less than half full) are indeed opposite to those of Pt and Au (more than half full).

The thickness dependent thermal voltage is shown in Fig. 7.5. The decrease of the thermal voltages below the peak in the thin film limit is a result of the back flow of spin current. The decay of the thermal voltages above the peak is because of the short spin diffusion length in those films as captured by Equation (8).

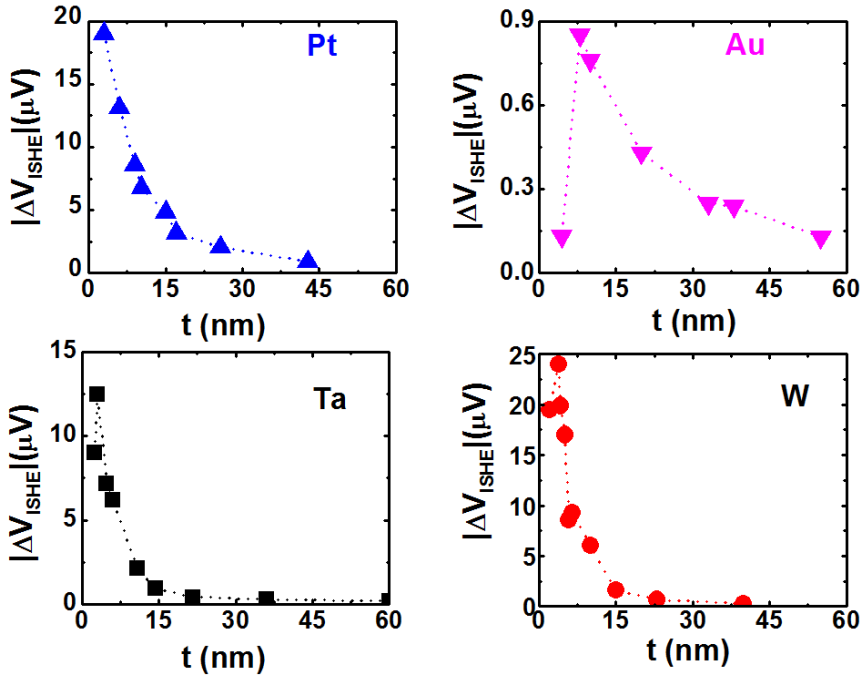

Fig. 7.5 Thickness dependent inverse spin Hall voltage for Pt(*t*)/YIG (blue), Au(*t*)/YIG (pink), Ta(*t*)/YIG (black), and W(*t*)/YIG (red) due to the thermal spin injection from YIG. Dashed lines are guides to the eyes.

7.3.3 Determination of Spin Hall Angle and Spin Diffusion Length

With the thickness dependent resistivity and ISHE voltage, we are able to determine the spin Hall angle and spin diffusion length of these *5d* metals. We rewrite *Eq. 8* as

$$\frac{\Delta V_{th}(t)}{\rho(t)} = 2[CL\nabla T][\theta_{SH}]\left[\left(\frac{\lambda_{SF}}{t}\right)\tanh\left(\frac{t}{2\lambda_{SF}}\right)\right] \quad (9)$$

and fit the $\frac{\Delta V_{th}(t)}{\rho(t)}$ data to *Eq. 9* to obtain λ_{SF} and the values of $[CL\nabla T][\theta_{SH}]$, which contains the spin Hall angle for each material, as shown in Fig. 7.6.

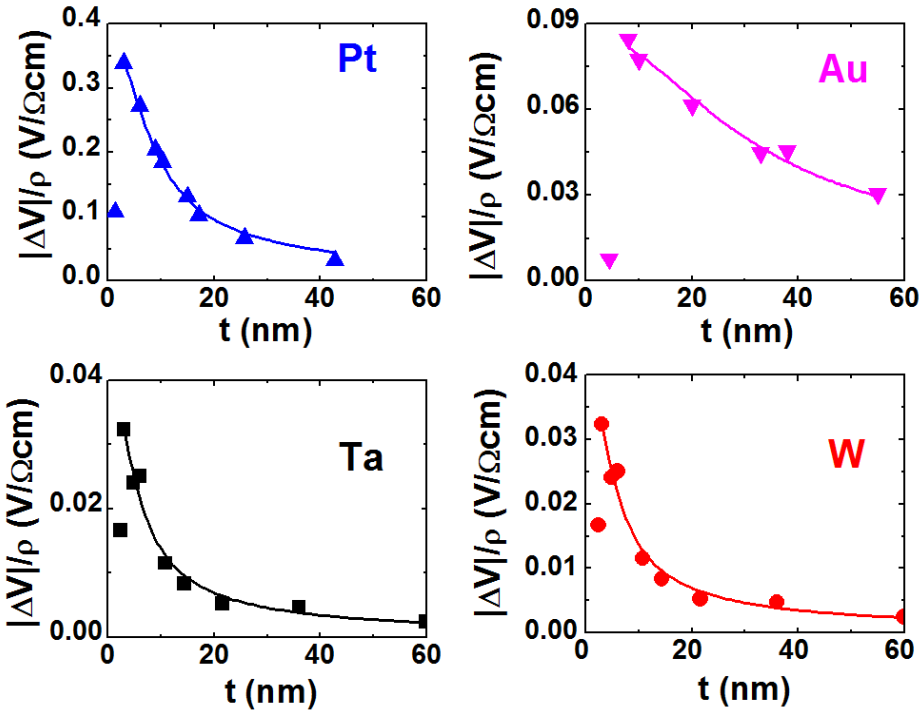

Fig. 7.6 Thickness dependent inverse spin Hall voltage over resistivity for Pt(t)/YIG (blue), Au(t)/YIG (pink), Ta(t)/YIG (black), and W(t)/YIG (red) for the calculation of spin Hall angle and spin diffusion lengths in these materials. Solid lines are fits to Eq. 9.

Spin Diffusion Length and Relative Spin Hall Angle

We have no capability to measure the spin-mixing conductance contained in the spin injection efficiencies *C* in these materials. For simplicity, if we assume that the spin injection efficiency *C* is the same for all the materials, we can obtain a relative spin Hall angle using Au as reference, and the spin diffusion length in these materials:

$$\theta_{SH}/\theta_{SH}\ (Au) = 4.33 \pm 1.33\ (Pt), 1.00 \pm 0.33\ (Au),$$

$$-0.46\ \pm 0.13(Ta), and - 1.43 \pm 0.53\ (W)$$

$$\lambda_{SF} = 2.5 \pm 0.1\ nm\ (Pt), 9.5 \pm 0.7\ nm\ (Au),$$

$$1.7 \pm 0.3\ nm\ (Ta), and\ 1.5 \pm 0.6\ nm\ (W)$$

Absolute Spin Hall Angle

In fact, different spin mixing conductance for different NM/YIG heterostructures at the interfaces have been reported by *Wang et. al.*:

$$g_{eff}^{\uparrow\downarrow} = 6.91 \times 10^{18}\ m^{-2}\ (Pt), \qquad 2.66 \times 10^{18}\ m^{-2}\ (Au),$$

$$5.35 \times 10^{18}\ m^{-2}\ (Ta), \qquad 4.54 \times 10^{18}\ m^{-2}\ (W)$$

If we borrow these values and the magnetic properties described in Sec.4.4, we calculate for each metal

$$C_0 = -\frac{\gamma\hbar\rho' k_m^3 l_m}{4\pi M\pi^2}\frac{B_1 B_S}{B_2} g_{eff}^{\uparrow\downarrow} k_B$$

$$C_0 = 2.03\times10^{-15} Jm^{-1}K^{-1}(Pt), \quad 0.78\times10^{-15} Jm^{-1}K^{-1}(Au),$$

$$1.56\times10^{-15} Jm^{-1}K^{-1}(Ta), \quad 1.33\times10^{-15} Jm^{-1}K^{-1}(W)$$

$$C = \frac{2e}{\hbar} C_0$$

$$C = 6.16\, Am^{-1}K^{-1}(Pt), \quad 2.36\, Am^{-1}K^{-1}(Au),$$

$$4.72\, Am^{-1}K^{-1}(Ta), \quad 4.03\, Am^{-1}K^{-1}(W)$$

Therefore, the absolute spin Hall angles for these materials are

$$\theta_{SH} = 0.08 \pm 0.025(Pt), 0.034 \pm 0.01\,(Au),$$

$$-0.016 \pm 0.005\,(Ta), and -0.047 \pm 0.017\,(W)$$

These values are within the broad ranges reported for Pt, Au, Ta, and W using nonlocal, spin pumping, etc. as shown in Table 7.1. [14]

One notes here the thermal voltages $|\Delta V_{th}(t)|$for Ta and W are similar to that of Pt, where W is the largest followed by Pt, Ta, and Au. On the other hand, the θ_{SH} values for Ta and W are much smaller than Pt. This underscores the essential role of resistivity. If the resistivity of the thin metal layer had not been measured and included in the analyses, one would have obtained thickness-dependent and exaggerated θ_{SH} values. As shown in Eq. (8), a large ISHE voltage relies on both a large θ_{SH}, and a large ρ. We define the spin Hall resistivity as $\rho_{SH} = \rho\theta_{SH}$, which is a key parameter in the pure spin

current devices. The values of the spin Hall resistivity for the 10 nm thin films are also shown in Table.

	Pt	**Au**	**Ta**	**W**
θ_{SH} *(reference)*	0.0037~0.08	0.0016~0.113	-0.0037~ -0.15	-0.07~ -0.33
θ_{SH}/θ_{Au} (this work)	4.33 (±1.33)	1.00 (±0.33)	-0.46 (±0.13)	-1.43 (±0.53)
$g_{eff}^{\uparrow\downarrow}$ *(m^{-2} reference)*	6.91×10^{18}	2.66×10^{18}	5.35×10^{18}	4.54×10^{18}
θ_{SH} (this work)	0.08 (±0.025)	0.034 (±0.01)	-0.016 (±0.005)	-0.047 (±0.017)
λ_{SF} (nm)	2.5 (±0.1)	9.5 (±0.7)	1.7 (±0.3)	1.5 (±0.6)
ρ_{SH} ([$2e/\hbar$]μΩcm)	2.95	0.33	-2.97	-4.7

Table 7.1 Spin Hall angles in literatures, the relative spin Hall angles obtained from this work, the spin mixing conductance in literatures, the absolute spin Hall angles, the spin diffusion lengths, and the spin Hall resistance for Pt, Au, Ta and W.

Thus, we have demonstrated a self-consistent, simple, and versatile method to determine the spin Hall angle by using the longitudinal spin Seebeck effect to inject spin current from the ferromagnetic insulator YIG to several *5d* metals including Pt, Au, Ta and W. It is essential to conduct thickness dependence studies with suitable analyses to quantitatively determine the spin Hall angle θ_{SH} and spin diffusion length λ_{SF}. The thermal voltage readily reveals the sign of θ_{SH}: The signs for Pt and Au are opposite to those of Ta and W. We show that both a large charge resistivity and spin Hall angle, i.e. a large spin Hall resistivity ρ_{SH}, are essential for a large inverse spin Hall voltage.

7.4 Magnetic Proximity Effect in Ta/YIG and W/YIG

Finally, we describe the unusual new magnetoresistance (MR) observed in these *5d* metals in proximity to the ferromagnetic insulator YIG. Non-magnetic metals, such as Pt, Ta, and W in isolation show no MR. However, Pt/YIG, Ta/YIG and W/YIG show the new MR as described in Chapter 5. [15, 16] The MR of the longitudinal resistivity $\rho_{\parallel}$ (with $\boldsymbol{M} \parallel I$) and transverse resistivity ρ_{T} (with $\boldsymbol{M} \perp I$ in-plane), share the same field dependence as that of the magnetization of the underlying YIG, as shown in Fig. 7.7(a). In contrast, perpendicular resistivity $\rho_{\perp}$ (with $\boldsymbol{M} \perp I$ out-of-plane) shows features of the new MR, with $\rho_{\perp} \approx \rho_{\parallel} > \rho_{\mathrm{T}}$ (Fig. 7.7(b)), which are distinct different from the well-known AMR with $\rho_{\parallel} > \rho_{\mathrm{T}} \approx \rho_{\perp}$. Furthermore, the magnitude of the new MR increases with decreasing film thicknesses (Fig. 7.7(c)), highlighting the interfacial contribution.

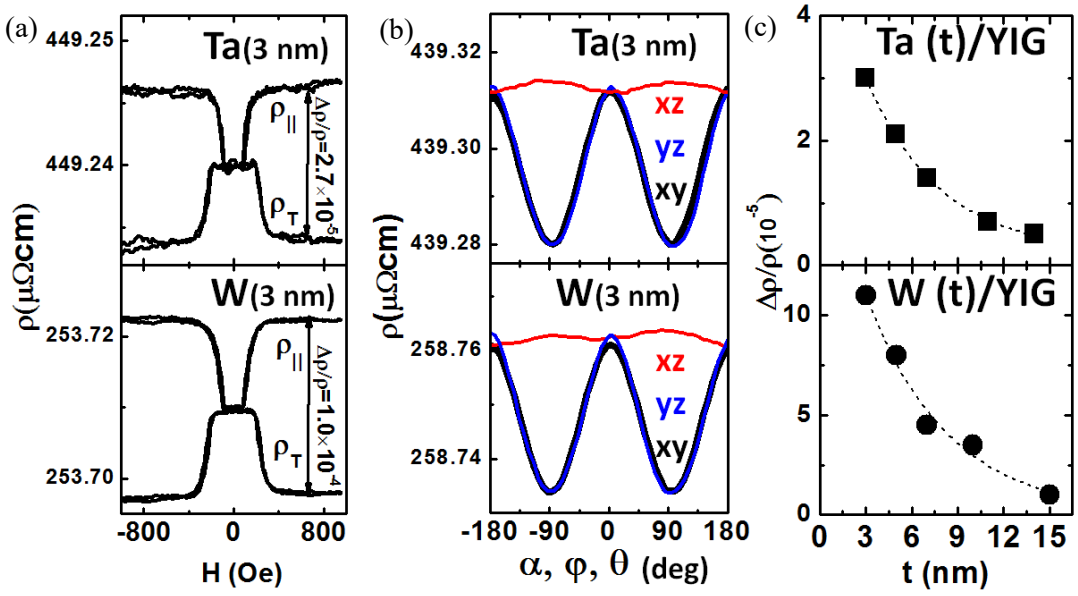

Fig. 7.7 (a) Magnetoresistance for Ta(3 nm)/YIG and W(3 nm)/YIG. (b) xz, yz and xy magnetic field angular dependent magnetoresistance for Ta(3 nm)/YIG and W(3 nm)/YIG. (c) Thickness dependent MR ratio for Ta(t)/YIG and W(t)/YIG.

In addition to the new MR, we have also made Hall effect measurements. The Hall resistance of Ta(10 nm)/SiO2 and W(10 nm)/SiO2 is linear in the magnetic field showing only the ordinary Hall effect (OHE) as shown in Fig. 7.8(a). In contrast, we have observed the anomalous Hall effect (AHE) in Ta(6 nm)/YIG and W(6 nm)/YIG as shown in Fig. 7.8(b). The AHE resistance R_{AHE} shows a strong temperature dependence. It is worth noting that R_{AHE} is positive for Ta and W, whereas that of Pt changes sign as shown in Fig. 7.8(c). Furthermore, R_{AHE} of Pt shows large enhancement at low temperatures. The evidences of MPE in Pt/YIG, Ta/YIG and W/YIG question whether the experimental values of θ_{SH} are intrinsic and can be compared with those from theoretical calculations including no MPE.

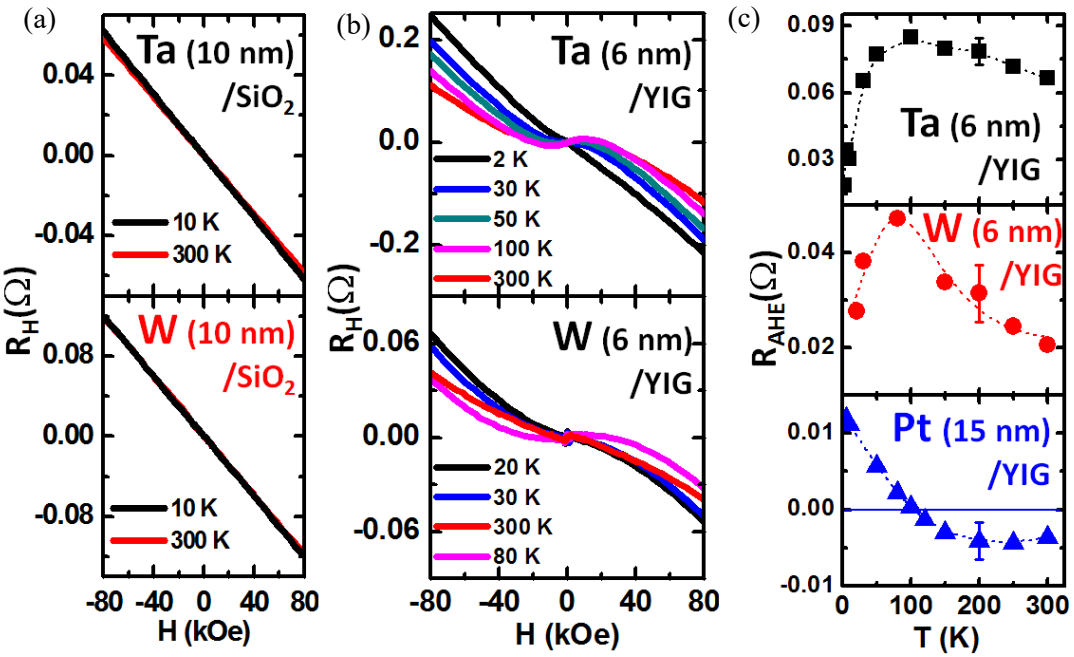

Fig. 7.8 (a) Ordinary Hall resistance for Ta(10 nm) and W(10 nm) thin film on SiO_2.(b) Hall effect measurement for Ta(6 nm) and W(6 nm) on YIG under different temperatures. (c) Temperature dependent anomalous Hall resistance for Ta(6 nm)/YIG, W(6 nm)/YIG and Pt(15 nm)/YIG.

Reference to Chapter 7

1. M. Morota, Y. Niimi, K. Ohnishi, D. H. Wei, T. Tanaka, H. Kontai, T. Kimura, and Y. Otani, "Indication of intrinsic spin Hall effect in *4d* and *5d* transition metals", Phys. Rev. B **83**, 174405 (2011).
2. L. Liu, T. Moriyama, D. C. Ralph, and R. A. Buhrman, "Spin-torque ferromagnetic resonance induced by the spin Hall effect", Phys. Rev. Lett. **106**, 036601 (2011).
3. L. Liu, C. Pai, Y. Li, H. W. Tseng, D. C. Ralph, R. A. Buhrman, "Spin-torque switching with the giant spin Hall effect of Tantalum", Science **336**, 555 (2012).
4. C. Pai, L. Liu, Y. Li, H. W. Tseng, D. C. Ralph, R. A. Buhrman, "Spin transfer torque devices utilizing the giant spin Hall effect of tungsten", Appl. Phys. Lett. **101**, 122404 (2012).
5. J. Bass and W. P. Pratt Jr., "Current-perpendicular (CPP) magnetoresistance in magnetic metallic multilayers", J. Magn. Magn. Mater. **200**, 274 (1999)
6. M. Gradhand, D. V. Fedorov, P. Zahn, and I. Mertig, "Spin Hall angle versus spin diffusion length: Tailored by impurities", Phys. Rev. B **81**, 245109 (2010)
7. Y. Niimi, Y. Kawanishi, D. H. Wei, C. Deranlot, H. X. Yang, M. Chshiev, T. Valet, A. Fert, and Y. Otani, "Giant spin Hall effect induced by skew scattering from Bismuth impurities inside thin film CuBi alloys", Phys. Rev. Lett. **109**, 156602 (2012)
8. H. L. Wang, C. H. Du, Y. Pu, R. Adur, P. C. Hammel, and F. Y. Yang, "Scaling of spin Hall angle in 3d, 4d, and 5d metals from YIG/metal spin pumping", Phys. Rev. Lett. **112**, 197201 (2014)

9. O. Mosendz, J. E. Pearson, F. Y. Fradin, G. E. W. Bauer, S. D. Bader, and A. Hoffmann, "Quantifying spin Hall angles from spin pumping: experiments and theory", Phys. Rev. Lett. **104**, 046601 (2010)
10. S. M. Rezende, R. L. Rodriguez-Suarez, R. O. Cunha, A. R. Rodrigues, F. L. A. Machado, G. A. Fonseca Guerra, J. C. Lopez Ortiz, and A. Azevedo, "Magnon spin-current theory for the longitudinal spin-Seebeck effect", Phys. Rev. B **89**, 014416 (2014)
11. P. Fan, K. Ti. J. D. Shao, and Z. X. Fau, "Electrical transport in metallic films", J. Appl. Phys. **95**, 2527 (2004).
12. D. Qu, S. Huang, B. F. Miao, S. X. Huang, and C. L. Chien, "Self-consistent determination of spin Hall angles in selected *5d* metals by thermal spin injection", Phys. Rev. B **89**, 140401 (R) (2014)
13. T. Tanaka, H. Kontani, M. Naito, T. Naito, D. S. Hirashima, K. Ymada, and J. Inoue, "Intrinsic spin Hall effect and orbital Hall effect in *4d* and *5d* transition metals", Phys. Rev. B **77**, 165117 (2008)
14. A. Hoffmann, "Spin Hall effects in metals", IEEE Trans. Mag. **49**, 10 (2013)
15. S. Y. Huang, X. Fan, D. Qu, Y. P. Chen, W. G. Wang, J. Wu, T. Y. Chen, J. Q. Xiao, and C. L. Chien, "Transport magnetic proximity effect in platinum", Phys. Rev. Lett. **109**, 107204 (2012)
16. Y. M. Lu, J. W. Cai, S. Y. Huang, D. Qu, B. F. Miao, and C. L. Chien, "Hybrid magnetoresistance in the proximity of a ferromagnet", Phys. Rev. B **87**, 220409(R) (2013)

Chapter 8

Inverse Spin Hall Effect in Magnetic Metals: Ferromagnetic (Py and Co) and Antiferromagnetic (Cr)

8.1 ISHE in Ferromagnetic Metals

8.1.1 Introduction

In a ferromagnetic metal, electrons are polarized with unequal populations of opposite spins. When a charge current of density J_C flows in a ferromagnetic metal with spontaneous magnetization, the anomalous Hall effect compels unequal numbers of electrons of opposite spins to drift in opposite directions, thus creating a spin-polarized current of density J_{SP} in the transverse direction. The unequal numbers of electrons accumulated at the opposite edges of the sample give the anomalous Hall effect voltage, which can be directly detected by electrical means. Details of the AHE have been discussed in Sec. 3.3.

The interesting scenario is when a pure spin current is injected into a ferromagnetic metal as shown in Fig. 8.1. Similar to the situation of ISHE in a non-magnetic metal, one may expect ISHE in a ferromagnetic metal to generate a transverse charge current and charge accumulation at the edges. However, demonstration of ISHE in a ferromagnetic metal is more challenging for a few reasons: most of the spin current generation methods discussed in Sec.3.2.4 involve ferromagnetic metals as spin current

source; the presence of the charge current and other effects associated with the ferromagnetic metals need also to be corrected. [1, 2] Therefore, in order to verify the ISHE in a ferromagnetic metal, proper choice of spin current source and careful experimental design and analysis are required.

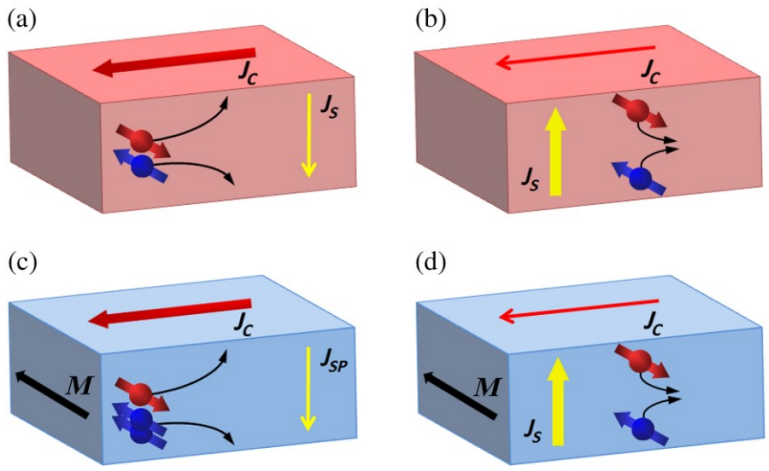

Fig. 8.1 Schematic drawing of (a) spin Hall effect, (b) inverse spin Hall effect, (c) anomalous Hall effect, and (d) inverse spin Hall effect in a ferromagnetic material.

8.1.2 Observation of ISHE in Py

In order to experimentally realize the ISHE in ferromagnetic metals, we use the longitudinal SSE in YIG via an out-of-plane temperature gradient to inject spin current into an attached Py layer. [3, 4] For non-magnetic metals, such as Pt, the structure of Pt/YIG would be sufficient to realize ISHE. However, for the ferromagnet Py, the Py/YIG structure is inadequate: in additional to the pure spin current effect, Py itself under the same temperature gradient would generate an anomalous Nernst voltage (ANE), which is added to and complicates the obtained thermal voltage. To unequivocally establish ISHE in Py due to the spin current injection from YIG, one must separate the ANE contribution and ISHE contribution. Note that if the pure spin current can be

blocked from entering Py, there would be no ISHE but only the ANE generated within Py. The methods used to block the pure spin current injection from YIG into the attached metal layer are described in the following.

In the metal/YIG sample, by altering the YIG surface, e.g., by physical ion bombardment before thin metal film deposition or by inserting an insulating layer between YIG and the metal layer, the pure spin current transport across the interface can be completely stopped. [5] As shown in Fig. 8.2, prior to the metal deposition, we have used Ar-ion beam bombardment (500 V, current density 0.4 mA/cm^2) on the YIG substrate for 5 mins to alter the surface, or depositing a 5-nm thick MgO layer on YIG. These samples are denoted as YIG_{BB}, where the subscript BB denotes 5 mins of ion bombardment, and MgO(5 nm)/YIG, respectively.

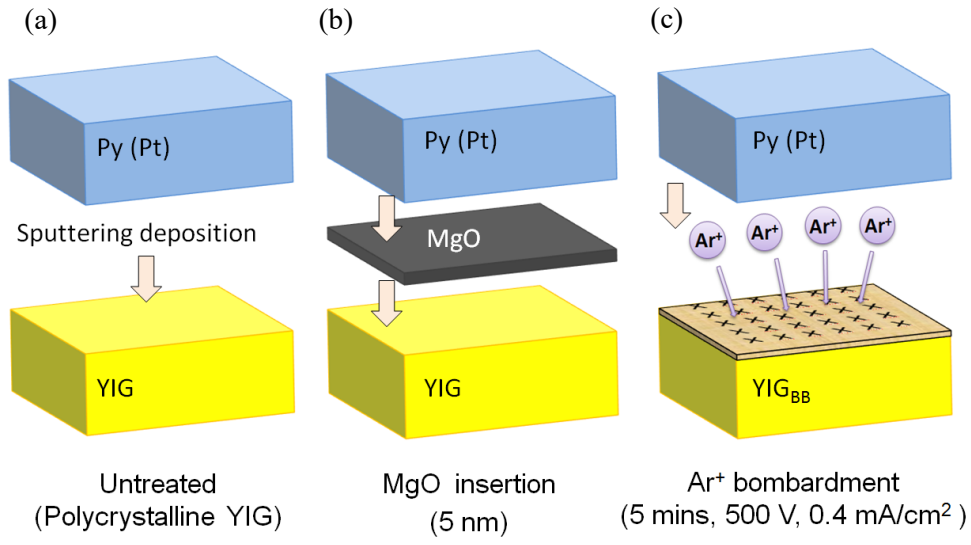

Fig. 8.2 Schematic drawing of (a) untreated YIG surface, (b) insertion of an MgO layer, and (c) Ar^+ bombardment of the YIG surface.

We first demonstrate the spin current blockage in the Pt/YIG sample with the above interfacial treatment. While a large V_{th} exists in Pt(3 nm)/YIG, there is no

measureable spin dependent thermal voltage in Pt(3 nm)/YIG_{BB} and Pt(3 nm)/MgO(5 nm)/YIG, shown as the red and blue horizontal lines in Fig. 8.3, respectively. Therefore, altering the YIG interface by either ion bombardment or by inserting a 5-nm MgO layer can completely block spin current injection into the metal layer. This crucial aspect will be exploited in extracting the ISHE in Py. It also underscores the importance of the quality of the metal-YIG interface for spin current injection.

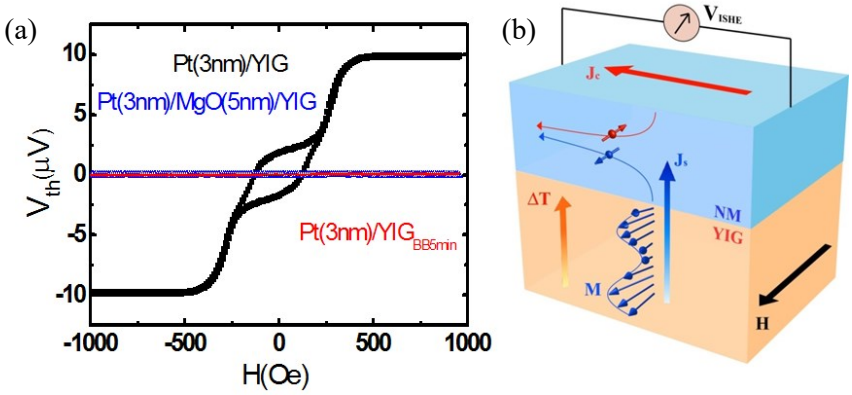

Fig. 8.3 (a) Inverse spin Hall voltage in Pt(3 nm) due to the thermal spin injection from untreated YIG (black), 5 nm MgO insertion at the interface between Pt/YIG (blue), and 5 min Ar^+ bombardment of YIG. (b) Schematic drawing of the thermal spin injection into the metal layer from YIG.

We next discuss the Py/YIG sample. In Py/YIG sample, Fig 8.4(a), under a temperature gradient, there is V_{ANE} within ferromagnetic Py of $V_{ANE} \propto \nabla_z T \times m$, where m denote the direction of magnetization, and V_{ISHE} from spin current of $V_{ISHE} \propto J_S \times \sigma$, where J_s is the spin current direction and σ is the spin index. Thanks to the magnetic coupling between Py and YIG, σ is parallel to m. Because of the longitudinal spin Seebeck effect in YIG, $\nabla_z T$ is parallel to J_s. Therefore, V_{ISHE} and V_{ANE} have the same magnetic field angular dependence and are additive and inseparable. As explained above

the interface treated Py/YIG_{BB} and Py/MgO/YIG samples contain only the V_{ANE} because of the spin current blockage at the interface, Fig. 8.4 (b). We shall use these to separate the ISHE from the ANE.

As shown in Fig. 8.4(c), the Py(5 nm)/YIG sample exhibits a thermal voltage ΔV_{th} with a magnitude of 4.2 μV, which consists of both the V_{ANE} and V_{ISHE}. The Py(5 nm)/YIG_{BB} and Py(5 nm)/MgO(5 nm)/YIG samples exhibit the same results with a magnitude of 0.9 μV, where only V_{ANE} in Py contributes. As a result, the maximal thermal voltage decreases substantially from 4.2 to 0.9 μV. The large difference of ΔV_{th} between the unaltered interface and the altered interface of Py/YIG samples is the *direct evidence* of the spin current injection and conversion in Py, demonstrating the inverse spin Hall effect in the ferromagnetic material Py.

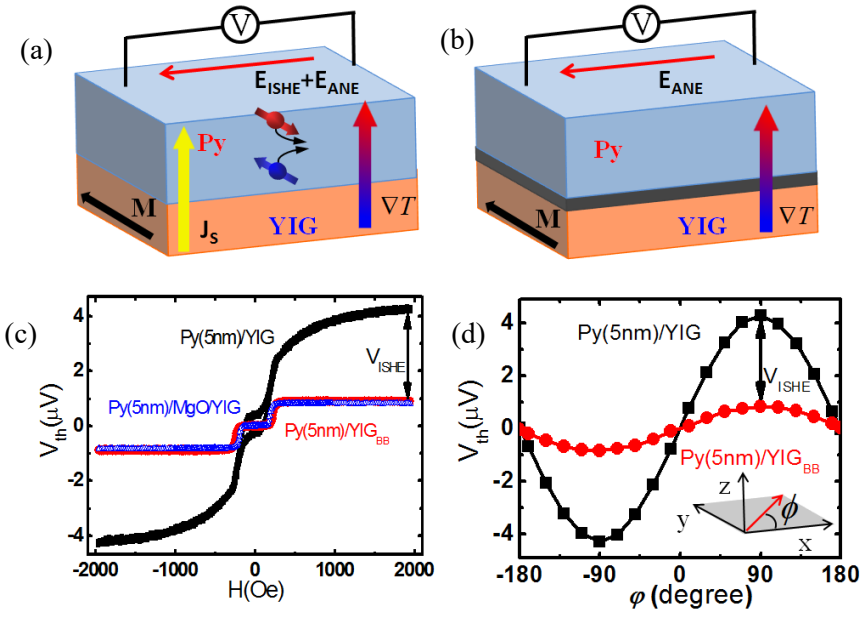

Fig. 8.4 (a) Schematic drawing of the thermal spin injection from YIG to Py. (b) Schematic drawing of the thermal spin injection from the treated YIG to Py. (c) Thermal voltage for Py (5 nm)/YIG (black), Py(5 nm)/MgO/YIG(blue), and Py(5 nm)/YIG_{BB}(red). (d) Magnetic field angular dependent thermal voltage for Py(5 nm)/YIG (black) and Py(5 nm)/YIG_{BB}(red).

The angular dependence of ΔV_{th} for Py(5 nm)/YIG and Py(5 nm)/YIG_{BB} is shown in Fig. 8.4(d). Both curves follow the $sin\phi$ field angular dependence, confirming that the V_{ANE} and V_{ISHE} share the same angular dependence, and the V_{ISHE} is the voltage difference between the two curves. This is the *first time* inverse spin Hall effect has been demonstrated in a ferromagnetic metal.

8.1.3 Spin Hall Angle and Spin Diffusion Length in Py

The demonstration of the ISHE in Py leads to several important questions: what is the spin/charge conversion efficiency in Py, and how far can the spin current transport without losing its information? In order to determine the spin Hall angle θ_{SH} and the spin diffusion length λ_{SF} in Py, a series of Py samples with different thickness have been fabricated and measured. By subtracting the V_{ANE} from the total ΔV_{th}, we obtain the V_{ISHE} in each case. Fig. 8.5 displays the dependence of resistivity ρ and V_{ISHE} on Py thickness. While at large thicknesses ρ is a constant, at small thickness ρ increases as the film thickness decreases thanks to surface scattering, the same behavior as seen in the *5d* metal thin films on YIG. From the thickness-dependent resistivity and ISHE voltage, we are able to extract θ_{SH} and λ_{SF} of Py according to equation discussed in the previous chapter. [4]

$$V_{ISHE}(t) = [CL\nabla T][\rho(t)\theta_{SH}]\left[\left(\frac{\lambda_{SF}}{t}\right)tanh\left(\frac{t}{2\lambda_{SF}}\right)\right]$$

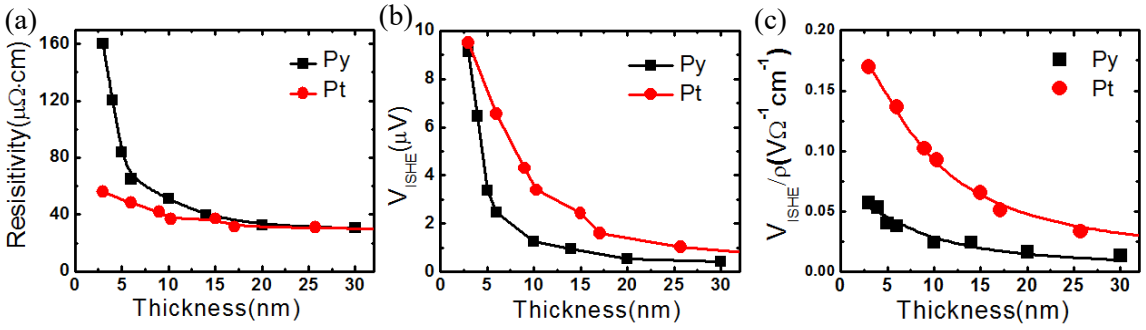

Fig. 8.5 Thickness dependent (a) resistivity, (b) inverse spin Hall voltage, and (c) voltage over resistivity for Py(t)/YIG (black) and Pt(t)/YIG (red) samples. Solid lines in (a) and (b) are guides to the eyes and in (c) is fitting to $V_{ISHE}(t) = [CL\nabla T][\rho(t)\theta_{SH}]\left[\left(\frac{\lambda_{SF}}{t}\right) tanh\left(\frac{t}{2\lambda_{SF}}\right)\right]$.

The spin Hall angle for Py relative to Pt is 0.38 assuming the same spin injection coefficient. If we take the spin mixing conductance of Py/YIG ($g_{eff}^{\uparrow\downarrow} = 1 \times 10^{18} m^{-2}$), the absolute spin Hall angle of Py is θ_{SH}=*0.033±0.003*. This result shows that Py has a large spin Hall angle comparable to those of the heavy *5d* metals. The spin diffusion length λ_{SF}=*2.5 nm* is consistent with those reported in Py.[6] This also indicates that the spin current in Py is mainly carried by the conduction electrons. This first demonstration of the inverse spin Hall effect in Py paves the way to exploiting many other ferromagnetic metals as superior pure spin current detectors for exploring pure spin current effects and applications.

8.2 Separation of ISHE and ANE in Co/Cu/YIG

It has been demonstrated in Sec. 8.1 that a ferromagnetic material can be used as an efficient pure spin current detector. However, as described above, even for the Py/YIG geometry without the complication of many other effects, we still need two samples, one of which serving as a reference to subtract the parasitic anomalous Hall effect

contribution. It would be more desirable if one could accomplish the observation of ISHE in FM using only one sample. In this section, we describe such a method. We also discuss the relationship between ferromagnetic ordering and the ISHE.

8.2.1 Separation of Inverse Spin Hall Voltage (ISHE) and Anomalous Nernst Voltage (ANE) in Co/Cu/YIG

To achieve the separation of V_{ISHE} and V_{ANE}, the sandwich structure Co/Cu/YIG with carefully designed layer thicknesses is used. [7] Here, we use the 120 nm *thin film* YIG grown on GGG instead of the bulk YIG substrate; otherwise the ferromagnetic thin film would be strongly coupled to the bulk YIG substrate even with a non-magnetic insertion layer. We use a thin Co layer to take advantage of its large magnetic coercivity. Finally, we use a thin Cu layer to decouple the two ferromagnets of Co and YIG and rely on its long spin diffusion length to ensure transmission of the pure spin current.

The magnetization response of the Co (2 nm)/Cu (5 nm)/YIG (120nm)/GGG sample is shown in Fig. 8.6. Distinctive steps are observed when sweeping the magnetic field from 100 Oe to -100 Oe. The steps are due to the fact that the YIG layer and the Co layer switch independently at 5 Oe and 50 Oe respectively.

We use the longitudinal SSE method to inject spin current from YIG into Co. In the SSE geometry, a temperature gradient of 40 K/mm is applied along the vertical direction of the sample; spin current is generated in YIG and transmitted through Cu to Co; the V_{ANE} is generated within Co. The obtained thermal voltage in Co/Cu/YIG follows exactly the hysteresis loop of the sample, with YIG switching at about 5 Oe and Co at about 50 Oe. When the YIG layer switches, the thermal voltage captures a sudden drop,

which represents the ΔV_{ISHE}; and when the Co layer switches, the voltage drop represents the ΔV_{ANE}.

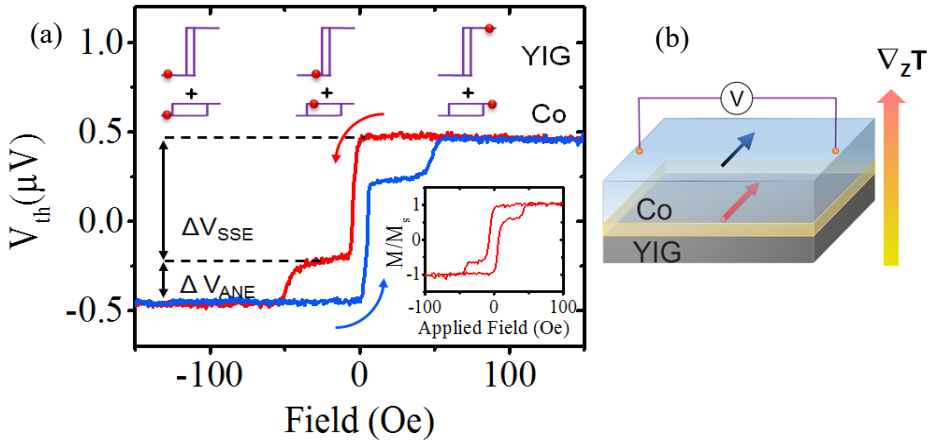

Fig. 8.6 (a) Thermal voltage obtained for the Co(3 nm)/Cu(5 nm)/YIG(120 nm)/GGG sample under a temperature gradient of 40 K/mm. Top insets are the schematics of the ISHE in Co due to thermal spin injection from YIG and ANE in Co due to an out of plane temperature gradient. Bottom inset is the hysteresis loop of the sample. (b) Schematics of the Co/Cu/YIG structure.

There is, however, one complication. Although the Cu layer separates Co and YIG magnetically and allows the transmission of the pure spin current, it also shunts the V_{ISHE} and the V_{ANE} in Co since Cu is metallic. A simple parallel circuit model helps us address this problem. The multi-layer structure may be simplified as a circuit diagram shown as of Fig. 8.7. Both ANE and SSE are generated in the Co layer. V_0 represents the un-shunted total voltage of V_{ISHE} and V_{ANE}. R_{Co} and R_{Cu} are the resistance of Co and Cu, respectively. V_x stands for the measured voltage. Thus,

$$V_0 = V_x \frac{R_{Co} + R_{Cu}}{R_{Cu}}$$

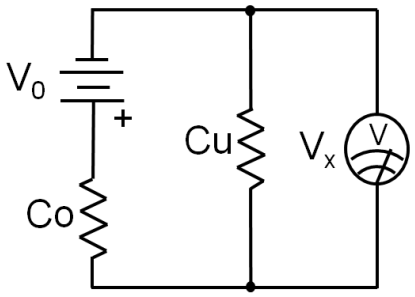

Fig. 8.7 Simplified circuit diagram of the of the Co/Cu/YIG sample.

To demonstrate the validity of this simple scheme, thermal transport using Co(t)/Si and Co(t)/Cu/Si structures with various Co thicknesses and only V_{ANE}. The deduced V_0 values for Co/Cu/Si are in excellent agreement with the V_{ANE} in Co/Si without any shunting effect, as shown in Fig. 8.8(a).

We then performed thermal measurements for Co(t)/YIG and Co(t)/Cu(5 nm)/YIG samples of varying thickness of the Co layer (up to 5 nm; coercivity approaches the YIG value for thicker films). We measured the Co resistivity and calculated the not-shunted V_{ISHE} and V_{ANE}. As expected, ρ increases as the film thickness decreases because of surface scattering. Both V_{ISHE} and V_{ANE} increases as the thicknesses decreases thanks to the short spin diffusion length, Fig. 8.8(b). From the thickness dependence of the thermal voltage, Fig. 8.8(c), we found that Co has a smaller spin Hall angle compared with that of Py, with the ratio of $(\theta_{SH}(Co))/(\theta_{SH}(Py)) = 0.41$.

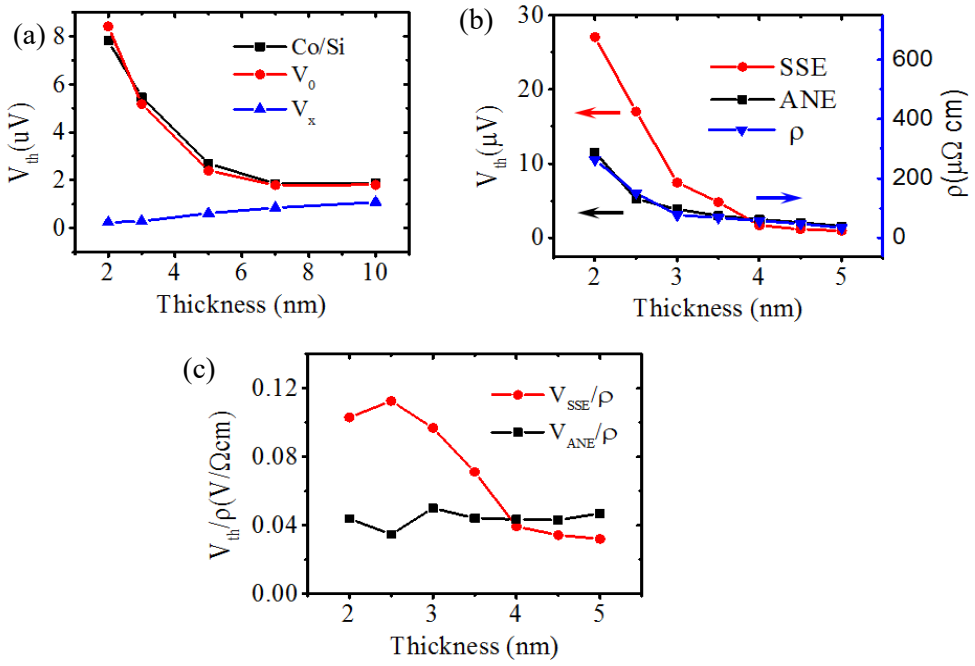

Fig. 8.8 (a) Thickness dependent thermal voltage for Co(t)/Si (black), and Co(t)/Cu(5 nm)/Si (red and blue) sample. V_x is the raw data and V_0 is calculated from the simplified circuit. (b) Thickness dependent inverse spin Hall voltage (red), anomalous Nernst voltage (black), and resistivity (blue) in the Co(t)/Cu(5 nm)/YIG sample. (c) Thickness dependent inverse spin Hall voltage (red) and anomalous Nernst voltage (black) over resistivity.

8.2.2 ISHE Independence on FM Magnetic Ordering

The magnetically decoupled Co/Cu/YIG structure allows us to study how the ISHE is influenced by the ferromagnetic ordering. [8] As shown in Fig.8.9, one first sets a large magnetic field (indicated in Fig. 8.9(b) by box denoted *1*) to align both the Co layer and YIG layer (indicated in Fig. 8.9(a) by arrows denoted *1*), and then reduces the magnetic field to the range where only the YIG layer is subjected to the external field direction, whereas the Co layer remains in its initial state (indicated in Fig. 8.9(b) by box denoted 2). Under such a magnetic field, we set the magnetization of YIG perpendicular to the voltage leads (marked in Fig. 8.9(a) by arrows denoted as *2*), and measure only the ISHE

in Co by switching only the YIG moment. This approach allows the study of ISHE in Co with different Co magnetizations.

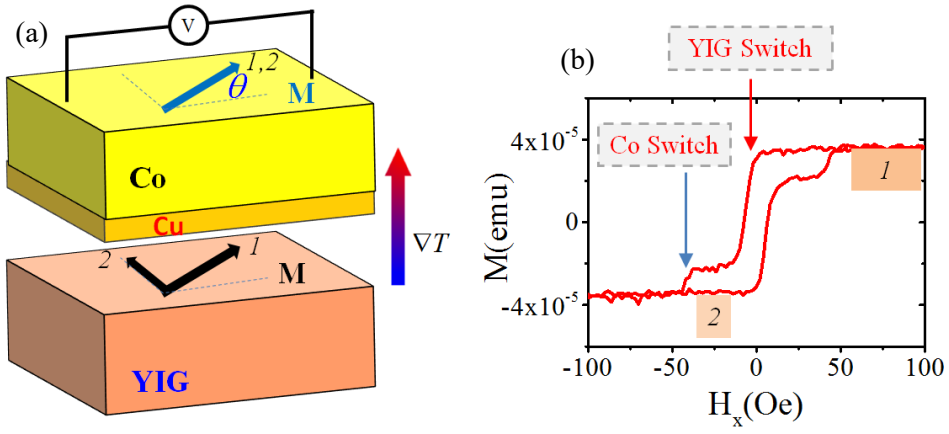

Fig. 8.9 (a) Illustration of experiment geometry for the study of ISHE dependence on FM magnetic ordering. (b) Hysteresis loop of the Co/Cu/YIG structure.

As shown in Fig. 8.10 (a), under a small field from -15 Oe to +15 Oe, the thermal voltages show only one shifted hysteresis loop. The height of the loop represents the V_{ISHE} in Co since only the YIG magnetization has been switched, whereas the vertical shift of the loop represents the ANE in Co thanks to the change of magnetization direction in Co in each of the cases. Thus we obtain the V_{ISHE} and V_{ANE} dependence on Co magnetization direction, as shown in Fig. 8.10(b). We have accounted for the shunting effect from Cu. Notably, in contrast to the sinusoidal angular dependence of V_{ANE}, the V_{ISHE} is *independent* of the Co magnetization direction. The V_{ISHE} independence of magnetization indicates contribution to the ISHE from the extrinsic impurity scattering, with magnetic origin, is negligible. The intrinsic contribution from the Berry phase curvature in the Co band structure may dominate in the ISHE in Co.

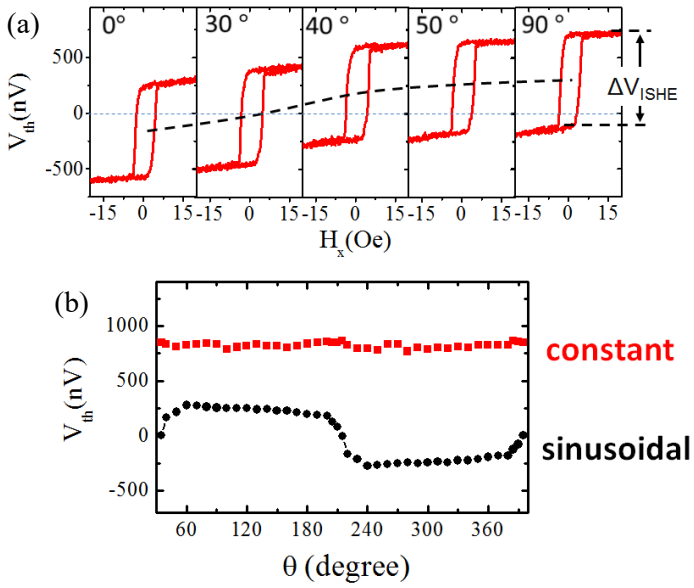

Fig. 8.10 (a) Thermal voltage with only YIG switches under field range -15 Oe to +15 Oe. (b) V_{ISHE} and V_{ANE} dependence on Co magnetization direction.

8.3 ISHE in Antiferromagnetic Metal Cr

Up to this section of the dissertation, the spin Hall effect and inverse spin Hall effect have been explored in non-magnetic heavy metals and ferromagnetic metals only. Recently, the prospect of the AHE in antiferromagnets (AFM) has been theoretically suggested and attracted a great deal of interest. [9-12] Antiferromagnets have been known to be fascinating scientifically but useless technologically since their magnetization, alternating on the atomic scale is largely insensitive to external magnetic field and undetectable by magnetic probes. Exchange bias using antiferromagnets in high-density magnetic recording read heads has been the first and the only significant exception. The discovery of large AHE in an antiferromagnet has generated new interest in the AFM spintronics thanks to the lack of stray magnetic field. Thus, with proper selection and design of AFM, the density and stability of spintronic devices could be greatly enhanced. In this section,

we describe and discuss spin current in antiferromagnetic Cr.

8.3.1 Antiferromagnetic Metals

Theoretically, first-principles calculations have shown that $IrMn_3$, a highly unusual antiferromagnet, may acquire a large anomalous Hall conductivity because of its non-collinear spin structure. [9] Since AHE and SHE share the same physical mechanism, as discussed in Chapter 3, one may expect large SHE and ISHE in such systems. Experimentally, the spin Hall effect has been observed in the antiferromagnets PtMn, IrMn, and PdMn. [10, 11] However, the relationship between the spin Hall effect and the antiferromagnetic ordering remains to be established and understood. Since these materials contain heavy elements with strong spin orbit coupling, it is more difficult to attribute the spin Hall effect in these materials to antiferromagnetism. More interestingly, spin-pumping experiments have shown that a large inverse spin Hall effect exists in *3d* AF Cr. [12] Impressively, despite its low *Z*, the observed θ_{SH} in Cr is comparable to that of *5d* transition metals and is nearly 50 times larger than the theoretical value calculated for Cr. These results lead to the intriguing question of whether the large θ_{SH} in Cr is due to its AF spin structure.

In this section, we study the ISHE in the AF Cr. We explore the prospect of ISHE in Cr for several reasons. Firstly, because Cr is a *3d* metal, a sizable θ_{SH} would be significant in view of the very small θ_{SH} in other *3d* metals such as Cu. Secondly, Cr metal exhibits an incommensurate spin-density wave (SDW) AF ordering below the Néel temperature (T_N) of 311 K, and a spin flip temperature at 123 K, which allows one to explore pure spin current effects in the paramagnetic as well as the AF states. Thirdly,

many *5d* metals such as Pt/YIG, Ta/YIG, and W/YIG, show evidences of magnetic proximity effects (MPE), as described in Chapter 5 and Chapter 7. It remains to be seen whether similar MPE also exists in Cr with a smaller value of *Z* in contact with a ferromagnetic insulator. [13]

8.3.2 Negligible Magnetic Proximity Effect in Cr

We first describe the magnetic proximity effect measurement in Cr/YIG. The unexpected MR and its unusual characteristics in Pt/YIG have been discussed in Chapter 5. Experiments suggest that the contributions for the unusual MR are from both spin current and magnetic proximity effect. The MR obtained for Cr/YIG can be ascribed to these two mechanisms as well. As shown in Fig. 8.11(a), in the small field region (< 2 kOe), the main contribution to the MR of Cr/YIG is spin current. The magnitude of this MR ratio is an order of magnitude smaller than that in Pt/YIG.

In Hall measurements of both Cr(t)/Si and Cr(t)/YIG with thickness *t* from 6 to 15 nm, we observe only the ordinary Hall effect with the Hall voltage linearly dependent on the magnetic field in the temperature range of 5 – 200 K and the field range of ± 5 T. However, unexpectedly in the thinnest 3 nm Cr sample, in addition to the ordinary Hall effect, we have also observed a clear anomalous Hall effect (AHE) signal for Cr(3 nm)/YIG as shown in Fig. 8.11(b). The AHE signal appears above 50 K and remains observable at 300 K, Fig. 8.11(c). However, further measurements indicate that the AHE signal also appears in Cr(3 nm)/Si and is thus unrelated to the presence of YIG. We note that the unexpected AHE in thin Cr has been reported earlier without an explanation of its origin. However, in our case, capping the 3 nm Cr with a 1.2 nm Si layer makes the AHE

contribution disappear so that only the linear ordinary Hall effect remains, as shown in Fig. 8.11(d). Therefore, the AHE in the thinnest unprotected Cr layer should come from surface Cr oxidation. It is noteworthy that both Cr/YIG and Cr/Si show no indication of the magnetic proximity effect, in sharp contrast to a *5d* metal on YIG, such as Pt/YIG and W/YIG. Therefore, Cr can be used as an intrinsic pure spin current detector similar to Au.

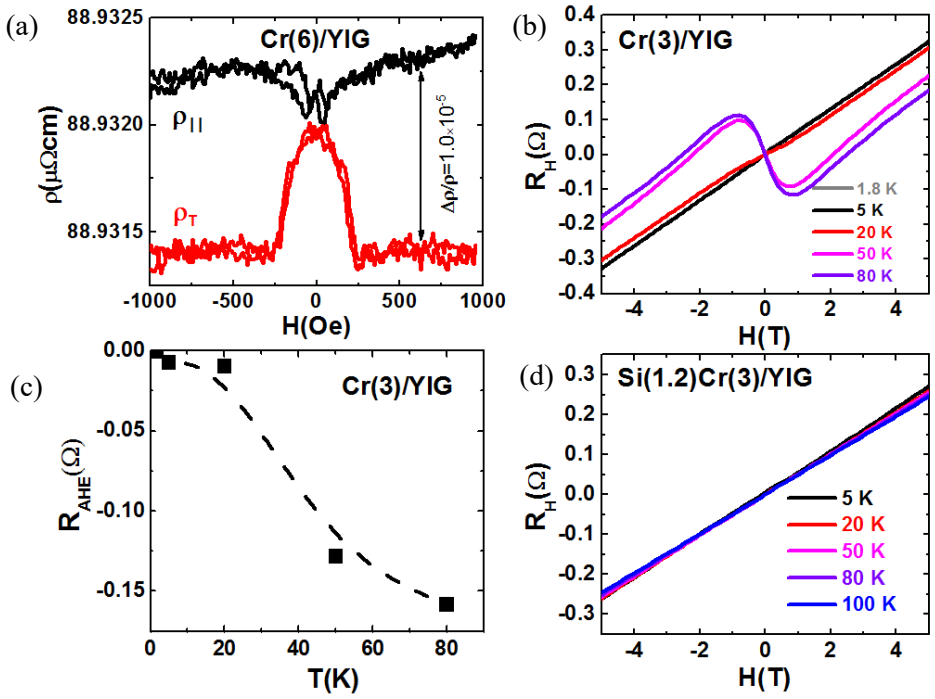

Fig. 8.11 (a) Magnetoresistance of Cr(6 nm)/YIG. (b) Hall measurement of Cr(3 nm)/YIG. (c) Temperature dependent anomalous Hall coefficient of Cr(3 nm)/YIG. (d) Hall measurement of Cr/YIG with 1.2 nm Si capping layer.

8.3.3 Inverse Spin Hall Effect in Cr

We have also studied the spin current phenomena in Cr/YIG. We have used the longitudinal spin Seebeck effect (LSSE) to inject spin current from YIG into the adjacent Cr metal layer. The spin current is then converted into a charge current by the ISHE and we measure the ISHE voltage as illustrated in Fig. 8.12(a).

As shown in Fig. 8.12 (b), the sign of the ISHE voltage in Cr/YIG is opposite to those in Pt/YIG and Au/YIG, which indicates that the sign of θ_{SH} in Cr is opposite to those of Pt and Au. The opposite sign of θ_{SH} is due to the less than half filled *3d* shell in Cr. For 6 nm Cr on YIG, a sizable thermal voltage of - 4.7 μV is observed from positive to negative saturation field, measured from a wire length of 4 mm under a temperature gradient of 20 K/mm. In the sample of Cr (30 nm)/Si, there is no discernable voltage under the same temperature gradient due to the lack of spin current and the absence of net magnetization in AFM Cr. This is also different from the sizable anomalous Nernst effect observed in the ferromagnetic metal Py. These results indicate that the spin current generated in YIG is converted to a charge current in Cr through the ISHE alone; Cr itself does not generate any measurable thermal voltage in the transverse direction under a perpendicular temperature gradient. Therefore, the thermal voltage observed in Cr/YIG can be attributed solely to the ISHE in Cr.

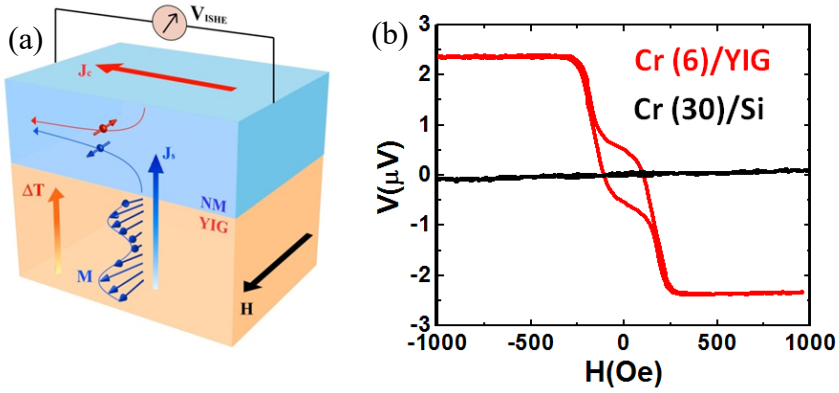

Fig. 8.12 (a) Schematic drawing of the thermal spin injection into a metal layer. (b) Thermal voltage in Cr(6 nm)/YIG (red) and Cr(30 nm)/Si (black).

We have applied the self-consistent method, as described in Chapter 7, for determining θ_{SH} and λ_{SF} by measuring a series of Cr layers with different thicknesses.

The results of the resistivity of the Cr films are shown in Fig. 8.13(a). The resistivity for very thick films is about 25 μΩ-cm, but its value rises sharply to a few hundreds of μΩ-cm for the thinnest films. The measured thermal voltage decreases with increasing Cr thickness as shown in Fig. 8.13(b) thanks to the decay of spin current. Our results can be described by the equation derived in Chapter 7 very well:

$$\Delta V_{th}(t) = 2[CL\nabla T][\rho(t)\theta_{SH}]\left[\left(\frac{\lambda_{SF}}{t}\right) tanh\left(\frac{t}{2\lambda_{SF}}\right)\right],$$

as shown by the sold line in Fig. 8.13(c).

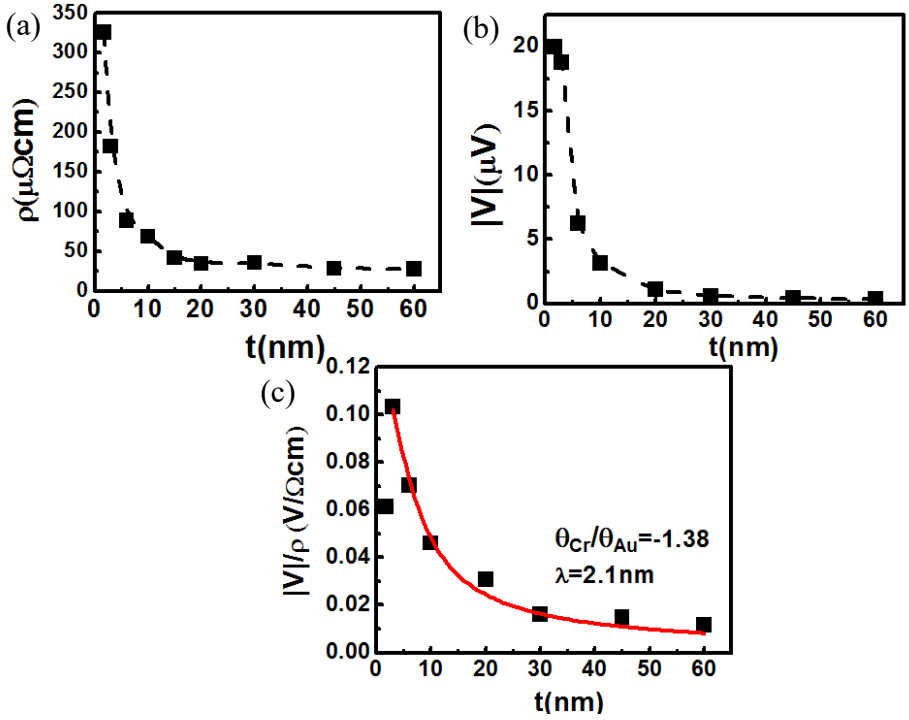

Fig. 8.13 Thickness dependent (a) resistivity, (b) inverse spin Hall voltage, and (c) voltage over resistivity for Cr(t)/YIG samples. Dashed lines in (a) and (b) are guides to the eyes and solid line in (c) is fitting to $\Delta V_{th}(t) = 2[CL\nabla T][\rho(t)\theta_{SH}][(\lambda_{SF}/t)\ \tanh(t/(2\lambda_{SF}))]$.

Assuming the same interface spin current transport efficiency, we obtain $\theta_{SH}\ (Cr)/\theta_{SH}\ (Au) = -1.38$, which is comparable to W and larger than Ta. If we

consider the spin mixing conductance of Cr $g_{eff}^{\uparrow\downarrow} = 1 \times 10^{18} m^{-2}$, the spin Hall angle of Cr is calculated to be θ_{SH}=-0.12, even larger than the *5d* materials. From the the fitted line we also obtained λ_{SH}=2.1 nm, comparable to the values in the literature.

8.3.4 ISHE Independence on Magnetic Ordering in Cr

It has been known that *3d* metals with low *Z* should have very small spin Hall angles relative to those of the *5d* metals. For example, the spin Hall angle in Cu is only 0.0032, which is nearly 20 times less than the *5d* metal Au, and 2 times smaller than the *4d* metal Ag. However, the determined spin Hall angle in the *3d* metal Cr by LSSE is large and comparable to the *5d* metal W. Equally important is the very different value obtained from theoretical calculations, up to 2 orders of magnitude difference.

Since Cr has the unusual spin density wave antiferromagnetic ordering, and its T_N is within experimental limit, it is important to investigate whether the large spin Hall angle in Cr is in anyway related to its *AF* ordering. We measured the thermal voltage of a 10 nm thick Cr film with 1.2 nm Si capping layer from 30 K to 345 K in a cryostation introduced in Chapter 2. For bulk Cr, T_N is 311 K but reduces to 300 K for the 80 nm Cr film on YIG substrate from resistance measurements. For thinner Cr layers, T_N is even lower. Thus, the temperature range of 30 – 345 K should safely covers T_N of all Cr samples, bulk or thin films. A Cernox thermometer reads the temperature of the sample on the cool side and the resistivity of the Cr film is measured to estimate the temperature on the hot side. By adjusting the heater power, we keep the temperature gradient on the Cr/YIG sample close to 20 K/mm.

We plot *V/(RΔT)* vs. hot side temperature in Fig. 8.14(a) to capture the intrinsic temperature dependent behavior of the Cr/YIG system. From 345 K to 100 K, the the *V/(RΔT)* of Cr/YIG steadily increases before decreasing at lower temperatures. This temperature dependence shows no dependence to the antiferromagnetic ordering at T_N to be attributable to Cr. Furthermore, for 5-nm Pt film on YIG, the values of *V/(RΔT)* show virtually the same dependence as shown in Fig. 8.14(b).

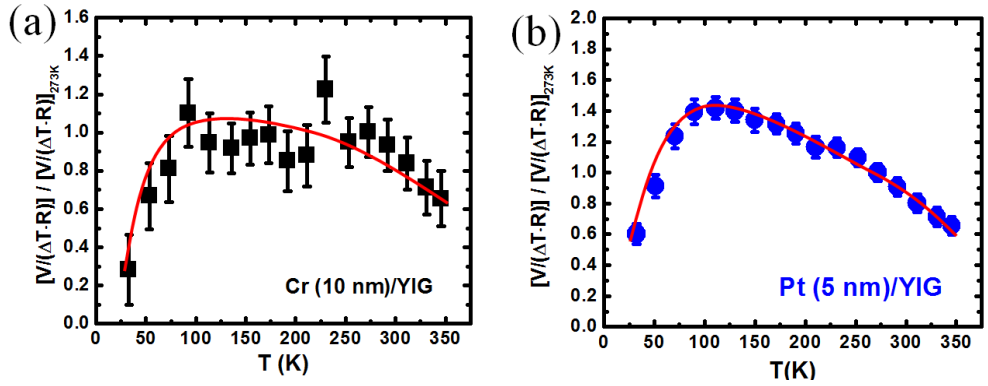

Fig. 8.14 Temperature dependent thermal voltage in (a) Cr(10 nm)/YIG and (b) Pt(5 nm)/YIG samples.

We thus conclude that, the temperature dependence of the ISHE voltages in Cr/YIG is unrelated to the AF ordering in Cr but instead reflects the thermal injection mechanism and the physical properties of YIG. The thermal injection mechanism for a ferromagnetic insulator relies on thermally excited magnons, which freeze out at low temperatures. Thus the ISHE voltage reduces towards zero as the temperature is lowered, in agreement with observations. The maximum of the ISHE voltage at 100 K and is decline at higher temperatures are likely due to the change of the magnon properties in YIG.

Recently, numerical calculations of the YIG magnon thermal conductivity show

that the temperature dependence of YIG magnon thermal conductivity is non-monotonic with a maximum around 70 K. At low temperatures, only magnons with low energy and long wavelength are excited, while at high temperatures the lifetime of magnons with high energy and short wavelength decreases. These results demonstrate that the AF ordering in Cr has no apparent effect on the spin Hall angle of Cr. Since magnetic ordering may affect the magnetic impurity scatterings contribution to the ISHE, the lack of dependence of the ISHE on magnetic ordering indicates the ISHE in Cr has a major contribution from the intrinsic mechanism, consistent with the independence on magnetic ordering for the Co/Cu/YIG structure as described in Sec.8.3.2.

Reference to Chapter 8

1. T. Kimura, Y. Otani, T. Sato, S. Takahashi and S. Maekawa, “Room-temperature reversible spin Hall effect” Phys. Rev. Lett. **98**, 156601 (2007).
2. O. Mosendz, J. E. Pearson, F. Y. Fradin, G. E. W. Bauer, S. D. Bader, and A. Hoffmann, “Quantifying spin Hall angles from spin pumping: experiments and theory”, Phys. Rev. Lett. **104**, 046601 (2010)
3. D. Qu, S. Y. Huang, Jun Hu, Ruqian Wu, and C. L. Chien, “Intrinsic spin Seebeck effect in Au/YIG”, Phys. Rev. Lett. **110**, 067206 (2013)
4. D. Qu, S. Huang, B. F. Miao, S. X. Huang, and C. L. Chien, “Self-consistent determination of spin Hall angles in selected *5d* metals by thermal spin injection”, Phys. Rev. B **89**, 140401 (R) (2014)
5. B. F. Miao, S. Y. Huang, D. Qu, and C. L. Chien, “Inverse spin Hall effect in a ferromagnetic metal”, Phys. Rev. Lett, **111**, 066602 (2013)
6. J. Bass and W. P. Pratt Jr., “Current-perpendicular (CPP) magnetoresistance in magnetic metallic multilayers”, J. Magn. Magn. Mater. **200**, 274 (1999)
7. D. Tian, Y. Li, D. Qu, X. Jin, and C. L. Chien, “Separation of spin Seebeck effect and anomalous Nernst effect in Co/Cu/YIG”, Appl. Phys. Lett. **106**, 212407 (2015)
8. D. Tian, Y. Li, D. Qu, S. Y. Huang, X. Jin, and C. L. Chien, “Manipulation of pure spin current in ferromagnetic metals independent of magnetization”, Phys. Rev. B (R) to be published. (2016)
9. H. Chen, Q. Niu, and A. H. MacDonald, “Anomalous Hall effect arising from noncollinear antiferromagnetism”, Phys. Rev. Lett. **112**, 017205 (2014)

10. J. B. S. Mendes, R. O. Cunha, O. Alves Santos, P. R. T. Ribeiro, F. L. A. Machado, R. L. Rodriguez-Suarez, A. Azevedo, and S. M. Rezende, "Large inverse spin Hall effect in the antiferromagnetic metal $Ir_{20}Mn_{80}$", Phys. Rev. B **89**, 140406 (2014)
11. W. Zhang, M. B. Jungfleisch, W. Jiang, J. E. Pearson, A. Hoffmann, F. Freimuth, and Y. Mokrousov, "Spin Hall effects in metallic antiferromagnets", Phys. Rev. Lett. **113**, 196602 (2014)
12. C. Du, H. Wang, F. Yang, and P. C. Hammel, "Systematic variation of spin-orbit coupling with *d*-orbital filling: Large inverse spin Hall effect in *3d* transition metals", Phys. Rev. B **90**, 140407 (R) (2014)
13. D. Qu, S. Y. Huang, and C. L. Chien, "Inverse spin Hall effect in Cr: Independence of antiferromagnetic ordering", Phys. Rev. B **92**, 020418(R) (2015)

Chapter 9

Conclusion

This dissertation presents a study of the interplay among charge, spin and heat in metal/magnetic insulator nano-structures. The first topic covered in it is the magnetic proximity effect in the Pt/yttrium iron garnet structure, whose signature is the anisotropic magnetoresistance and anomalous Hall like behavior; typical features for ferromagnetic metal exist in a non-magnetic metal Pt. The ferromagnetic features may complicate the signal in Pt when it is used as a pure spin current detector. Therefore, the magnetic proximity effect casts serious doubt on the suitability of Pt as a pure spin current detector in establishing almost all the important pure spin current phenomena, including the spin Seebeck effect. This group first raised this question and attracted lots of attention worldwide. Experimentally, we have found that magnetoresistance in Pt/ferromagnet structures exhibits an unusual dependence on the direction of magnetic field, unlike any magnetoresistance behavior that we know; we attribute this to the magnetic proximity effect. Although the magnetic proximity effect has encountered intense debates with the proposal of spin Hall magnetoresistance, we designed several experiments and demonstrated that the magnetoresistance under the large field is mostly due to the magnetic proximity effect.

Because of contamination by the magnetic proximity effect in the Pt/yttrium iron garnet, one needs to search for a better pure spin current detector for the conclusive

establishment of the longitudinal spin Seebeck effect in the ferromagnetic insulator. We have shown that Au/yttrium iron garnet is the more ideal structure that shows negligible magnetoresistance ratio and only ordinary Hall effect, which are indications that Au does not acquire any magnetic moment in proximity to a ferromagnet. This is the first conclusive demonstration of the intrinsic spin Seebeck effect in yttrium iron garnet by using a pure spin current detector without the contamination of any other effect. With Au as a pure spin current detector, one can now conclusively establish the spin Seebeck effect in a ferromagnetic insulator.

We have succeeded in using the longitudinal spin Seebeck effect to inject spin current into materials of interest. Besides Au and Pt, other *5d* materials such as W and Ta have been predicted and experimentally demonstrated to have large spin Hall angles. However, the spin Hall angles, even for one material, obtained by different methods from different groups show very large variations, sometimes by one or two orders of magnitude. Even the signs may not agree. One needs a consistent method to systematically study the spin Hall angle and spin diffusion length in these materials. We provide one such method by using the longitudinal spin Seebeck effect to inject spin current into materials of interest. The advantage of this method is that it uses a metal/insulator structure with only one interface, thus avoiding complications such as a nontrivial current distribution in the metal/metal case, the decay of spin current in multi-interface structures, and heating from external microwave sources in the spin pumping method. This simple, versatile and consistent method has allowed us to obtain the relative spin Hall angle and spin diffusion length of many materials under the assumption that spin mixing conductance are equal.

Finally, we have demonstrated that the inverse spin Hall effect exists not only in non-magnetic materials, but also in magnetic material such as ferromagnetic metal Py and antiferromagnetic metal Cr. We have shown that inverse spin Hall effect is insensitive to the onset of the ferromagnetic ordering in Co by decoupling the magnetization of Co with yttrium iron garnet. We have also shown that the inverse spin Hall effect is independent of the antiferromagnetic ordering in Cr by varying the measurement temperature from below to above the ordering temperature. The consistent results indicate that the intrinsic contribution from Berry phase is dominant in the inverse spin Hall effect in these magnetic materials. Moreover, we have determined the spin Hall angles in these magnetic materials, and found them comparable to those of *5d* metals, especially after taking into account the spin mixing conductance at the interface. Cr thin films on yttrium iron garnet show the largest spin Hall angle among all the materials studied during the course of this thesis. This would make Cr the material with the largest spin Hall angle.

The novel physical properties discovered and studied in this dissertation, such as the unique magnetoresistance, the intrinsic spin Seebeck effect, and the large spin Hall angle in materials regardless of their magnetic orderings or atomic numbers, may find applications to high-density, low-power-consumption, and stable future spintronic devices.

List of Publication

1. D. Tian, Y. Li, **D. Qu,** S. Y. Huang, X. Jin, and C. L. Chien, "Manipulation of pure spin current in ferromagnetic metals independent of magnetization", Phys. Rev. B **94**, 020403(R) (2016)
2. B. F. Miao, S. Y. Huang, **D. Qu**, and C. L. Chien, "Absence of anomalous Nernst effect in spin Seebeck effect of Pt/YIG", AIP Advances **6**, 015018 (2016)
3. **D. Qu**, S. Y. Huang and C. L. Chien, "Inverse spin Hall effect in Cr: independence of antiferromagnetic ordering", Phys. Rev. B **92**, 020418(R) (2015)
4. Dai Tian, Yufan Li, **D. Qu**, Xiaofeng Jin and C. L. Chien, "Separation of spin Seebeck effect and anomalous Nernst effect in Co/Cu/YIG", Appl. Phys. Lett **106**, 212407 (2015)
5. **D. Qu**, S. Y. Huang, B. F. Miao, S. X. Huang and C. L. Chien, "Self-consistent Determination of Spin Hall Angles of Selected 5d Metals by Thermal Spin Injection", Phys. Rev. B **89**, 140407 (R) (2014)
6. B. F. Miao, S. Y. Huang, **D. Qu** and C. L. Chien, "Physical Origins of the New Magnetoresistance in Pt/YIG", Phys. Rev. Lett. **112**, 236601 (2014)
7. B. F. Miao, S. Y. Huang, **D. Qu** and C. L. Chien, "Inverse spin Hall effect in a ferromagnetic metal", Phys. Rev. Lett. **111**, 066602 (2013)
8. **D. Qu**, S. Y. Huang, Jun Hu, Ruqian Wu and C. L. Chien, "Intrinsic spin Seebeck effect of Au/YIG", Phys. Rev. Lett. **110**, 067206 (2013)
9. S. Y. Huang, **D. Qu** and C. L. Chien, "Charge, Spin, and Heat Transport in the Proximity of Metal/Ferromagnet Interface, Recent Advances in Magnetics Insulators

- From Spintronics to Microwave Applications", A Special Issue of "Solid State Physics" Series (2013).

10. Y. M. Lu, J. W. Cai, S. Y. Huang, **D. Qu**, B. F. Miao and C. L. Chien, "Hybrid magnetoresistance in the proximity of a ferromagnet", Phys. Rev. B **87**, 220409 (R) (2013)
11. S. Y. Huang, X. Fan, **D. Qu**, Y. P. Chen, W. G. Wang, J. Wu, T. Y. Chen, J. Q. Xiao and C. L. Chien, "Transport magnetic proximity effect in Platinum", Phys. Rev. Lett. **109**, 107204 (2012)
12. Hui Zhang, Jun Dai, Yujing Zhang, **Danru Qu**, Huiwen Ji, G. Wu, X. F. Wang, X. H. Chen, Bing Wang, Changgan Zeng, Jinlong Yang, and J. G. Hou, "Universal $\sqrt{2} \times \sqrt{2}$ structure and short-range charge order at the surfaces of $BaFe_{2-x}Co_xAs_2$ compounds with various Co doping levels", Phys. Rev. B **81,** 104520 (2010)

Vita

Danru Qu was born on January 2nd, 1989 in Jiujiang city, Jiangxi Province, the People's Republic of China. In 2006, she attended University of Science and Technology of China (USTC) and majored in Physics. During the four-year undergraduate in USTC, she was awarded Guanghua Fellowship, Outstanding student award, and third prize in statistical modelling competition in USTC. She graduated in 2010 with B. S. Degree in Physics. At the same year, she enrolled in the Ph.D. program in the Department of Physics and Astronomy at the Johns Hopkins University, and she worked on experimental condensed matter physics under the guidance of Professor C. L. Chien. During the six-year Ph.D. study, she was awarded Gardner Fellowship, Best in session award in Techcon conference, student travel award in magnetism and magnetic materials (MMM) conference, and Chinese government award for outstanding student abroad. She has published 11 peer reviewed journals including 3 first authored papers. She has also presented 1 invited talk and 4 contributed talks on APS March meetings and MMM conferences.